MULTISCALE MODELING OF COUPLED OSCILLATORS WITH APPLICATIONS TO THE MAMMALIAN CIRCADIAN CLOCK

by

Daniel Aaron DeWoskin

A dissertation submitted in partial fulfillment
of the requirements for the degree of
Doctor of Philosophy
(Applied and Interdisciplinary Mathematics)
in The University of Michigan
2015

Doctoral Committee:

Professor Daniel B. Forger, Co-chair
Associate Professor Santiago Schnell, Co-chair
Associate Professor Victoria Booth
Professor Trachette L. Jackson
Assistant Professor Sara J. Aton

ACKNOWLEDGEMENTS

I have been very fortunate to have the help and support of the members of my thesis committee as well as several invaluable experimental collaborators throughout my graduate studies. Without their help and guidance, this thesis would not have been possible. First and foremost, I would like to thank my adviser, Danny Forger. He inspired me to pursue my joint passions of mathematics and biology and helped me to find a way to combine the two through the study of biological clocks. Over the past five years, he has greatly supported all of my work, and in addition to math, he has also taught me how to do research, how to work with collaborators, how to write manuscripts, and so much more. He introduced me to the circadian field, helped me to establish many experimental collaborations, and supported me in visiting their labs. His mentorship and support throughout my graduate studies has made all of this possible, and I couldn't have asked for a better adviser. I am also extremely grateful to my co-advisor Santiago Schnell. He welcomed me into his lab and taught me a lot about modeling biological systems. Additionally, I thank him for all of his life advice, and discussions about working as a scientist in a medical school and industry, writing papers, and grant writing. Both of my advisers have greatly contributed to my development and I owe them greatly for my success at Michigan. I am also grateful to Victoria Booth, Trachette Jackson, and Sara Aton for serving on my committee. Victoria Booth provided my first training as a computational neuroscientist, and our many discussions about neuronal signaling have been a great help in my thesis work. I thank Trachette Jackson for discussing cancer modeling with me and making possible

the great experience I had attending the Mathematical Problems in Industry Workshop. I thank Sara Aton for joining my committee and providing an experimentalists point of view on circadian rhythms and signaling in the SCN.

I would like to thank Seth Meyer and Bennet Fauber for their help with scientific computing, troubleshooting, and working with GPUs. Additionally, I thank Divakar Viswanath for his help with parallel programming on GPUs.

I sincerely thank all of the current and former students of Danny Forger that I have had the pleasure of working with during my time at Michigan: Jae Kyoung Kim, Casey Diekman, Adam Stinchcombe, Olivia Walch, Kirill Serkh, and Kevin Hannay. Without the work of Jae and Casey in developing the foundational models of SCN molecular timekeeping and electrophysiology, and our many long discussions together on these subjects, my thesis would not have been possible. I especially thank you both for your continued help and advice on scientific subjects as well as life as a researcher, even after graduating and moving on to other positions. I would like to thank Adam Stinchcombe for all of the help and discussions about numerical methods and programming on GPUs. You have been a great friend, colleague, and collaborator, and inspired me as a mathematician. I thank Olivia Walch for facilitating many great discussions between the members of our group about circadian rhythms and entrainment, as well as for her amazing figure-making skills.

I also thank all of the members of the Schnell lab during my time at Michigan: Mark Whidden, Michelle Wynn, Caroline Adams, Allison Ho, Michael Vincent, Márcio Mourão, Erin Shellman, Conner Sandefur, and Firas Midani. Attending the Schnell lab meeting has been a great experience. You have each provided very valuable feedback on my work over the years, and educated me on a variety of other subjects in mathematical biology. The Schnell lab has been a second home for me at Michigan, and I have always enjoyed our great discussions.

I owe a great debt of gratitude to all of my experimental collaborators: Mino Belle, Hugh Piggins, Jihwan Myung, Toru Takumi, Jodi Paul, and Karen Gamble. Each of them not only shared their valuable data, but also welcomed me into their labs and taught me a great deal about circadian biology. I owe much of my understanding of the SCN to discussions with these incredible biologists. I would especially like to thank Toru Takumi and Jihwan Myung for hosting me for an extended stay in Japan. Jihwan, I thank you for all of our long talks about science in general and life as a researcher. I would additionally like to thank Marco Brancaccio, Michael Hastings, and Jennifer Evans for sharing their data with me.

I would also like to thank all of my funding sources for their essential support throughout my graduate studies including the Human Frontiers of Science Program, the Air Force Office of Scientific Research, the Department of Mathematics at Michigan, and the Rackham Graduate School.

Finally, I would like to thank my family and friends for their love, support, and encouragement. I owe you more than I can say, and certainly more than fits in this short acknowledgement, but suffice it to say that without all of you, I would not be who I am today.

TABLE OF CONTENTS

LIST OF FIGURES

Figure

ABSTRACT

Multiscale Modeling of Coupled Oscillators with Applications to the Mammalian Circadian Clock

by

Daniel Aaron DeWoskin

Co-chairs: Daniel B. Forger, Santiago Schnell

Many biological systems function based on two essential motifs: network interactions between cells and integration across timescales. Both of these are ubiquitous in coupled biological oscillators, such as in heart and brain tissues, which require communication and coordination between cellular oscillators across timescales in order to generate tissue-level rhythms. Mathematical modeling can provide invaluable insight in order to explain this complexity. In this dissertation, we develop a detailed model of the suprachiasmatic nucleus (SCN), the central circadian (daily) pacemaker in mammals, and numerical methods for simulating it. This new multiscale model resolves the intracellular molecular events that generate circadian rhythms as well as the cellular electrical activity important for relaying timing information to the rest of the brain. The model not only reproduces experimental findings, but also makes several new predictions about the role of intercellular signaling in the SCN, some of which we experimentally validate. First, the model explains how intercellular signaling in the SCN increases robustness of tissue-level rhythms. Second, it proposes a new mechanism by which the SCN can differentially regulate intra-SCN synchrony and SCN

output signals through a single neurotransmitter signaling on disparate timescales. Third, it shows how the response polarity of cells to this neurotransmitter changes depending on the particular daylength an animal has been entrained to. By modulating the response and the intrinsic period of subsets of SCN neurons, phase-locked populations of cells are used to encode the daylength of the entraining signal. Finally, the model predicts that a kinase can be used to modulate the firing rate of cells to control SCN output. On the whole, the model answers many open questions about signaling within the SCN and control of SCN output to the rest of the brain. It presents a holistic picture of the SCN as a robustly oscillating network with its synchrony and output signals modulated on two different timescales in response to the entraining light signal. The computational framework developed herein with parallelization using GPUs provides an important tool for circadian research, and a model computational system for the many multiscale projects currently studying brain function.

CHAPTER I

Introduction

Despite many years of intense study, the functioning of the human brain remains one of the least understood topics in modern science. Much is known about small sections of the brain, but the methods by which neuronal networks process, encode, and transmit information still largely remain an open question.

Mathematically, studying brain networks provides many interesting challenges. Neurons can exhibit a wide variety of electrical activities. On short time scales, from milliseconds to seconds, they often show large oscillations (action potentials) in their membrane voltage, driven by the motion of charged ions through channels in their cell membranes. On longer time scales, from hours to days to even years, these electrical oscillations are slowly modulated by changes in the state of the cell, often due to differences in gene expression. On each of these disparate timescales, neuronal activity is influenced by other cells in the network, with each neuron both sending and receiving signals to many other coupled cells.

This problem of networks of coupled oscillators with essential behaviors occurring across disparate spatial and temporal scales is a common feature to many problems in biology. Biological systems are intrinsically multiscale, with levels of organization ranging from the atomic to the whole organism level. In our example of the firing of an action

potential in a neuron, the process begins at the atomic level where motion of individual ions through small protein channels cause changes at the cellular level. This leads to propagation of the signal through intercellular signaling pathways, and eventually ends in important macroscopic changes in firing of entire neuronal networks. The question then becomes how do we integrate information from a variety of cellular processes to understand effects at the tissue or organism level? From a modeler's perspective, this is a very difficult question, as it involves a wide range of temporal and spatial scales. This thesis develops and applies a detailed multiscale model of a fairly well understood system: the mammalian circadian clock.

Circadian rhythms are endogenous, roughly 24 hour rhythms in behavior or physiology. These rhythms are entrained by external signals, such as light and food intake, but persist even in their absence. In mammals, the ~20,000 neurons of the suprachiasmatic nucleus (SCN) form the central circadian pacemaker, and send out time of day information to the rest of the body. Time is coordinated both through oscillations in protein concentration occurring over hours, and oscillations in membrane voltage occurring over milliseconds. These activities influence each other within each of the neurons of the SCN. Additionally, intercellular signaling on each of these time scales has been shown to be essential for coordinating tissue-level rhythms. In particular, isolated, neurons of the SCN show weak, noisy rhythms [82] that can gain or lose rhythmicity in response to external stimuli [135]. When coupled together, however, these neurons form a robust circuit with precise 24-hour oscillations that is resistant to genetic mutations [76]. Thus, important interactions on the network level lead to emergent behaviors that cannot be seen by considering only a single cell.

In Chapter II of this thesis, we build a detailed multicellular model of the molecular rhythms in the SCN in order to study the role of intercellular signaling in creating robust,

tissue-level rhythms. Next, we extend the multicellular model to a multiscale model, incorporating the electrophysiology of SCN neurons to study signaling on this much faster timescale (Chapter III). After fitting the model and developing techniques for simulating it, we use it to study two open questions in the SCN: first, the encoding of seasonal time within the relative phase relationship of neurons in the SCN network (Chapter IV), and second, how the electrical activity and output of SCN neurons can be controlled by the molecular clock, in particular through a specific kinase (Chapter V).

While much of this thesis is devoted to the specific problem of circadian rhythms, the methods and framework for simulating the model developed herein are widely applicable to many biological networks such as in the heart, pancreas, or other parts of the brain. These systems all share the common thread that they are large networks of coupled oscillators with important behaviors on both fast (seconds or faster) and slow (hours to days) time scales. Additionally, we will discuss computational techniques including parallel programming with graphics processing units (GPUs), which can make the simulation of these detailed multiscale models possible.

1.1 Biological background

Circadian rhythms are endogenous rhythms in behavior or physiology with periods of approximately 24 hours [134]. These rhythms are maintained by internal pacemakers, or clocks, which play essential roles in the regulation and synchronization of many physiological processes. While originally assumed to be possible only in advanced multicellular organisms, circadian rhythms have been found to be so fundamental to adapting to life on Earth that they exist not only in plants, fungi, and animals, but also in organisms as simple as prokaryotic cyanobacteria [33, 42, 56, 109]. In this dissertation, we will focus on the interesting problem of how the mammalian circadian clock, driven by the central

circadian pacemaker in the suprachiasmatic nucleus, integrates information across many cells on two different timescales to coordinate daily activities throughout the organism.

1.1.1 The suprachiasmatic nucleus

The suprachiasmatic nucleus (SCN) is a two-lobed structure, with each lobe made up of approximately 10,000 neurons. It is located in the anterior hypothalamus, just dorsal to the optic chiasm, with one lobe on either side of the third ventricle [137]. The lobes are each organized into two subdivisions: the ventral "core" region, and the dorsal "shell" region which partially surrounds the core [137]. The SCN is considered to be the master pacemaker in mammals because experiments have shown that ablation of the SCN is sufficient for abolishing circadian rhythms, and that rhythms with the intrinsic period of the graft SCN can be reestablished via transplantation [116, 134].

Individual cells of the SCN keep time through autonomous oscillations in the protein concentrations of key "clock" proteins, such as PER and CRY. In addition, the neurons show variations in electrical activity including the rate of firing action potentials (APs) throughout the day. The combination of these two types of oscillations leads to a robust rhythm within the SCN. The way in which activity from individual cells is integrated into a coherent output from the SCN to the rest of the animal is still not well understood.

The SCN receives input from a variety of external signals such as feeding and activity, but the strongest entraining signal is light. Intrinsically photosensitive retinal ganglion cells receive light input and transmit it directly to the SCN, where they stimulate SCN neurons [88, 137] and entrain them to the light-dark cycle of the environment.

It is essential to note that while the SCN will modulate its activity in order to entrain to light cues, it is also an endogenous oscillator which will continue to produce coherent rhythms even in the absence of external forcing. In fact, the neurons of the SCN even oscillate autonomously when extracted from the animal as an organotypic slice [141] or

as individual neurons grown in isolation [136]. These rhythms are different, however, as an SCN slice shows robust, coherent rhythms while the physically dissociated, isolated neurons show heterogeneous oscillations with a wide range of periods and no clear phase relationships [136].

While much is known about the SCN, there are still many open questions about the way in which a collective rhythm is generated by thousands of heterogeneous, independent oscillators. A variety of important neuropeptides are involved in creating this coherent rhythm. These neuropeptides are expressed throughout the SCN, and play critical roles in maintaining synchrony. The spatial organization of which cells express which peptides seems to vary across species, and is not fully understood [27, 117]. It is generally accepted, however, that a large portion of the cells in the core express vasoactive intestinal peptide (VIP) (roughly 10-15% of SCN neurons), and that a large percentage of the shell neurons express arginine vasopressin (AVP) (roughly 20% of SCN neurons) [6, 8, 137]. These neuropeptides are essential for intercellular communication within the SCN. For instance, knockout of either VIP or its receptor VPAC2 have both been shown to severely diminish synchrony within the SCN and also lead to diminished or absent circadian rhythms in locomotor activity, body temperature, and heart rate [6, 8, 26, 49, 112].

1.1.2 Transcription/translation feedback loops

At the core of the circadian oscillations within the cells of the SCN is a transcription/translation negative-feedback loop shown in figure 1.1 [108, 140]. In this pathway, the proteins Circadian Locomotor Output Cycles Kaput (CLOCK) and Brain and Muscle Aryl hydrocarbon receptor nuclear translocator-Like 1(BMAL1) form an activator complex which binds to an E-box in the promoter of the Period (Per1, Per2, Per3) and Cryptochrome (Cry1, Cry2) genes [53, 52]. This leads to the transcription of the Per and Cry mRNAs, which are then translated into the PER and CRY proteins. PER and CRY proteins

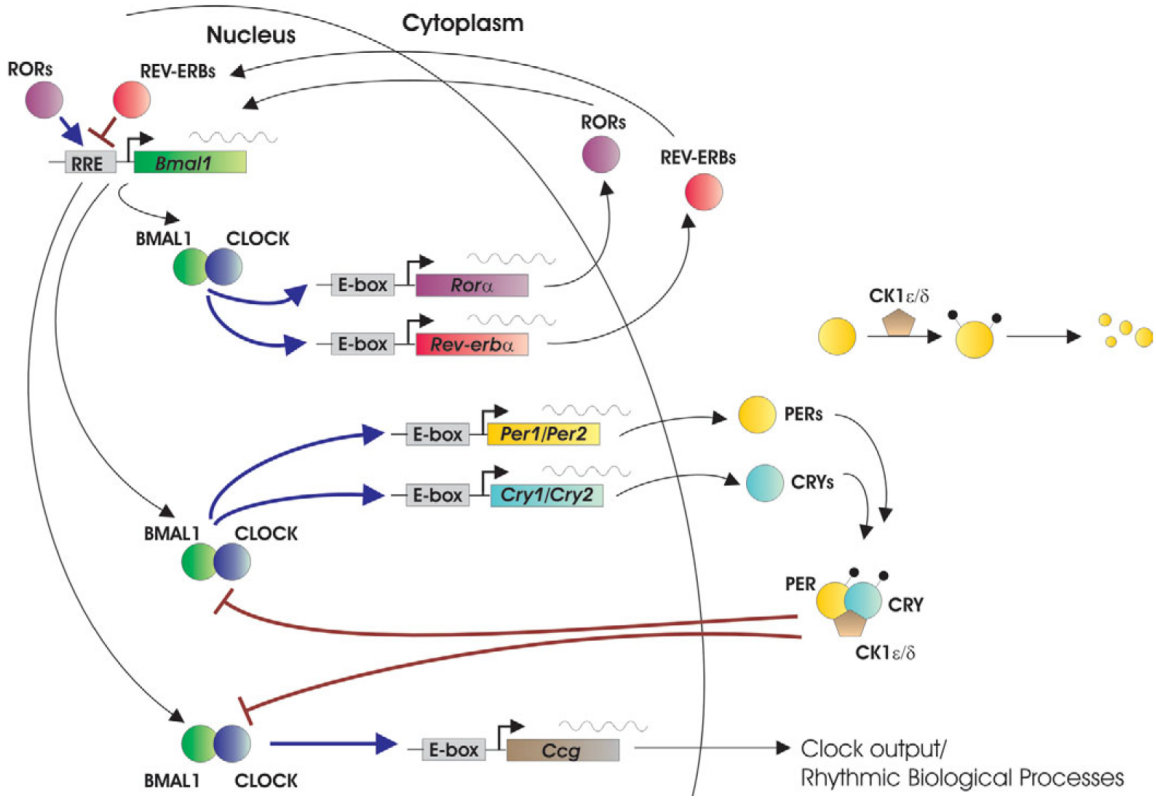

Figure 1.1: A schematic of the key components of the mammalian circadian clock (figure reproduced from [61]). The core negative feedback loop involves the BMAL1:CLOCK activated transcription and consequent translation of the PER (1, 2, and 3) and CRY (1 and 2) proteins. PER and CRY proteins form a heterodimer and are also phosphorylated by casein kinase 1 (CK1ε or CK1δ) before being translocated into the nucleus, where they repress their own transcription through BMAL1:CLOCK inactivation. BMAL1:CLOCK also activated transcription of the RORs and REV-ERBs which activate and repress Bmal1 transcription respectively.

are phosphorylated by casein kinase 1 (CK1ε or CK1δ), and form heterodimeric repressor complexes which translocate into the nucleus. In the nucleus, the PER/CRY complex binds the CLOCK:BMAL1 complex inactivating it, causing repression of Per and Cry gene expression. Phosphorylation of the PER and CRY proteins also leads to degradation, at least partially through ubiquitination regulated by the ubiquitin ligase complexes β-TrCP1 and FBXL3 [115, 122, 137]. The decline in PER/CRY levels frees up activator complexes so that the cycle may repeat. A diagram of the core feedback loop is contained in figure 1.1.

In addition to the core negative-feedback loop described above, there is the ROR/REV-ERB/Bmal1 feedback system, also diagramed in figure 1.1. Expression of the RORs

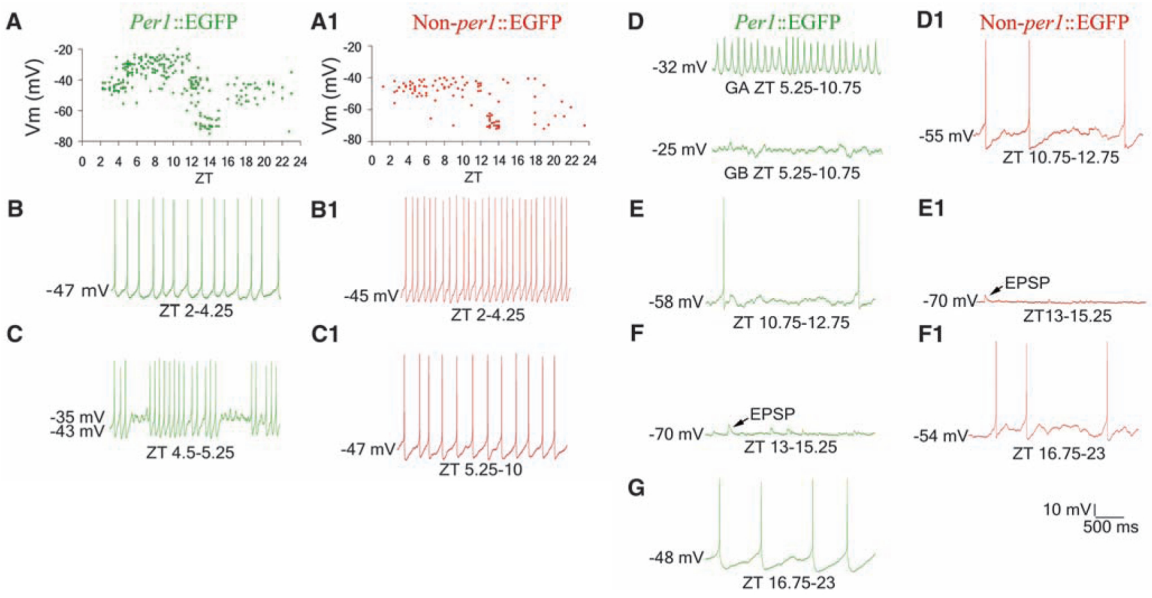

Figure 1.2: Circadian variation in electrical activity of Per1 (green) and non-Per1 (red) cells (figure reproduced from [14]). Zeitgeber time (ZT) 0 is subjective daybreak, and ZT 12 is subjective nightfall. Cells displaying circadian variation in Per1 reach high levels of membrane depolarization in the mid to late afternoon, and may switch into low amplitude oscillations (panel D). Non-per1 cells have a lower resting membrane potential during these hours, and show high levels of spiking (panel C1).

(RORα, β, and γ) and REV-ERBs (α and β) is driven by the circadian clock, presumably by the activation of E-box elements by CLOCK:BMAL1 [75, 126]. These proteins then compete for access to their response elements (RORE) on the Bmal1 promoter, and differentially affect Bmal1 expression: the RORs activate Bmal1 transcription, while the REV-ERBs repress it [47, 75]. These additional feedback loops are thought to add an additional level of control which helps to stabilize BMAL1 levels, but they have been shown to be unnecessary for circadian function, as constitutively expressed BMAL1 is also able to drive normal circadian rhythms or rescue rhythms in Bmal1$^{-/-}$ mice [75, 80].

1.1.3 Electrical activity

The neurons of the SCN show spontaneous firing of action potentials throughout the day. The classical theory is that action potential firing rate varies in a circadian fashion,

with higher frequency firing during the day than at night [57]. More recently, cells expressing circadian variation in the Per1 gene have been shown to display two previously unreported behaviors: a depolarized steady state at approximately -25mV and depolarized low-amplitude oscillations with a resting membrane potential of approximately -32mV [14]. These new electrical states were seen in the mid to late afternoon. Circadian variations in resting membrane potential and resistance are also seen, and seem to account for the transition to these depolarized states [14]. A summary of the firing behaviors seen in Per1 and non-Per1 cells as a function of zeitgeber time (ZT) is shown in figure 1.2.

When plated in dispersed culture, individual SCN neurons have been shown to maintain circadian variations in firing rate with periods ranging between 21.25 and 26.25 hours [136]. Interestingly, the neurons had no specific phase or period relationship with their neighbors, and maintained their intrinsic periods and phases after application and removal of TTX, causing a temporary blockade in action potentials [136]. These experimental results suggest that firing rate may be a function of the phase of each cell's internal molecular clock.

The firing dynamics of SCN neurons involves several ionic currents, including sodium, L-type calcium, voltage-activated potassium, calcium-activated potassium, and background leak currents [17, 57]. Individual neuronal activity is also influenced by other cells in the network. Synaptic coupling between SCN cells seems to be fairly sparse, with more projections from core to shell than from shell to core [137]. As mentioned above, a variety of neuropeptides are involved in signaling in the SCN, with different expression levels in different regions of the SCN. The only neurotransmitter that seems to be universally expressed is GABA [86]. While GABA is generally considered to be an inhibitory signaling molecule, some studies have shown that it can provide excitatory signals in the SCN as well, and perhaps specifically in the dorsal or shell region [4, 24, 28].

1.2 Previous modeling approaches and their limitations

1.2.1 Single-cell electrophysiology models

Most detailed neuronal models are based on the Hodgkin-Huxley (HH) equations, developed in the early 1950s [51]. The underlying idea is to consider a small patch of membrane as a circuit, and analyze the voltage across it, and the ionic currents that flow through it. The original HH model contained four variables, one for the membrane voltage, and the other three describing the gating of the sodium and potassium currents. It was fit to data recorded from the squid giant axon. The HH model spawned an entire class of neuron models, each with different attributes and relevant ionic currents. In general, they are all of the form

$$C_M \frac{\mathrm{d}V}{\mathrm{dt}} = \sum I_{ion} \qquad \text{where} \qquad I_{ion} = g_{ion}(E_{ion} - V)$$

In the above, V is the membrane voltage, I_{ion} is an ionic current with reversal potential E_{ion}, and membrane conductance g_{ion}. The conductance, g_{ion}, is the inverse of the membrane resistance, and is often allowed to vary in time.

The first detailed model specifically fit to the electrophysiology of SCN neurons was constructed by Sim and Forger [118]. The Sim-Forger model is a HH-type model, which includes the dynamics of four ionic currents: sodium, potassium, calcium, and a leak current. The model includes six ordinary differential equations (ODEs): one for membrane voltage, and 5 ionic gating variables, which give the the dynamics of the ionic currents. Simulations using this model match both the firing rates and dynamics of these ionic currents seen in real SCN neurons.

1.2.2 SCN electrophysiology models

Diekman and Forger revised the Sim-Forger model, and used it to perform a large multicellular simulation of the electrical activity of the SCN [32]. In their model, 10,000 cells

with heterogeneous firing rates were coupled randomly with a combination of inhibitory and excitatory synaptic signaling. In order to add further variability to the system, the authors also tested different coupling strengths, and included a probability of faulty synaptic transmission as well as variability in the amplitude of post-synaptic currents generated by each firing event. In all cases, with a sufficient coupling strength, the neurons eventually clustered into generally three distinct groups, each 1/3 of an oscillation out of phase, even with synaptic connectivity as low as 5%. In some cases, a fourth silenced or non-firing cluster was seen as well. Interestingly, the simulations showed that having a significant fraction of excitatory connections actually led to increased coherence within clusters. If a majority of synaptic connections were excitatory, however, all neurons synchronized and fired together. Finally, the authors showed that most neurons in their simulation had a firing rate of about 3 Hz. Neurons with higher or lower intrinsic firing rates were slowed down or silenced, so that they either matched the consensus firing rate, or did not fire at all. Based on these results, the authors hypothesize that the clustering of firing in the SCN may provide a way to generate a single coherent output from the SCN and modulate the activity of neurons that differ from the majority.

1.2.3 Single-cell molecular clock models

The first detailed molecular model of the mammalian circadian clock was created by Leloup and Goldbeter in 2003 [72]. It contained 16-19 ODEs, and described the dynamics of the Per, Cry, Bmal1, Clock, and Rev-Erbα genes and protein products. For suitable choices of parameters, the model could generate circadian oscillations, or damped rhythms, and could also be entrained by an external stimulus, simulating the effect of light. The model also predicted the antiphase relationship of Per/Cry and Bmal1 oscillations. Although the model provided a good start for mammalian circadian modeling, it made some questionable assumptions, such as having all transcription occur through

Hill-type equations, and many degradation and reaction events through Michaelis-Menten kinetics.

Later that year, Forger and Peskin produced a more detailed model of the molecular clock, which importantly used only mass action kinetics rather than assuming Hill or Michaelis-Menten-type kinetics [42]. The assumption of cooperativity of Bmal1 E-box binding does not seem to match experimental data, so this is a more physiologically reasonable approach. The model also distinguished between Per1 and Per2, and Cry1 and Cry2, and included the dynamics of gene and kinase binding and unbinding. Simulations from the model fit experimental data well, and the model was also able to predict some knockout phenotypes. A variation of this model was also used for stochastic simulations using the Gillespie algorithm [43]. These simulations showed that the model was robust to noise, even at low numbers of molecules. Interestingly, the authors also found that the Per2 knockout was rhythmic in the stochastic model (matching some experimental data), even though it was arrhythmic in the related deterministic model.

A simplified model was proposed by Becker-Weimann et al., which contained only seven ODEs [12]. The Becker-Weimann model again used high Hill coefficients in the transcription terms in order to create oscillations. The rest of the reactions, however, followed mass action kinetics. The model is similar to the Leloup-Goldbeter model, and is essentially an expanded Goodwin oscillator. Because of its simplicity, it can not be used for in depth comparisons with experimental data.

More recent detailed models include those by Mirsky et al. [85] and Relógio et al. [107]. These two models describe the core Per/Cry negative feedback loop as well as the secondary ROR/Rev-Erb/Bmal1 control loop. Both models employ Michaelis-Menten and Hill functions in the transcription rates, and use mass action kinetics for the rest of the reaction and degradation steps. The Relógio model focuses on the secondary ROR/Rev-

Erb/Bmal1 control loop, and shows that in their model, it can function as an independent oscillator. This has not been verified experimentally. The gene knockout results of both models do not match well with experimental data.

The Forger-Peskin model has also recently been updated in [60]. The new version is much more detailed, as much more has been learned about the molecular clock in the last nine years. A schematic of several key parts of the model is given in figure 1.3. The model has 208 molecular species and complexes, but given its size, it has a relatively small number of parameters (70). Interestingly, although it has 10 times as many molecular species as either the Mirsky or Relógio models, it has the least parameters of the three since it does not use any Michaelis-Menten or Hill functions. Fourteen of the parameters were measured, and the rest were fit to experimental data. The new model is able to predict most knockout phenotypes described in [10], and elucidated the importance of the secondary negative feedback loop through Rev-Erbα which had previously been thought to play little role. The authors showed that the secondary negative feedback loop is important for maintaining the stoichiometry of BMAL1:CLOCK activator complexes to the PER/CRY repressor complexes, which in turn leads to robust rhythms with a very fixed period even under large variations in parameters.

1.2.4 SCN molecular clock models

When constructing a model for the molecular clock in the SCN, two main questions must be addressed: what details of the molecular clock are included in each cell, and how are these cells arranged and coupled together? As more has been discovered about the physiology of these clock cells, so have models of the SCN increased in complexity.

Achermann and Kunz [2, 68] created one of the earliest SCN models, based on 10,000 coupled Van der Pol oscillators with a distribution of natural periods. This model is very simplified, with no direct connection to the actual biochemistry involved. The cells were

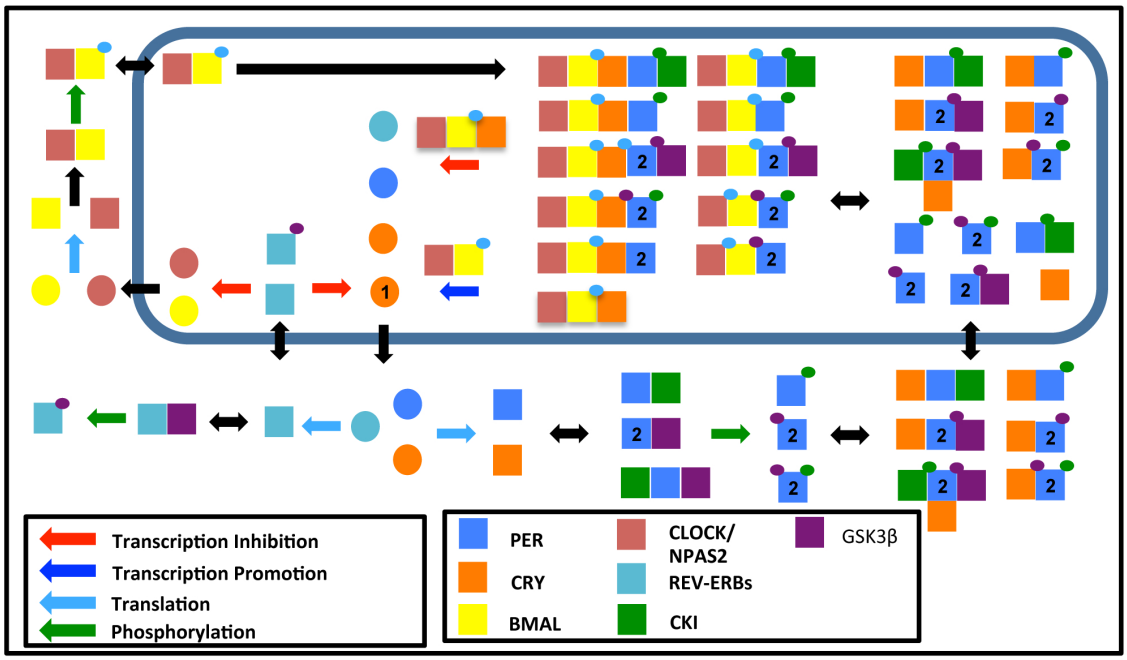

Figure 1.3: Schematic of the main components of the detailed circadian model by Kim and Forger (reproduced from [60]). Large circles represent mRNA molecules, squares represent proteins, and small circles on squares represent phosphorylations by the kinase of the same color. Blue and red arrows denote transcriptional activation and repression respectively, and other arrows denote complex formation or translocation (black), phosphorylation (green), or translation (teal) events.

coupled together using diffusive local coupling, which was shown to be sufficient for synchronizing the cells. This model includes no physiological information specific to the SCN. Additionally, a cylindrical boundary was used in which the top and bottom rows of the lattice were identified. These periodic boundary conditions are not physiologically realistic, and furthermore, make it simpler to generate synchronization.

A slightly more detailed model, proposed by Gonze et al. [46], is based on 10,000 Goodwin-type biochemical oscillators. These oscillators are coupled by releasing a signaling molecule which is assumed to diffuse quickly, so that the entire SCN is influenced by the mean field value of the signal. The 10,000 cells are then split into two populations, representing the dorsomedial (DM) and ventrolateral (VL) regions of the SCN. However, this is again done using mean field coupling, and includes no details about the spatial

arrangement of the cells within the SCN.

In an improvement on the Gonze model, Bernard et al. included a bit more of the molecular biology of the intracellular oscillations, as well as some of the SCN spatial heterogeneity: cells were placed on a lattice, with a separation of the left and right halves of the SCN, a distinction between the DM and VL regions, and a gradient of intrinsic periods of the oscillators from the DM toward the VL regions, with the shortest periods in the DM region [15]. The intracellular oscillations were based on the Becker-Weimann model, with the addition of an intercellular signaling molecule which activates a 2-step cascade, leading to increased Per/Cry expression. The model contained 309 independent oscillating cells with varying connectivities enforced through the signaling molecule which has direct, rather than diffusive effects [7]. This is again an improvement over the global, mean field coupling.

Both the Bernard and Gonze models claim that an individual cell receiving the average level of signal molecule would show damped oscillations, and that by bringing cells out of the oscillatory regime, the signaling molecule is better able to synchronize the entire array of cells.

Around the same time, To et al. [124] published an SCN model based on the Leloup and Goldbeter single-cell model. As in the Bernard model, they used a coupling agent which acts through direct, local coupling in order to link the cells and form a network model. Simulations of this model showed that the coupling agent was sufficient for synchronizing the cells even when only 40% of the individual cells were intrinsically rhythmic. Additionally, if the coupling agent was not produced by the cells, but rather was applied as a periodic pulse (24 hour period), then this was again sufficient for causing a majority of cells to be rhythmic, and creating a synchronized rhythm across the population. This model contained no spatial information, and the effects of the signaling molecule on cel-

lular periods do not seem to match experimental data.

Each of the models presented above use simplified intracellular clock models, based on Van der Pol or Goodwin type oscillators. Of them all, only the Bernard model produced spatiotemporal simulations similar to experimental results. The Bernard model is however quite simplified, and does not use experimental data to fit model parameters.

1.2.5 Full SCN models

To date, no studies have looked in depth at the full dynamics of the molecular clock and the electrophysiology in the SCN. A first attempt in a single cell was performed by Vasalou and Henson [129], who combined a firing rate code model to a basic molecular clock model by Leloup and Goldbeter [72] using a modified version of the model for signal-induced Ca^{2+} oscillations by Goldbeter et al. [45]. This model has the disadvantage that it does not resolve any of the firing dynamics, but rather derives an algebraic expression for a generalized average firing rate. In this expression, ionic conductances are considered to be constant on 10 minute time steps. In addition, Hill-type expressions are used in many of the model equations, especially for the currents, usually to try to fit experimental data. As the authors admit however, these do not express any meaningful mechanistic relationships, which lessens the predictive power of the model. In some cases, a mechanistic relationship is implied, but it is not clear what the physiological implications of such an expression would be. For example, VIP is assumed to be released as a Hill-type function of firing rate with an exponent of 1.9.

Vasalou and Henson also used this model as the basis of a multicellular model [131]. They simulated 400 cells with heterogeneous properties, such as ability to oscillate in isolation, length of intrinsic period, neurotransmitter release, and intercellular coupling. Coupling was mediated through GABA and VIP, and small world connectivity was assumed. While the authors show that their model generates synchronized activity, the actual be-

havior of the SCN is not this straightforward; there is actually a phase wave that travels across the SCN. Additionally, both the single-cell and multicellular models predict that all of the clock cells show rhythmic firing rates peaking in the afternoon. Because they do not simulate the specifics of the electrical activity, they do not account for the large cohort of SCN cells (the “Per1 cells”) that have been shown to not fire at all in the afternoon, and have alternate depolarized electrical states [14].

CHAPTER II

Network properties of the molecular clock

Portions of this chapter were published in: DeWoskin et al., It is not the parts, but how they interact that determines the behaviour of circadian rhythms across scales and organisms. *Interface focus*, 4(3):20130076, June 2014 [29].

2.1 Introduction

The roughly 20,000 neurons of the suprachiasmatic nuclei (SCN) form a circuit that times daily (circadian) events in mammals. Each of these neurons can independently function as a clock, measuring time using genetic feedback loops in transcription and post-translational modifications that generate rhythms in clock protein levels. The concentrations of these proteins oscillate with a period around 24 hours. While many of the cellular components of this timekeeping system have been identified, the way in which interactions between cells within the SCN contribute to the generation of robust rhythms at the tissue level remains to be investigated.

Previous studies of the circadian timekeeping system have shown that coupling between cells can help heterogeneous neurons with weak, damped oscillations [15, 124] or only stochastic oscillations [62] to generate rhythms as a synchronized network. Coupling has also been shown to affect the ability of the network to entrain to external stimuli [1]. While several previous models of the SCN have been built [42, 60, 15, 124, 85, 46, 12, 107,

31, 72, 129, 130], generally many of the details of transcriptional and post-translational regulation that are essential for timekeeping are left out. Additionally, the role of coupling between cells in the model is important for fitting parameters, but is often not considered.

We aim to match experimental measurements of the SCN from both the dispersed cell culture (uncoupled neurons) and organotypic slice preparations (coupled neurons). SCN slices contain a 2-dimensional array of neurons, each of which could generate timekeeping. To represent the intracellular rhythms, we use the Kim and Forger model [60] for the mammalian circadian clock, which includes detailed descriptions of complex formation, and transcriptional regulation by the repressor complexes formed. We chose the Kim and Forger model because of its detail and predictive accuracy. We first extend the Kim and Forger single-cell model to make a detailed multicellular model of the SCN. We then use the multicellular SCN model to explore how differences in phenotype between dispersed SCN neurons and the SCN network are generated.

Most mathematical models of intracellular clocks model a single cell, but are routinely compared with experimental data from collections of cells. Here, we develop a detailed biochemical model of the SCN, fit parameters that incorporate intercellular coupling to population data, and then compare the result to the same model when coupling is removed. Our goal is to use the model to understand how intercellular signaling leads to emergent phenomena at the network level. We find that refitting the model in this way yields different dynamics and makes an interesting prediction that also matches experimental data: individual cells are bistable, and network coupling removes this bistability and causes the network to be more robust to external perturbations. We propose that the interactions between cells in biological timekeeping networks are carefully tuned towards proper function.

2.2 Methods

2.2.1 SCN model formulation

We first extend the Kim and Forger model of intracellular rhythms in the SCN to a tissue-level SCN model by incorporating intercellular signaling through the neuropeptide vasoactive intestinal peptide (VIP). VIP has been reported to be the most essential signaling molecule in the SCN, and is required for generating stable, tissue-level synchrony [79, 5, 8, 48, 19, 103]. VIP is released by roughly 20% of the neurons of the SCN, and received by the cell-surface $VPAC_2$ receptor ($VPAC_2R$). This receptor has been shown to be present on the surface of upwards of 90%, if not all cells in the SCN [6], so we will assume all cells can receive VIP. Reports about whether VIP is produced rhythmically or not conflict [143, 55, 87], but it is generally agreed upon that VIP release should be rhythmic [114], so we focus only on VIP release.

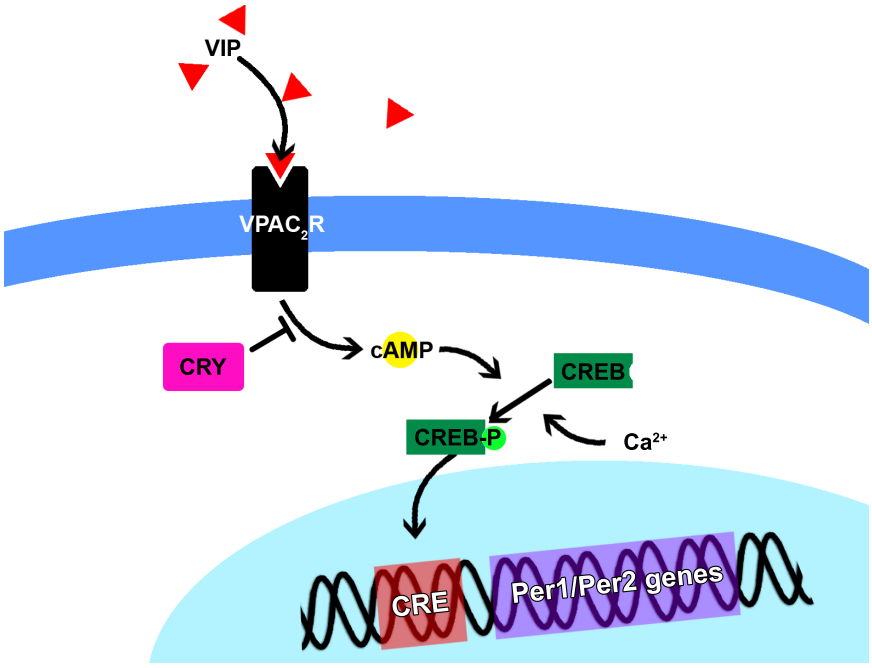

Figure 2.1: Diagram of the steps of the CRE activation pathway included in the model. Binding of VIP to the cell-surface receptor $VPAC_2R$ leads to increases in cAMP, which together with intracellular calcium promote the phosphorylation and activation of CREB. CRY non-competitively binds the intracellular domain of $VPAC_2R$, inhibiting it. Activated CREB binds to CRE sites on the promoters of the *Per1* and *Per2* genes increasing their transcription.

Binding of VIP to the receptor initiates an intracellular signaling cascade with several steps occurring on a very fast time scale. Condensing this fast timescale, we model only the ligand-receptor binding and a few key steps in the pathway for which we have experimental data to compare (see Figure 2.1). Specifically, we assume that VIP binding to the receptor leads to an increase in cAMP, which promotes phosphorylation and activation of CREB. The activated CREB then binds to the CRE sites in the promoter regions of the *Per1* and *Per2* genes, increasing their transcription [125]. The rate of VIP release is assumed to be proportional to intracellular calcium levels, and calcium can also, through a parallel pathway, promote the phosphorylation of CREB directly [97]. Intracellular calcium is assumed to increase at a rate proportional to E-box activity, and decrease at a linear rate. While this is a purely phenomenological assumption, it is consistent with experimentally measured time courses of intracellular calcium, which show the greatest increase roughly at the time of maximal E-box activity [18, 34], and creates a phase difference between calcium and the molecular clock components consistent with those found experimentally as well as in previous modeling studies [31]. Finally, CRY1 and CRY2 are assumed to inhibit the adenylyl cyclase activity of $VPAC_2R$ [144]. This pathway is diagrammed in Figure 2.1, and all equations, variables, and parameters modified from the original Kim and Forger model, or added to make this new model are given in appendix A.1.

2.2.2 Parameter estimation with GPUs

The addition of intercellular signaling to the Kim and Forger model requires the fitting of 15 new parameters. To represent a single cell, *Per1* and *Per2* maximal E-box transcription rates (parameters trPo and trPt) were set to 40% of their originally published maximal values, as recommended in the original manuscript, and all other original parameters were unchanged [60]. This was done to allow for additional *Per* transcription initiated by CRE activation through VIP and calcium.

The 15 new parameters were fit to the protein and mRNA time courses and protein abundance data that the original model was fit to, as well as additional time courses of intracellular calcium and CRE activity levels extracted from published videos [18] using Matlab. These data were used to generate a cost functional (given in appendix A.2) which was minimized by simulated annealing as in the original Kim and Forger publication [60]. In order accelerate the parameter fitting process, 1024 instances of simulated annealing were run in parallel on a GPU card. The GPU architecture is well suited for this problem because parameter estimation using simulated annealing is embarrassingly parallel and fits entirely within the memory onboard the GPU card. The number 1024 was chosen specifically for this problem and our particular GPU card (specifics of which are given below), as tests showed that it was a near optimal choice in terms of speed of computation per number of concurrent tests (Figure 2.2). Note that this optimum is problem specific.

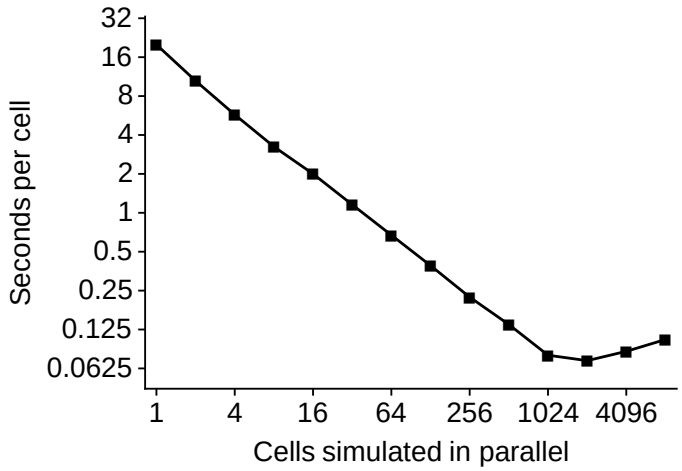

Figure 2.2: Wall time needed to simulate 48,000 time steps of the extended single-cell ODE model as a function of the number of concurrent cells run in parallel on the GPU card. The minimum amount of time per cell was achieved for 2048 cells simulated in parallel.

To fit the new parameters in parallel, an array of length 1024 was allocated on the GPU card for each state variable and each parameter, with the indices representing 1024 independent, uncoupled cells. Elements of a state variable array were initialized with identical initial conditions and arrays for parameters from the original model were all

initialized to their published values (with the exception of trPo and trPt which were set to 40% of their published values as mentioned). The arrays for the 15 new parameters were initialized with random perturbations of reasonable initial guesses, normally distributed with standard deviations 8% of the mean. For fitting purposes, cells were coupled to themselves, so that each cell received only the VIP that it produced. This was necessary to allow fitting of the activation of the CRE pathway by VIP in a single cell. The independent ODE models for each cell were solved in parallel by assigning each of the 512 threads to solve the equations for two cells. The standard 4th order Runge-Kutta method was used, as it has a fixed time step, which was necessary in order to maintain synchrony between threads.

In the simulated annealing iterative algorithm, in each iteration, the ODEs were solved, and then costs for each of the 1024 parameter sets were calculated, and compared only to the parameter sets at the same index from previous iterations. A new parameter set at a locus was accepted automatically if its cost was lower than the previously accepted one, and with probability $0.5 \exp(-k/10)$, where k is the number of the current iteration, if its cost was higher. The next parameter set at each locus in the array was then generated from the previously accepted one at the same locus by random perturbation. This process was repeated, until eventually 1024 candidate parameter sets remained at the end of the simulated annealing procedure. A final parameter set was then chosen by selecting the set with the lowest cost that also produced the correct mutation phenotypes for both the single-cell and network models (as in [60]). Fits of the model to experimental data obtained are shown in Figure 2.3.

Parameter fitting and subsequent model simulation was performed on a dedicated server with 16 2.20 GHz Intel(R) Xeon(R) E5-2660 CPU cores and two NVIDIA M2090 GPU cards with compute capability 2.0. All code for the GPU was written by the author in

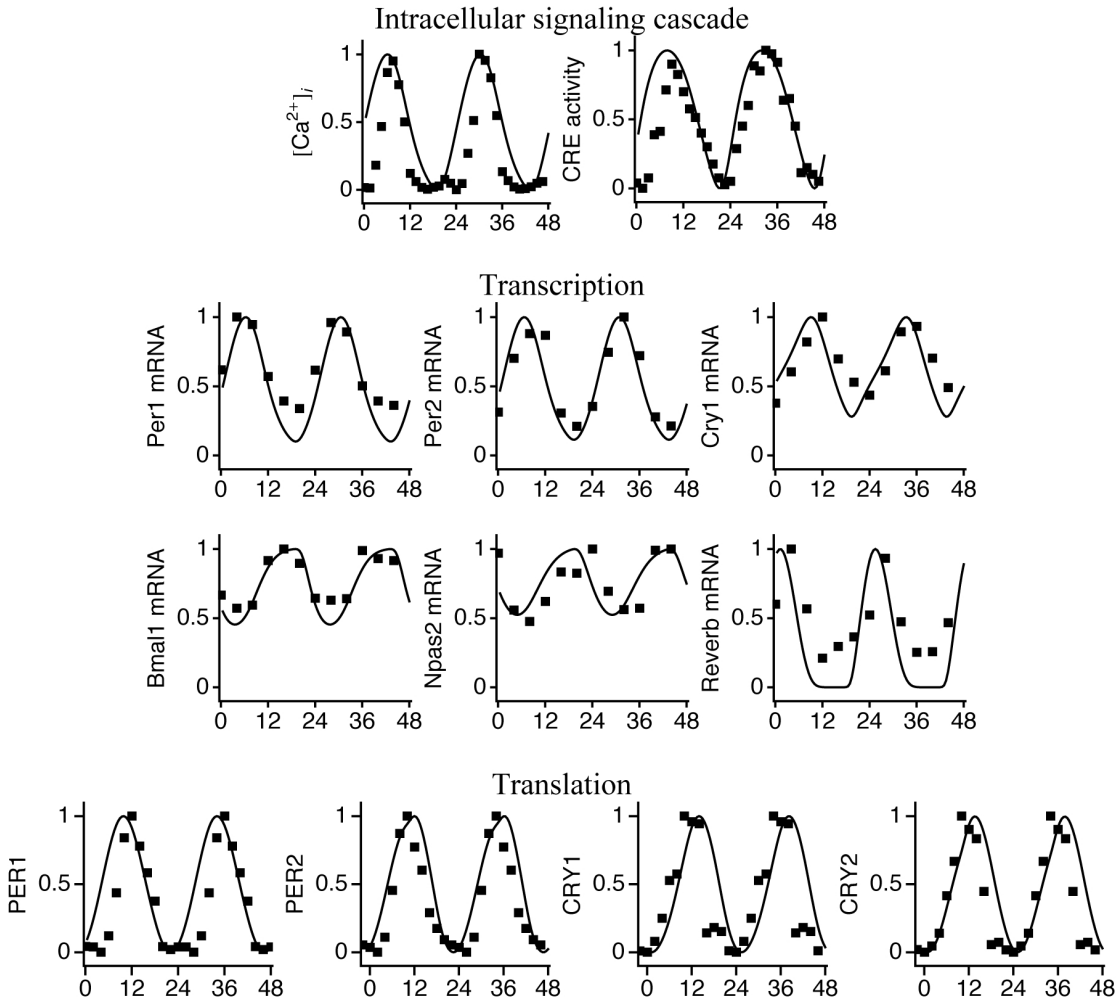

Figure 2.3: Fits of the extended single-cell model to mRNA, protein, CRE activity, and Ca^{2+} time series. Model predictions are shown as smooth curves, and experimental data as squares. All time series are normalized by their maximum values. mRNA and protein time series are the same as used in [16]. CRE and Ca^{2+} time series extracted from videos in [59].

CUDA C, release 5.0, and compiled using nvcc (version V0.2.1221) and gcc (version 4.4.6). Each simulation was performed on one dedicated GPU card. An equivalent CPU implementation of the parameter estimation routine written in C with an identical data structure setup and numerical method as the GPU version (but with scalar doubles in the place of the arrays used for the parallel implementation), run on the same server, solved the system of ODEs for one cell for 48,000 time steps in a wall time of 1 second. The GPU version solved the system for 1024 cells in parallel for an equal number of time steps in

81 seconds, roughly 12.6 times as fast.

2.2.3 Simulating the SCN model with GPUs

We simulate an SCN network model of 1024 cells in total, and assume that VIP is produced by 205 ($\sim$20%) of the cells. For simulation of the whole SCN, the VIP released by each cell is divided by the number of VIP producing cells, so that the input signal from the network is on the order of the originally fit VIP level. VIP is a small neuropeptide, which should diffuse rapidly throughout the SCN compared to the timescale of transcriptional activation. Therefore, we make the simplifying assumption that the VIP producing cells released VIP equally to all cells in the SCN. To test the consequences of this assumption, we compared the time courses obtained with this connectivity to those seen with random network connectivity of varying percentages ranging from 10% to 100%, normalizing the VIP input to each cell by the number of upstream cells, and saw no significant difference in synchrony, period, amplitude, or waveform.

Heterogeneity is included in the model by allowing the *Per1* and *Per2* maximal transcription rates associated with both E-box activation (parameters trPo and trPt respectively) and CRE activation (parameters CtrPo and CtrPt respectively) to vary between cells. For each cell, these four parameters were drawn independently from normal distributions with mean equal to the value from our fit single-cell model, and standard deviation 5% of the mean. This affects the strength of oscillations seen in individual cells as well as their intrinsic periods of oscillation. Only these transcription rates were varied between cells; all other parameters were set to the values fit as described above.

The SCN network model was simulated using GPUs with exactly the same data layout as for parameter estimation. As such, we choose to use a 1024-cell network as before. The only difference with the network simulation is that it requires some communication between threads. In particular, information about intercellular coupling through VIP must

be passed between cells. This is a small amount of data relative to the computation of the intracellular dynamics, which can be solved in independent blocks, but requires additional consideration in order to not unnecessarily slow the computation.

To couple the cells, we define a connectivity matrix C, where $C(i, j)$ is 1 if cell j projects to cell i, and 0 otherwise. VIP released by a cell is assumed to be proportional to the intracellular calcium levels of the cell. Thus, to get the VIP received by a cell at a time step, we multiply the matrix C by the column vector containing the intracellular calcium levels in all cells. This gives a vector whose j-th entry is the VIP released to cell j at this time. For our 1024-cell SCN network, this requires the multiplication of a 1024×1024 matrix by a 1024×1 column vector, which is time-consuming, and must be done four times at every time step in the 4th order method used to solve our ODE model. To accelerate this process, we use the cuBLAS package of GPU optimized linear algebra routines. The cublasDgemv matrix-vector multiplication function speeds up the simulation of our 1024 cell model by 2.2 times compared to our original naïve implementation in which we parallelized this operation on the GPU card as 1024 dot products. The increase in speed depends on the number of cells simulated, and in this case, greater speedup is seen for larger networks. A comparison of the two methods for networks of various sizes is shown in Figure 2.4.

2.3 Results

2.3.1 SCN network rhythms are more robust than single cells

We consider our model both in the presence of, and absence of coupling through VIP. Raster plots of PER2 levels for 200 randomly selected cells (out of 1024) from the coupled SCN model are shown in Figure 2.5(a). Cells within the intact SCN have well-synchronized, high-amplitude rhythms. The uncoupled model mimics the dispersed cell

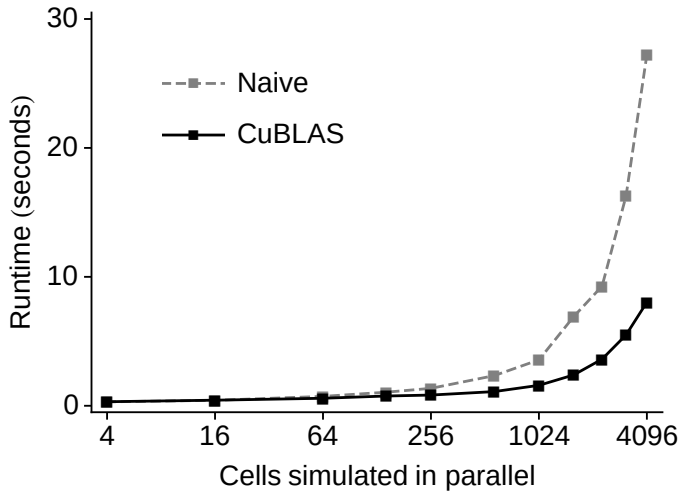

Figure 2.4: Comparison of runtimes for 40,000 time steps of the multicellular model using two different methods for calculating VIP coupling. Calculating coupling for a network of N cells in a 4th order numerical method requires multiplying an $N \times N$ matrix by an $N \times 1$ vector four times at every time step. The optimized cuBLAS matrix-vector multiplication routine greatly speeds up this computation for large networks, in comparison with a naïve implementation performing N dot products in parallel.

preparations often used experimentally. In these simulations, the VIP release rate (parameter vpr) is set to zero, as cells are assumed to be dispersed enough that they are unable to signal through VIP. Raster plots of PER2 levels for the uncoupled model are shown in Figure 2.5(b). In the absence of coupling, the cells desynchronize and show a drastic reduction in rhythm amplitude, with some losing rhythmicity altogether. While the uncoupled cells all begin with similar initial conditions, they drift apart over time due to their differences in intrinsic periods. Periods of individual cells range from 24.0 to 25.6 with a mean of 24.79 $\pm$ 0.29, and are distributed roughly normally. Of the 1024 isolated cells simulated, 966 showed sustained rhythms while the other 58 were arrhythmic or heavily damped.

Consistent with the original model [60], we find that our uncoupled model matches known single-cell genotypic knockouts: 70% of *Per1*$^{-/-}$ and all *Cry1*$^{-/-}$ cells modeled were arrhythmic, while *Cry2*$^{-/-}$ cells were mostly rhythmic (918 of 966 rhythmic) with a long period (mean 27.13 $\pm$ 0.38 hours). This is all consistent with experimental data

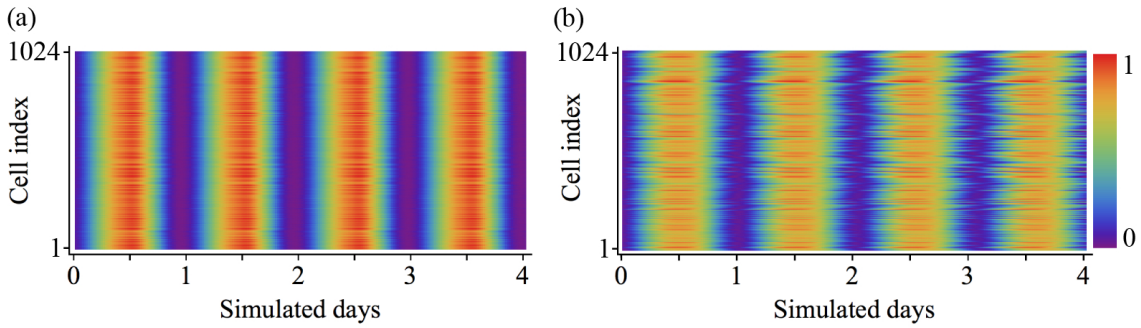

Figure 2.5: PER2 rhythms in the simulated SCN. (a) Raster plots of 200 cells selected randomly from the 1024 cells in the simulated SCN. Each row of the raster plot shows the total PER2 protein level vs. time for one cell. Cells are all well synchronized throughout the simulation. (b) Raster plots from a simulation of uncoupled cells shows that without VIP signaling, neurons drift out of phase as time progresses due to differences in intrinsic period. PER2 levels are normalized within each panel and displayed according to the color scheme at the right. Cells are indexed from top to bottom in random order.

for SCN neurons in dispersed culture [76]. In the coupled SCN model with intact VIP signaling, cells synchronize with a period of 24.2 hours, consistent with SCN explants [76]. Unlike the isolated cells, the network model is resistant to genotypic knockouts, showing robust rhythms in $Per1^{-/-}$, $Cry1^{-/-}$, and $Cry2^{-/-}$ individual knockouts, with no period change, period shortening by ~1 hour, and period lengthening by ~1.5 hours respectively for the three knockouts.

2.3.2 Network rhythms are less susceptible to perturbations

To test the robustness of individual cellular rhythms, we constructed a phase response curve (PRC) to VIP to see how the phase of cellular rhythms shifts in response to external signaling. For this curve, circadian time was determined relative to the cell's PER2 protein level, with the peak PER2 level defined as CT12. Individual cells can show both large phase advances as well as delays depending on the time at which the VIP is applied, and surprisingly can also be made arrhythmic (denoted as a gap in the PRC). A PRC for a single cell is shown in Figure 2.6(a). For this particular cell, a VIP pulse between CT17.3 and CT20.5 causes the cell's rhythms to damp (Figure 2.6(c)), in stark contrast

to the quickly recovered rhythms when the pulse is given at other circadian times (Figure 2.6(d)). This bistability was surprising, as it had not been seen with the parameters used in the original Kim and Forger model, and is a novel prediction of our new single cell model. It is, however, consistent with experiments which have shown that application of forskolin, a direct stimulant of the cAMP signaling pathway, to isolated SCN neurons can cause the cells to gain or lose rhythmicity [135]. Other models have also found this behavior, notably in the light response of the *Drosophila* circadian clock [71] and in a particular range of parameters in an overall model of mammalian circadian rhythms [73].

VIP pulses of identical magnitudes applied to the SCN network show much smaller phase shifts, with a traditional type I PRC, as described in [139], shown in Figure 2.6(b) (note the difference in scale). Thus the intercellular coupling confers robustness against external perturbations. The SCN network PRC qualitatively matches that found experimentally [5], with roughly the same pattern of advances and delays. The main notable difference is that the magnitude of the phase delays is not as great as in [5], which could be explained by the pharmacokinetics of VIP, or small differences in the magnitude of the VIP pulse given, as compared to our simulations.

2.3.3 Coupling restores robust rhythms to bistable isolated neurons

To explore this bistability in single cells further, we tested if the reintroduction of VIP signaling could restart collective rhythms in the network. Using our uncoupled model from before, we began with half the cells in the rhythmic state and the other half in the arrhythmic state, and reintroduced VIP signaling. Plots of 32 representative cells from the 1024 in the network with varying initial amplitudes (with bright to dark colors representing low to high initial amplitudes respectively), and phases are shown in Figure 2.6(e). After restoring VIP signaling (time denoted by the red vertical line), all of the cells in the network quickly regained high amplitude rhythms, and resynchronized over time. This il-

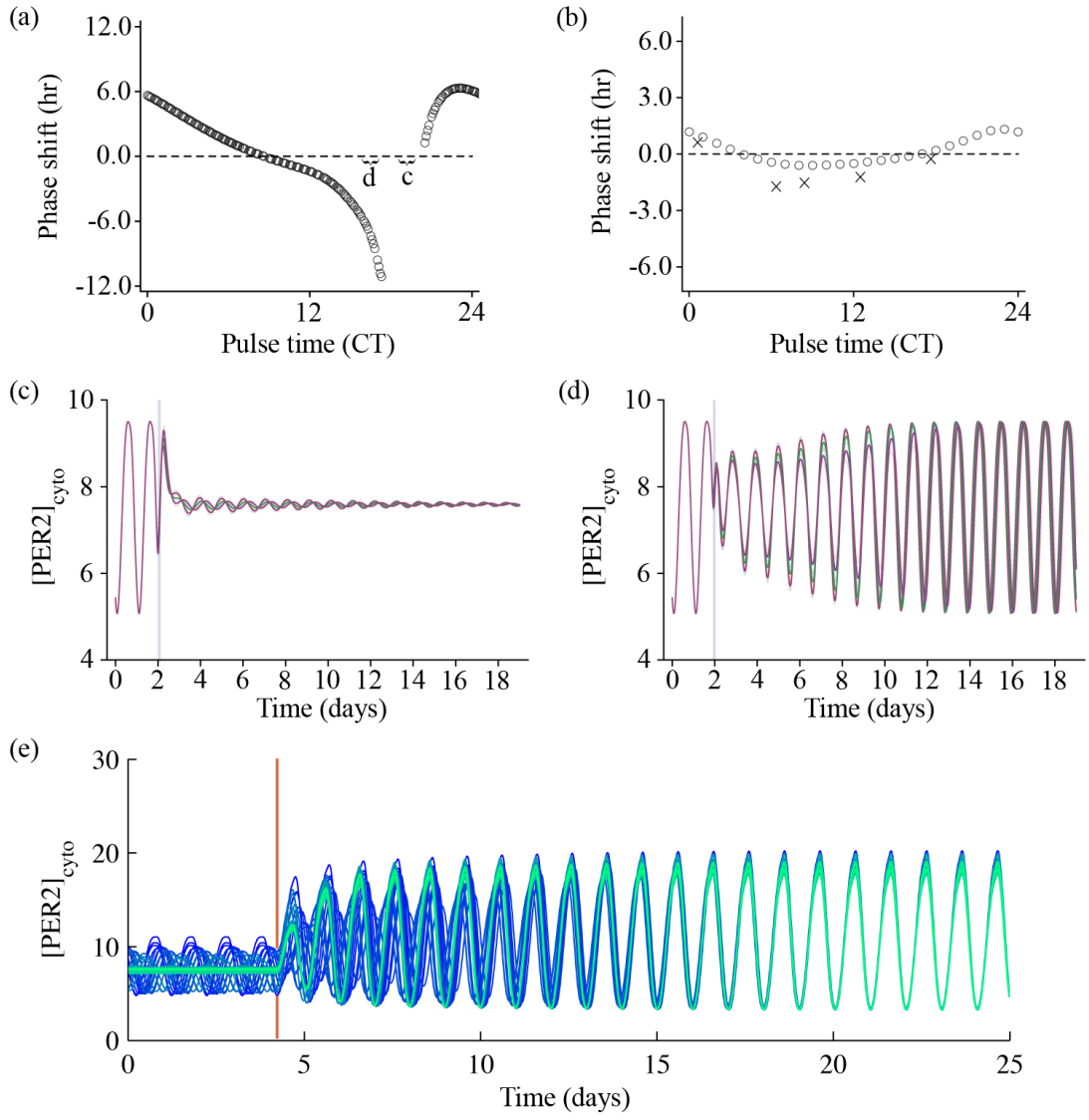

Figure 2.6: Effect of VIP on individual cells and the SCN network. Phase response curves (PRCs) predicted by the model for (a) a single cell and (b) the SCN network (circles) in response to a VIP pulse show that single cells can be shifted much more easily than the SCN network (note the difference in scales). Experimentally determined phase shifts for application of 100nM VIP to the SCN from [47] are labeled as x's in panel (b) for comparison. VIP pulses given to the single cell (labeled as regions c and d in panel (a) and denoted by gray vertical lines) can either (c) cause the cell to become arrhythmic or (d) phase shift it. In particular, pulses between CT17.3 and CT20.5 cause the cell to lose rhythms, shown as a gap on the PRC (single cell parameters are given in the Supplementary Material). (e) Restoring VIP signaling (denoted by a red vertical line) to an uncoupled network of half rhythmic (blue), half arrhythmic (green) cells quickly restores rhythms and synchrony to the network.

lustrates the fact that bistability is not seen in the coupled network, but rather is only seen in isolated cells.

2.4 Discussion

The development of detailed multicellular models of biological tissues has the potential to explore many complicated phenomena seen experimentally, and to try to explain the mechanisms behind them. Here, we develop a multicellular model of the mammalian circadian clock, and study the differences in timekeeping between single neurons and the intact neuronal network. We show how coupling between cells can greatly increase the amplitude of network-level rhythms, and additionally make them resistant to perturbations, both of which are in agreement with experimental findings [21, 142, 79]. Most interestingly, we find that when cellular coupling is included in model fitting, individual cells lacking the coupling signal become bistable. This matches data which shows that timekeeping within individual isolated neurons within the SCN can be turned on or off by biochemical signals [135]. It also raises questions about our single cell simulations of circadian mutants, and the data that we compare our simulations against [76]. When single cells are found to be arrhythmic, it remains to be seen if that is due to bistability or if the cells are actually incapable of rhythmicity. This needs to be explored both in simulations and in the experimental preparation.

The findings here are in line with the original Kim and Forger study which showed that a 1:1 stoichiometry between transcriptional activators and repressors was essential for generating robust rhythms in the model [60]. In the original model, transcriptional activation was due to E-box activity alone. In the extended model developed here, we add transcription due to CRE signaling and correspondingly reduce the transcriptional drive from E-box activity in individual cells. In the absence of signaling, isolated cells, therefore, are predicted to have decreased transcriptional activation and a less than 1:1 stoichiometry, leading to reduced rhythmicity. In the intact network, the transcriptional drive is

supplemented by CRE activation by VIP, restoring the balance needed for robust rhythms. Thus we find that bistability in intracellular timekeeping due to a loss of transcriptional activation makes timekeeping vulnerable to perturbations, and can be compensated for by intercellular coupling.

With our SCN model, we focused on the molecular mechanisms of rhythm generation. In the actual SCN, there is a strong connection between the molecular clock and the electrical activity of the cells [14], and previous studies have shown that the rhythms in electrophysiology can strengthen molecular rhythms [31]. This aspect of rhythm generation here will be explored further in chapter III.

Another important area for continued work is to study the differences in phase among neurons in the SCN network. Heterogeneity of period and phase within the SCN have been shown to be important for the coding of seasonal changes in light and dark cycles [91, 54, 37]. Previous studies have shown that cells in subregions of the SCN exhibit differences in intrinsic period [91, 96, 95, 63], and some have suggested that these period differences drive the spatiotemporal pattern or "phase wave" seen in SCN slices [63]. A mechanism for encoding seasonal time in the phase distribution between SCN subregions will also be further discussed in chapter IV.

CHAPTER III

Signaling across timescales in the SCN network

Portions of this chapter were published in: DeWoskin et al., Distinct roles for GABA across multiple timescales in mammalian circadian timekeeping. *Proceedings of the National Academy of Sciences of the United States of America*, 2015 [30].

3.1 Introduction

The multicellular molecular clock model of the SCN developed in chapter II was sufficient to explore many of the important differences between protein rhythms in single SCN neurons and the SCN network, but it lacked one very important additional level of detail: neuronal electrical activity. SCN neurons show a variety of electrical activities throughout the day including hyperpolarization block, firing action potentials at various frequencies, depolarized low amplitude membrane oscillations (DLAMOs), and depolarization block (see Figure 1.2). These distinct electrical states are thought to be essential for both coordinating molecular rhythms within the SCN network, as well as in providing the output signal from the SCN to other brain regions. Modeling this activity, however, provides a computational challenge as it must be coupled bidirectionally with the molecular clock [67, 84, 105, 31], but occurs on a much faster timescale with important behaviors happening over milliseconds.

Much of the fast electrical activity is coordinated through intercellular signaling medi-

ated by the neurotransmitter γ-aminobutyric acid (GABA). GABA is of particular interest in the SCN because of all the neurochemicals of importance for synchronization of tissue-level rhythms and intercellular signaling [79], only GABA is both produced and received by all, or nearly all SCN neurons [86, 77]. Despite its ubiquity, the role of GABA in the SCN is still not well understood. While GABA-elicited post-synaptic currents (PSCs) are generally hyperpolarizing (inhibitory) in most parts of the brain, in the SCN they can also be depolarizing (excitatory) [3, 44, 24, 4, 28, 132, 39]. Interestingly, the response elicited by a GABA signal is determined by the state of the receiving cell (dependent on its intracellular chloride concentration [39]), so that GABA released by a neuron can both excite and inhibit different downstream cells at the same time. Furthermore, the fraction and location of the GABA-excited SCN neurons is still debated.

GABA has been shown to synchronize SCN rhythms [77] and is necessary for the synchronization of SCN subregions after disruption by light [37], phase shifts of the light/dark cycle [4, 106], or the compromising of molecular rhythms [62]. On the other hand, other studies have found that GABA actively opposes synchrony by injecting jitter into rhythms [44] and that blocking GABA receptors increases synchrony in SCN slices [91], and peak firing rates, rhythm amplitude, and precision of cultured SCN neurons [9]. Thus, the work of well-respected labs seems to produce opposite results on whether the primary signal in the SCN acts to synchronize, desynchronize, inhibit or excite SCN neurons.

To investigate the role of GABA in the SCN, we use an integrative approach combining experiments and mathematical modeling. Since the electrical activity of an SCN neuron depends on the state of its molecular clock, and vice versa, we require a multiscale SCN model, which we construct by incorporating SCN electrical activity [31] into each cell of the multicellular molecular clock model [60, 29] developed in chapter II. This new multi-scale model of the SCN network is able to resolve both the molecular events generating in-

tracellular rhythms and the electrical activities of each cell in the network down to individual action potentials. With it, we are able to simulate the billions of GABA PSCs that occur daily within the SCN, and predict their effect on the synchrony of molecular rhythms. Despite numerous modeling studies [15, 46, 124, 107, 72], with some even describing GABA [129, 131], no previous model has been able to resolve the effects of GABA on their natural timescale of milliseconds, which is integral to understanding GABA's role in circadian timekeeping. We show how to simulate this detailed model utilizing the framework for parallelizing cellular network models on GPUs described in section 2.2.3. Additionally, we utilize numerical methods that take advantage of the difference in timescales between the molecular and electrical activities and the coupling structure of the ODE systems. We show how this model, combined with novel physiological data, can resolve much of the controversy surrounding GABA in the SCN, and can be used to study both signaling within the tissue and control of its output.

The model predicts that GABA signaling has two components: phasic (fast) and tonic (slow). Phasic GABA post-synaptic currents are released after action potentials, and can both increase or decrease firing rate, depending on their timing in the interspike interval, a modeling hypothesis we experimentally validate. This allows flexibility in the timing of circadian output signals. Phasic GABA, however, does not significantly affect molecular timekeeping. The tonic GABA signal is released when cells become very excited and depolarized. It changes the excitability of neurons in the network, can shift molecular rhythms, and affects SCN synchrony. We measure which neurons are excited or inhibited by GABA across the day and find GABA-excited neurons are synchronized by, and GABA-inhibited neurons repelled from this tonic GABA signal, which modulates the synchrony in the SCN provided by other signaling molecules. These findings suggest a novel mechanism of signaling in the brain, in which a single signaling molecule can have dif-

ferent effects on different timescales depending on its profile of release. Additionally, our mathematical model provides an important framework for the many multiscale projects currently studying brain function.

3.2 Multiscale model formulation

In chapter II, we used a detailed model of the molecular clock in a single cell [60] as the basis for a multicellular SCN model with intercellular signaling through the neuropeptide vasoactive intestinal peptide (VIP) [29]. Here, we greatly extend the multicellular model to make it multiscale by including: each cells electrophysiological activity, coupling between the molecular clock and electrical activity within each cell, and GABAergic signaling between the cells in the network. The connections between each of these components within a model cell are shown in Figure 3.1, and are explained in detail in the following sections. We break down the multiscale SCN network model into its four components: 1) the electrophysiology model (section 3.2.1), 2) the GABA coupling model (section 3.2.2), 3) the molecular clock model (section 3.2.3), and 4) the VIP coupling model (section 3.2.3).

Briefly, molecular clock phase (determined by E-box activity) controls two potassium channel conductances (gKCa and gK-leak) leading to circadian variation in the resting membrane voltage and electrical activity of the cell. Membrane voltage can be further increased or decreased due to GABA signaling, with the polarity dependent on the GABA reversal potential (E_{GABA}) of the cell. Membrane voltage affects intracellular calcium concentrations, which can cause Per transcription via CREB phosphorylation and subsequent activation of the CRE site. In simulations including VIP, VIP is assumed to be released only by 10% of the ventral SCN neurons. In these cells, VIP release is assumed to be dependent on intracellular calcium. VIP is assumed to diffuse quickly across the

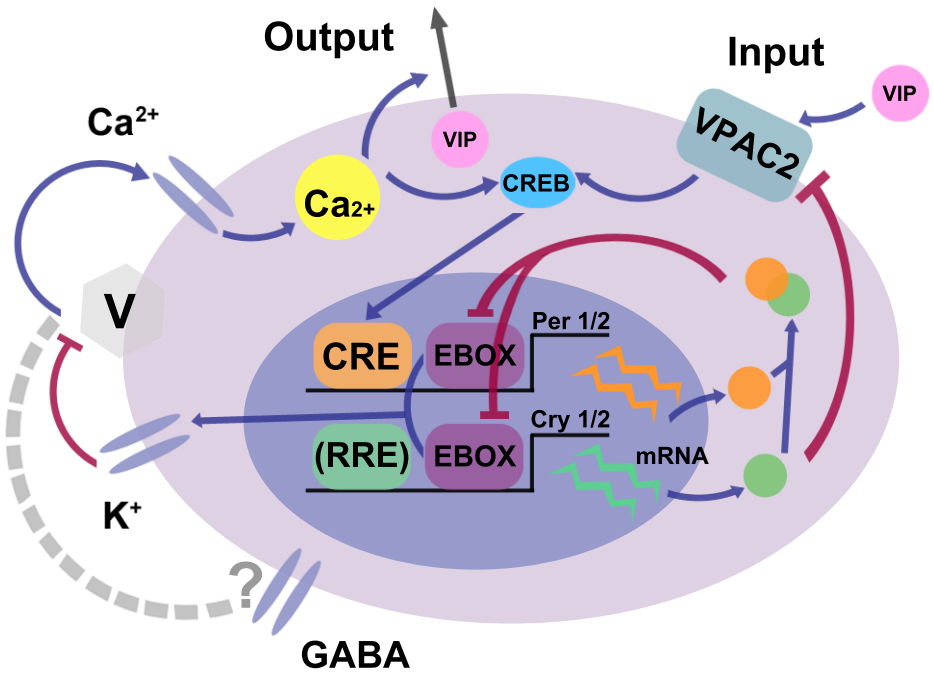

Figure 3.1: Interactions between components of the SCN model. The full SCN model contains both a detailed molecular clock model as well as a conductance-based electrophysiology model of the dynamics of each cell in the network. The connections between these components are highlighted here. The molecular clock state, determined by E-box activity, influences the permeability of KCa and K-leak channels. These drive changes in membrane voltage, which affect intracellular calcium concentrations. Both calcium and VIP can lead to activation of CREB, causing transcription of Per1 and Per2. Calcium also causes release of VIP in VIP producing cells. The activity of the VPAC2 receptor is inhibited by CRY. GABA can lead to excitation or inhibition of membrane voltage depending on EGABA.

SCN and is received by all cells, since all cells express the VIP receptor VPAC2 [6]. After its release, VIP binds to extracellular VPAC2 receptors leading to CREB phosphorylation and subsequent Per transcription. Finally, the activity of the VPAC2 receptor is inhibited by cytosolic CRY [144]. With these extensions, we are able to resolve all of the billions of action potentials and GABAergic PSCs in the SCN network in each simulated day, and study the effects of GABA signaling on SCN timekeeping.

All SCN network simulations presented use 1024 cells. All parameters for the molecular clock model as well as two of the electrophysiology parameters (ECa and clk) are drawn from a normal distribution with means equal to the previously fit values [60, 29]

and standard deviation 2% of the mean. This is done to allow for unbiased intercellular heterogeneity in amplitude and period, and is based on previous estimates of biochemical parameter heterogeneity in the SCN [62]. The model is deterministic and does not include intrinsic stochasticity, as has been done in some other modeling studies [62, 11]. Certainly much could be learned from studying stochasticity in this context as well, but here we first study different types of GABA signals generated by a heterogeneous population and their effects on synchrony. We delay analysis of GABAs effect on the accuracy of the clock or on stochastically generated oscillations for future work. The details of the computational methods used to simulate the model on GPUs can be found in section 3.3.

3.2.1 Electrophysiology model

The electrophysiology model is an 11 variable conductance-based ODE model, which includes membrane voltage (V), 8 gating variables ($m, h, n, r_L, r_{NL}, f_{NL}, s, y$), the cytosolic calcium concentration (Ca_c), and the calcium concentration in a small shell near the cell membrane (Ca_s). The model is mostly as in [31] with the addition of the GABA current. The ODEs are reproduced below:

$$
\begin{aligned}
(3.1)\quad C_M\frac{dV}{dt} &= -I_{Na} - I_K - I_{CaL} - I_{CaNL} - I_{KCa} - I_{K-leak} - I_{Na-leak} - I_{GABA} \\
&= -g_{Na}m^3h(V - E_{Na}) - g_K n^4(V - E_K) \\
&\quad - g_{CaL}r_L f_L(V - E_{Ca}) - g_{CaNL}r_{NL}f_{NL}(V - E_{Ca}) \\
&\quad - g_{KCa}s^2(V - E_K) - g_{K-leak}(V - E_K) \\
&\quad - g_{Na-leak}(V - E_{Na}) - g_{GABA}y(V - E_{GABA})
\end{aligned}
$$

$$
(3.2)\qquad \frac{dq}{dt} = \frac{q_\infty - q}{\tau_q}, \text{ for } q = m, n, r_L, r_{NL}, f_{NL}, \text{ and } s
$$

$$
(3.3)\qquad \frac{dCa_x}{dt} = -k_x(I_{CaL} + I_{CaNL}) - Ca_x/\tau_x + b_x \text{ for } x = c \text{ and } s
$$

The q_∞ and τ_q functions, as well as all parameters are as in [31]. Also as in [31], the electrophysiology is coupled to the state of the molecular clock through the conductances g_{KCa} and g_{K-leak}, which depend on E-box activity through the functions: $g_{KCa} = 198/(1 + \exp(R)) + 2$ and $g_{K-leak} = 0.2/(1 + \exp(R))$. In the original publication, R was a measure of E-box activity that varied roughly between -5 and 5. Correspondingly, we let $R = clk \cdot 11.36(G - 0.25)$, where G is the state variable for E-box activity in the detailed molecular clock model used here (see section 3.2.3) and clk is a parameter which determines the strength of the influence of the molecular clock on the electrical activity of the cell ($clk = 2.2$).

In some simulations, we also consider the effect of a channelrhodopsin (ChR2)-type current. For these simulations, a current of the form $I_{ChR} = g_{ChR} z(V - E_{Ca})$ is subtracted along with the other currents from the ODE for voltage, with $g_{ChR} = 20$ nS and gating variable z. The calcium reversal potential is used based on ChR2's high permeability to calcium and sodium [23, 92], both of which have similar reversal potentials in the model. For this reason, the ChR2 current is also added to I_{CaL} and I_{CaNL} in the ODE for intracellular calcium (Ca_c). The dynamics of the gating variable z are of the standard form: $\frac{dz}{dt} = \alpha(1 - z) - \beta(z)$ with α = 100 ms^{-1} and β = 1/15 ms^{-1} (based on τ_{off} from [138]).

3.2.2 GABA signaling model

The GABA signaling model is adapted from [36] to match post-synaptic currents seen in SCN recordings such as [64]. The GABA current that a cell receives is added to the original current balance equation for voltage from [31] as in equation (3.1) ($I_{GABA} = g_{GABA} y(V - E_{GABA})$). Here $g_{GABA} = 0.5$ is the maximal conductance, $y \in [0, 1]$ is the fraction of GABA channels open, and E_{GABA} is the cell's GABA reversal potential. Since we are particularly interested in the role of the GABA response polarity, which is

dependent on E_{GABA}, we will measure E_{GABA} experimentally (see section 3.5.2).

The dynamics of a cell's GABA channel gating variable (y) are given by:

$$\frac{dy}{dt} = a_r[T_{in}](1-y) - a_d y$$

with a_r = 5 mM^{-1}ms^{-1}, a_d = 0.18 ms^{-1}, and $[T_{in}]$ the input concentration of GABA to the cell's extracellular receptors [36]. The amount of neurotransmitter output to a downstream cell by upstream cell i, $[T_{out}]_i$, depends on the voltage of the upstream, presynaptic cell i according the the function:

$$[T_{out}]_i = \frac{T_{max}}{1 + exp(-(V_i - V_T)/K_p)}.$$

The total neurotransmitter received by a cell is summed over all upstream cells $(i = 1, ..., n)$ and normalized:

$$[T_{in}] = \frac{1}{n}\sum_{i=1}^{n}[T_{out}]_i$$

We take T_{max} = 1mM, V_T = -20 mV, and K_P = 3.0 mV in order to generate GABAergic post-synaptic currents with the amplitude and timing seen in the SCN [64]. Synaptic connectivity in the SCN is assumed to be sparse in accordance with experimental data [44]. All simulations in this chapter assume 10% random connectivity of GABAergic synapses unless otherwise noted.

3.2.3 Molecular clock and VIP signaling models

The molecular clock model was adapted from its original version [60] into a multi-cellular model along with the addition of the VIP signaling pathway in [29] as described in section 2.2.1. This previously published version [29] contained a phenomenologically fit state variable for intracellular calcium, which we now replace with the intracellular calcium calculated by the electrophysiology model (Ca_c). All other parameters are as in [29]. VIP is assumed to be produced and released by the roughly 10% of neurons in the

ventral-medial SCN, based on immunohistochemistry data shown in Figure 3.2, at a rate proportional to the intracellular calcium of VIP producing cells. It is assumed to diffuse quickly relative to the time scale of transcription and the size of the SCN, so that the rate of VIP input to all cells in the network (VIP_{in}) is the same:

$$VIP_{in} = \frac{1}{m}\sum_{i=1}^{m}(Ca_c)_i$$

where $i = 1, \ldots, m$ are the indices of the VIP producing cells (some to all connectivity). All cells are assumed to express the VIP receptor VPAC2 so that they may receive VIP [6]. The rest of the VIP signaling pathway equations are identical to as in [29] (as shown in appendix A.1.5) with the exception of the two below:

$$\begin{aligned}\frac{d}{dt}vip &= 6000 \cdot vpr \cdot VIP_{in} - uv \cdot vip - vbin \cdot (V00 + V01 + V02) \cdot vip \\ &\quad + unvbin(V10 + V11 + V12) \\ \frac{d}{dt}CREB &= 6500 \cdot Ca_c + vs \cdot cAMP - us \cdot CREB\end{aligned}$$

which are scaled for the physiological concentrations of calcium generated by the electrophysiology model.

3.3 Numerical methods

3.3.1 Operator splitting implementation on a GPU

The variables in the model are split into two disparate time scales, with the electrophysiology model evolving over milliseconds and the molecular clock changing over minutes to hours. Because of this timescale separation, we solve the models separately in a nested fashion. We first hold the molecular clock state fixed and simulate the electrophysiology model for N time steps, each of size Δt_E, until the calcium levels have reached their equilibrium. We then update the molecular clock state variables over one time step of length Δt_M, holding calcium fixed at the previously found level. We repeat this process

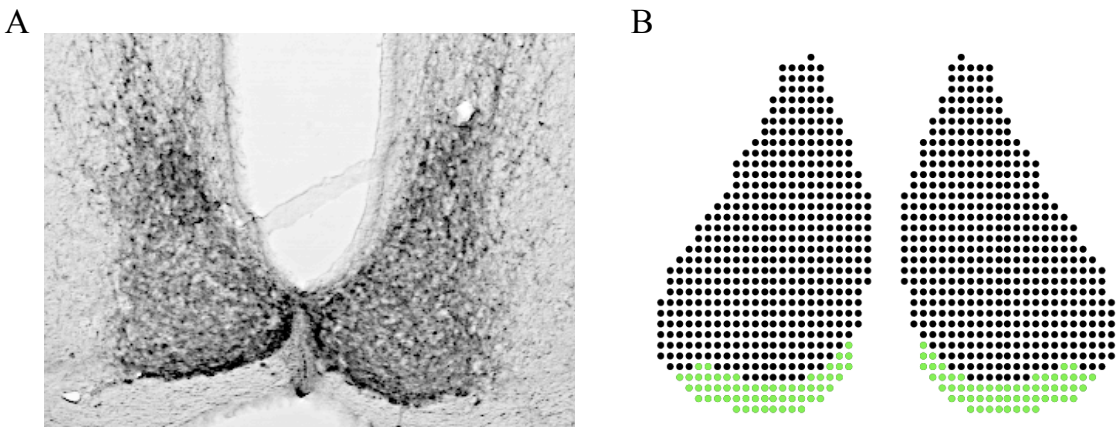

Figure 3.2: VIP producing cells determined by immunohistochemistry. (A) Immunostaining of an SCN slice pretreated with colchicine to block VIP transport to neurites identifies cell bodies of VIP-producing cells. (B) Based on the experimental data, roughly 10% of SCN neurons, located in the ventral-medial SCN are assumed to produce and release VIP in the model (green cells). VIP is assumed to diffuse quickly across the SCN so that all cells may receive it.

M times. This technique greatly speeds up the computation. A summary of the procedure for solving the model is given in algorithm 1.

Algorithm 1 Solve the SCN model

for $MCStep = 1, \ldots, M$ **do**
  calculate g_{K-leak} and g_{KCa} (functions of molecular clock model variable G)
  for $EphysStep = 1, \ldots, N$ **do**
    calculate GABA input to each cell (cuBLAS matrix vector multiply: $[T_{in}] = C[T_{out}]$)
    execute GPU kernel to update electrophysiology variables:
      $t_{inner} \leftarrow t_{inner} + \frac{\Delta t_E}{2}$
      update gating variables ($m, h, n, r_L, r_{NL}, f_{NL}, s, y$) and calcium ($Ca_s, Ca_c$)
      $t_{inner} \leftarrow t_{inner} + \frac{\Delta t_E}{2}$
      update voltage (V)
      calculate GABA output from each cell ($[T]_i = f(V_i)$)
  end for
  calculate VIP released to all cells (find mean of Ca_c in VIP-producing cells)
  $t_{outer} \leftarrow t_{outer} + \Delta t_M$
  execute GPU kernel to update molecular clock variables
end for

The specific details of the numerical methods used to solve the two different models are given in the next two sections. We find that using a molecular clock time step (Δt_M) of 0.004 hours, an electrophysiology model time step (Δt_E) of 0.1 ms, and simulating the electrophysiology model for 1 second in between each molecular clock step ($N =$

$10,000$) allows us to simulate the model in a reasonable amount of time and with sufficient accuracy. We test this accuracy by simultaneously halving Δt_M and Δt_E and comparing the numerical solution of the total PER2 protein levels in one cell at the end of 24 hours of simulated time. We calculate the percent error of the numerically estimated PER2 levels with the less refined time step relative to the more refined one as:

$$\text{Percent error} = \frac{PER2(\Delta t_M, \Delta t_E) - PER2(0.5\Delta t_M, 0.5\Delta t_E)}{\frac{PER2(\Delta t_M, \Delta t_E) + PER2(0.5\Delta t_M, 0.5\Delta t_E)}{2}} \times 100$$

Reducing Δt_M from 0.004 hrs to 0.002 hrs and Δt_E from 0.1 ms to 0.05 ms yields a percent error of 0.0119%. Reducing Δt_M from 0.002 hrs to 0.001 hrs and Δt_E from 0.05 ms to 0.025 ms yields a percent error of 0.0055%. The small error implies that very little is gained in accuracy by decreasing the time steps, so we perform all simulations with $\Delta t_M = 0.004$ and $\Delta t_E = 0.1$.

All simulations presented in this chapter were done on either NVIDIA Tesla M2090 or K20m GPU cards, with all code written in CUDA and C++. Since all network simulations contained 1024 cells and these cards have 512 and 2496 cores respectively, the molecular clock and electrophysiology update kernels were organized so that each thread calculated the updated state variables for one cell on the K20m or two cells on the M2090. The GABA input to all cells was calculated simultaneously as a large matrix vector multiplication on the GPU using the cuBLAS library (as explained in section 3.3.3). All calculations were performed on the GPU as noted in algorithm 1. Arrays for all state variables and their updates in time, as well as for all parameters, were initialized on the GPU. All data fit easily within the 5 GB on board memory of the GPU card (requiring only 100-200 MB of memory for most simulations). State variables were saved into separate output arrays allocated on the GPU card at regular intervals and copied back to the CPU for writing to files so as to avoid data races, reduce the memory needed on the GPU at any one time,

and improve performance. Simulations took roughly 24 hours of walltime for 12 days of simulated time.

3.3.2 Integrating the molecular clock model

The standard 4th order Runge-Kutte method is used to numerically solve the molecular clock model, with a time step of 0.004 hours, as discussed above. At a fixed point in time, the only input from the electrophysiology model into the molecular clock model is each cell's intracellular calcium concentration. This is assumed to vary little over the time step of the molecular clock. To test this assumption, we compare the maximum and minimum calcium values attained by a cell at different molecular clock phases. As the parameter R, which measures molecular clock phase (see section 3.2.1), is varied, large differences in calcium concentration are seen across different clock phases, however, little difference is seen between the maximum and minimum intracellular calcium values attained at a single point in time so that these curves are almost indiscernible. The maximum and minimum intracellular calcium values as well as the difference between these values are plotted in Figure 3.3.

3.3.3 Integrating the electrophysiology model

Trapezoidal rule with leapfrogging

Because of its stiffness, we use an implicit second order method, based on the trapezoidal rule, to solve the electrophysiology ODE model. The method employs a leapfrogging scheme in which the voltage is solved for on whole time steps $(t = 0, 1\Delta t, 2\Delta t,)$, and taken to be constant until the next whole time step, and the gating variables and calcium are solved on half time steps $(t = .5\Delta t, 1.5\Delta t, 2.5\Delta t,)$, and likewise assumed to be constant at intermediate times. This method works well for Hodgkin-Huxley style equations as the ODEs for each of the voltage and gating variables are linear in themselves

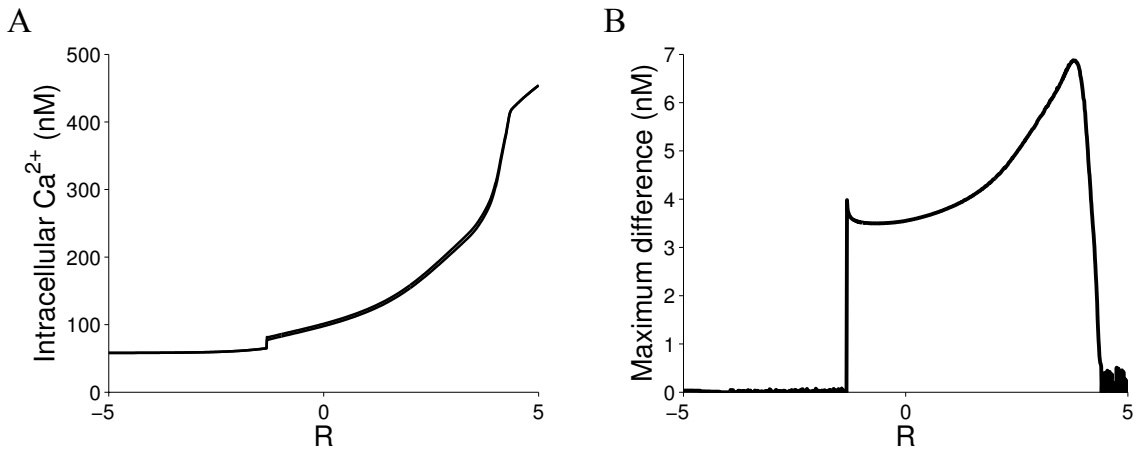

Figure 3.3: (A) Maximum and minimum intracellular calcium concentrations (Ca_c) attained at different molecular clock phases. The molecular clock state is determined by the parameter R, which depends on E-box activity and varies between -5 and 5 depending on the phase of the cell's rhythms. (B) The difference between the two curves in panel A. The maximum difference between the calcium peaks and troughs at any point in time is very small ($\leq$ 7 nM) relative to the circadian variation in calcium ($\sim$400 nM).

so that the implicit method can actually be solved explicitly. For example, for a gating variable q, generally q_∞ and τ_q depend on V which varies in time, but holding V fixed, these become constants, allowing us to integrate directly:

$$\int_{t-\frac{\Delta t}{2}}^{t+\frac{\Delta t}{2}} \frac{dq}{dt} dt = \int_{t-\frac{\Delta t}{2}}^{t+\frac{\Delta t}{2}} \frac{q_\infty - q(t)}{\tau_q} dt$$

$$q\left(t+\frac{\Delta t}{2}\right) - q\left(t-\frac{\Delta t}{2}\right) = \frac{q_\infty}{\tau_q}\Delta t - \frac{1}{\tau_q}\int_{t-\frac{\Delta t}{2}}^{t+\frac{\Delta t}{2}} q(t)dt.$$

Using the trapezoid rule to approximate the integral of $q(t)$ gives

$$q\left(t+\frac{\Delta t}{2}\right) - q\left(t-\frac{\Delta t}{2}\right) = \frac{q_\infty}{\tau_q}\Delta t - \frac{\Delta t}{2\tau_q}\left(q\left(t+\frac{\Delta t}{2}\right) + q\left(t-\frac{\Delta t}{2}\right)\right).$$

Solving for $q(t+\frac{\Delta t}{2})$ (denoted as $q_{t+\frac{\Delta t}{2}}$) gives the simple update scheme

$$q_{t+\frac{\Delta t}{2}} = \frac{2\Delta t}{2\tau_q(V_t)+\Delta t} q_\infty(V_t) + \frac{2\tau_q(V_t)-\Delta t}{2\tau_q(V_t)+\Delta t} q_{t-\frac{\Delta t}{2}}$$

where V_t is the voltage at time t and $q_{t-\frac{\Delta t}{2}}$ is the value of the gating variable at the previous time step.

On the half time step

The equations for $q = m,\ h,\ n,\ r_L,\ r_{NL}$, and f_{NL} follow the pattern above identically. We update these gating variables on the half step ($t + \frac{\Delta t}{2}$) first.

The update equations for Ca_s, Ca_c, and s can also be solved explicitly on the half time step when voltage is held fixed in the same manner. Note that since $f_L = \frac{K_1}{K_2 + Ca_s}$, the equation for Ca_s becomes quadratic, but may be solved explicitly using the quadratic formula. Due to the complexity of these expressions and for ease of notation, we will drop all subscripts and capitalization in variable names when writing out the update equations (e.g. $r_L = rl$, Ca_s = cas, etc.).

$$cas_{t+\frac{\Delta t}{2}} = \frac{-B + \sqrt{B^2 - 4AC}}{2A}$$

where:

$$A = \frac{1}{\Delta t} + \frac{1}{2\tau_s}$$

$$B = \frac{K_2 - cas_{t-\frac{\Delta t}{2}}}{\Delta t} + \frac{k_s}{2} g_{CaNL} rnl_{t+\frac{\Delta t}{2}} fnl_{t+\frac{\Delta t}{2}} (V_t - E_{Ca}) + \frac{K_2 + cas_{t-\frac{\Delta t}{2}}}{2\tau_s} - b_s$$
$$+ \frac{k_s}{2} \left(g_{CaL} rl_{t-\frac{\Delta t}{2}} \frac{K_1}{K_2 + cas_{t-\frac{\Delta t}{2}}} + g_{CaNL} rnl_{t-\frac{\Delta t}{2}} fnl_{t-\frac{\Delta t}{2}} \right) (V_t - E_{Ca})$$

$$C = -\frac{K_2}{\Delta t} cas_{t-\frac{\Delta t}{2}} + \frac{K_2}{2\tau_s} cas_{t-\frac{\Delta t}{2}} - b_s K_2$$
$$+ \frac{k_s}{2} \Big(g_{CaL} rl_{t+\frac{\Delta t}{2}} K_1 + K_2 g_{CaNL} rnl_{t+\frac{\Delta t}{2}} fnl_{t+\frac{\Delta t}{2}} \Big) (V_t - E_{Ca})$$
$$+ \frac{k_s K_2}{2} \Big(g_{CaL} rl_{t-\frac{\Delta t}{2}} \frac{K_1}{K_2 + cas_{t-\frac{\Delta t}{2}}} + g_{CaNL} rnl_{t-\frac{\Delta t}{2}} fnl_{t-\frac{\Delta t}{2}} \Big) (V_t - E_{Ca})$$

$$cac_{t+\frac{\Delta t}{2}} = \frac{1}{1 + \frac{\Delta t}{2\tau_c}} \Big[cac_{t-\frac{\Delta t}{2}} (1 - \frac{\Delta t}{2\tau_c}) + b_c \Delta t - \frac{k_c}{2} \Delta t \Big(g_{CaL} rl_{t+\frac{\Delta t}{2}} \frac{K_1}{K_2 + cas_{t+\frac{\Delta t}{2}}}$$
$$+ g_{CaNL} rnl_{t+\frac{\Delta t}{2}} fnl_{t+\frac{\Delta t}{2}} + g_{CaL} rl_{t-\frac{\Delta t}{2}} \frac{K_1}{K_2 + cas_{t-\frac{\Delta t}{2}}}$$
$$+ g_{CaNL} rnl_{t-\frac{\Delta t}{2}} fnl_{t-\frac{\Delta t}{2}} \Big) (V_t - E_{Ca}) \Big]$$

$$s_{t+\frac{\Delta t}{2}} = \frac{1}{1 + \frac{\Delta t}{2\tau_s(cas_{t+\frac{\Delta t}{2}})}} \Big(s_{t-\frac{\Delta t}{2}} \Big(1 - \frac{\Delta t}{2\tau_s(cas_{t-\frac{\Delta t}{2}})} \Big)$$
$$+ \frac{\Delta t}{2} \Big(\frac{s_\infty(cas_{t-\frac{\Delta t}{2}})}{\tau_s(cas_{t-\frac{\Delta t}{2}})} + \frac{s_\infty(cas_{t+\frac{\Delta t}{2}})}{\tau_s(cas_{t+\frac{\Delta t}{2}})} \Big) \Big)$$

Note that these require the values of the gating variables rl, rnl, and fnl at time $t + \frac{\Delta t}{2}$, so the gating variable updates must be calculated first. Additionally, the updates for $cac_{t+\frac{\Delta t}{2}}$ and $s_{t+\frac{\Delta t}{2}}$ updates require the value of $cas_{t+\frac{\Delta t}{2}}$, so cas must be updated before these can be calculated. If the equations are solved in the order listed above, they can all be determined explicitly.

The GABA gating variable y is also calculated on the half time step:

$$y_{t+\frac{\Delta t}{2}} = \frac{(2\Delta t)a_r[T_{in}]_t + (2 - (a_r[T_{in}]_t + a_d)\Delta t)y_{t-\frac{\Delta t}{2}}}{2 + (a_r[T_{in}]_t + a_d)\Delta t}$$

where $[T_{in}]_t$ is the amount of neurotransmitter GABA input to the cell at time t (dependent on the voltages of all upstream cells as explained in section 3.2.2).

On the whole time step

Voltage is next updated on the whole time step ($t + \Delta t$):

$$V_{t+\Delta t} = \frac{1}{C_M + \frac{\Delta t}{2}G}\Big(E\Delta t + (C_M - \frac{\Delta t}{2}G)V_t\Big)$$

where:

$$G = g_{Na}m^3_{t+\frac{\Delta t}{2}}h_{t+\frac{\Delta t}{2}} + g_K n^4_{t+\frac{\Delta t}{2}} + g_{CaL}rl_{t+\frac{\Delta t}{2}}\frac{K_1}{K_2 + cas_{t+\frac{\Delta t}{2}}}$$
$$+ g_{CaNL}rnl_{t+\frac{\Delta t}{2}}fnl_{t+\frac{\Delta t}{2}} + g_{KCa}s^2_{t+\frac{\Delta t}{2}} + g_{K-leak} + g_{Na-leak} + g_{GABA}y_{t+\frac{\Delta t}{2}}$$

and

$$E = E_{Na}(g_{Na}m^3_{t+\frac{\Delta t}{2}}h_{t+\frac{\Delta t}{2}} + g_{Na-leak}) + E_K(g_K n^4_{t+\frac{\Delta t}{2}} + g_{KCa}s^2_{t+\frac{\Delta t}{2}} + g_{K-leak})$$
$$+ E_{Ca}(g_{CaL}rl_{t+\frac{\Delta t}{2}}\frac{K_1}{K_2 + cas_{t+\frac{\Delta t}{2}}} + g_{CaNL}rnl_{t+\frac{\Delta t}{2}}fnl_{t+\frac{\Delta t}{2}})$$
$$+ E_{GABA}g_{GABA}y_{t+\frac{\Delta t}{2}}.$$

For ease of computation, we add an extra state variable $[T_{out}]_j$ for each cell j, which records the amount of GABA that the cell releases to downstream cells, as described in section 3.2.2. $[T_{out}]_j$ is an instantaneous function of the cell's voltage V_j, so we update it now to its value at time $t + \Delta t$ so that it may be used in the next update of the gating variables y for all downstream cells (from time $t + \frac{\Delta t}{2}$ to time $t + \frac{3\Delta t}{2}$). For a downstream cell, the total synaptic input from all upstream cells can be easily calculated as the i-th element of the vector $[T_{in}]$, with $[T_{in}] = C[T_{out}]$ where C is the synaptic connectivity matrix: $C(i, j)$ = 1 if cell j has a projection to cell i and zero otherwise. This simplifies

the calculation of the GABA input to all cells to a simple matrix vector multiplication which we calculate using the cuBLAS package as described in section 2.2.3.

Method validation

We validate this numerical method by comparing its accuracy to the numerical solution calculated by MATLAB's ode15s ODE solver with low tolerance settings (relative and absolute tolerances = 1e-12, and max step size = 0.1 ms), and by performing a time step refinement study. Voltage traces for 1 second of simulated time with ode15s and our numerical method with various time steps are shown in Figure 3.4A. Trajectories are almost indistinguishable with time steps ranging between 0.0125 ms to 0.4 ms. A magnification of the last action potential in Figure 3.4B reveals differences between the larger time step simulations ($\Delta t_E \geq 0.2$ ms) and the rest. All simulations in the main text use a time step of 0.1 ms for the electrophysiology model, which matches the ode15s solution extremely well. To quantify this, we plot the log_2 of the error in the final voltage at the end of each simulation using our method relative to the ode15s solution versus the log_2 of the step size, dt (Figure 3.4C). Linear regression of the error values shows that the method is second order, as expected based on the error in the trapezoidal rule (slope = 2.0084, r^2 = 0.99931). With a time step of 0.1 ms, the percent error in the final value relative to the ode15s solution is:

$$\frac{|V_{LF}(t_{final}) - V_{ode15s}(t_{final})|}{V_{ode15s}(t_{final})} = 0.0631\%$$

where V_{LF} is the voltage calculated using the leapfrogging method and V_{ode15s} is the voltage calculated using Matlab's ode15s solver.

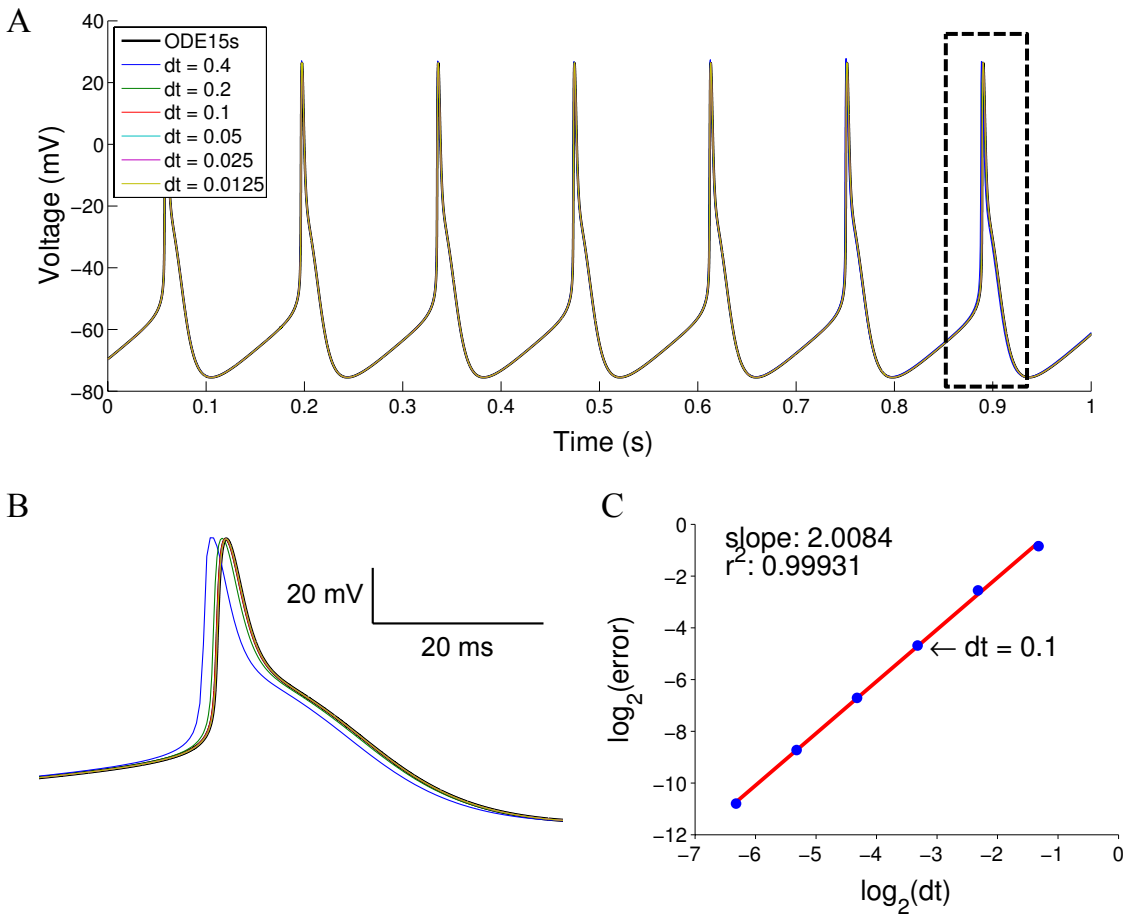

Figure 3.4: Comparison of numerical solutions found using the trapezoidal rule with leapfrogging with various time steps and MATLAB's ode15s. (A) Voltage traces for one cell simulated for one second with time steps between 0.0125 ms and 0.4 ms are nearly indistinguishable. (B) A very close magnification of the final action potential in panel A (denoted by the dashed box) reveals small differences between the simulations. Simulations with time steps greater than 0.1 ms differ from those with smaller time steps, which closely match the ode15s solution. A scale bar is shown in the upper right corner. (C) Quantification of time step refinement study shows that the method attains second-order accuracy for values of dt near that used in full model simulations (dt = 0.1 ms). Error is defined as $|V_{LF}(t_{final}) - V_{ode15s}(t_{final})|$ where V_{LF} is the voltage calculated using the leapfrogging method and V_{ode15s} is the voltage calculated using Matlab's ode15s solver (relative and absolute tolerances = 1e-12, max step size = 0.1 ms). Voltages were compared at the end of the 1 second simulation from panel (A).

3.4 Experimental methods

3.4.1 Hyperpolarizing current phase response measurements

In this section, we measure the response of SCN neurons to GABA-like current pulses and generate a phase response curve. Electrophysiological recordings were done as in [14]

by Mino Belle in the lab of Hugh Piggins. Ten pA hyperpolarizing current pulses, 60ms in duration were applied to SCN neurons in acute mouse brain slices. The GABAA receptor antagonist gabazine [64] was used to block the effects of endogenous synaptic input. I analyzed the data and generated the experimental PRC. Only neurons that repetitively fired both before and after the pulse were used. A cells characteristic ISI was measured as the mean of the lengths of the four ISIs prior to each pulse. Change in phase was determined as the difference in timing of the third subsequent spike after the pulse and the predicted time of this spike if no pulse had been given (three standard ISIs after the spike preceding the pulse).

3.4.2 MQAE imaging of intracellular free chloride concentration

The GABA-response polarity of an SCN neuron depends on its intracellular chloride concentration, which determines the cell's GABA reversal potential, E_{GABA}. To measure intracellular chloride, we apply a fluorescent dye, MQAE (N-(Ethoxycarbonylmethyl)-6-methoxyquinolinium bromide), that is quenched by chloride to SCN slices and measure fluorescence. MQAE experiments and imaging were done by myself and Jihwan Myung in the lab of Toru Takumi. Calibration of the fluorescence measurement with chloride standards is shown in Figure 3.5. Full methods are given in [30]. To verify that the chloride concentration did not vary with time, time-lapse MQAE fluorescence images from the SCN were obtained with a confocal microscope under sequential 405 nm and 488 nm excitations, shown in Figure 3.6. Timelapse imaging was done in 30-minute intervals, and the nuclear signal from the green emission (from the 488 nm excitation) was used to identify regions-of-interest where chloride was then estimated from the blue emission (405 nm excitation).

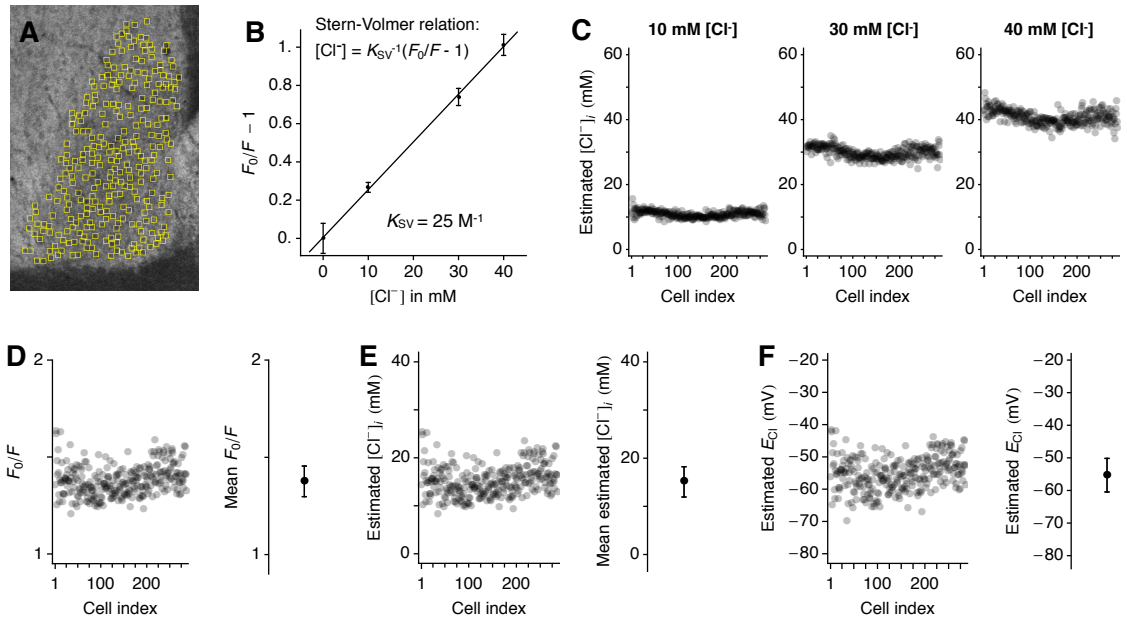

Figure 3.5: Calibration and estimation of the intracellular chloride concentration in the SCN in situ. (A) Cellular regions-of-interest (ROI) in an SCN slice selected for chloride calibration and estimation (n=286 cells). (B) The Stern-Volmer constant (KSV) is estimated to be 40 M^{-1} using chloride standards of 0, 10, 30, and 40 mM (R^2 = 0.999). Error bars indicate standard deviation. (C) Estimated chloride concentrations in the cells of the SCN slice in each standard solution. The standard solution contains ionophores to enable diffusion of the bath chloride into the cells. (D) The ratio of MQAE fluorescence values under 0 mM chloride, F0, and control, F, in the 286 randomly selected cells. (E) The Stern-Volmer relation-based estimation predicts a range of 10-30 mM intracellular chloride concentrations. (F) By the Nernst equation under room temperature (25°C), the range of chloride reversal potentials is estimated to be -70 to -40 mV.

3.4.3 Identification of VIP producing cells

To determine which SCN cells produce VIP, VIP immunostaining was performed on SCN slices from animals pretreated with colchicine injection to block VIP transport to neurites. Immunostaining experiments were performed by Jihwan Myung in the lab of Toru Takumi. Animals were fixed trough cardiac perfusion after pentobarbital anesthesia. Cryosections of the SCN were prepared and immunohistochemistry against VIP was performed as in [91]. VIP rabbit polyclonal antibody (ImmunoStar) was used at 1:1000 dilution. Results of the immunostaining are shown in Figure 3.2A.

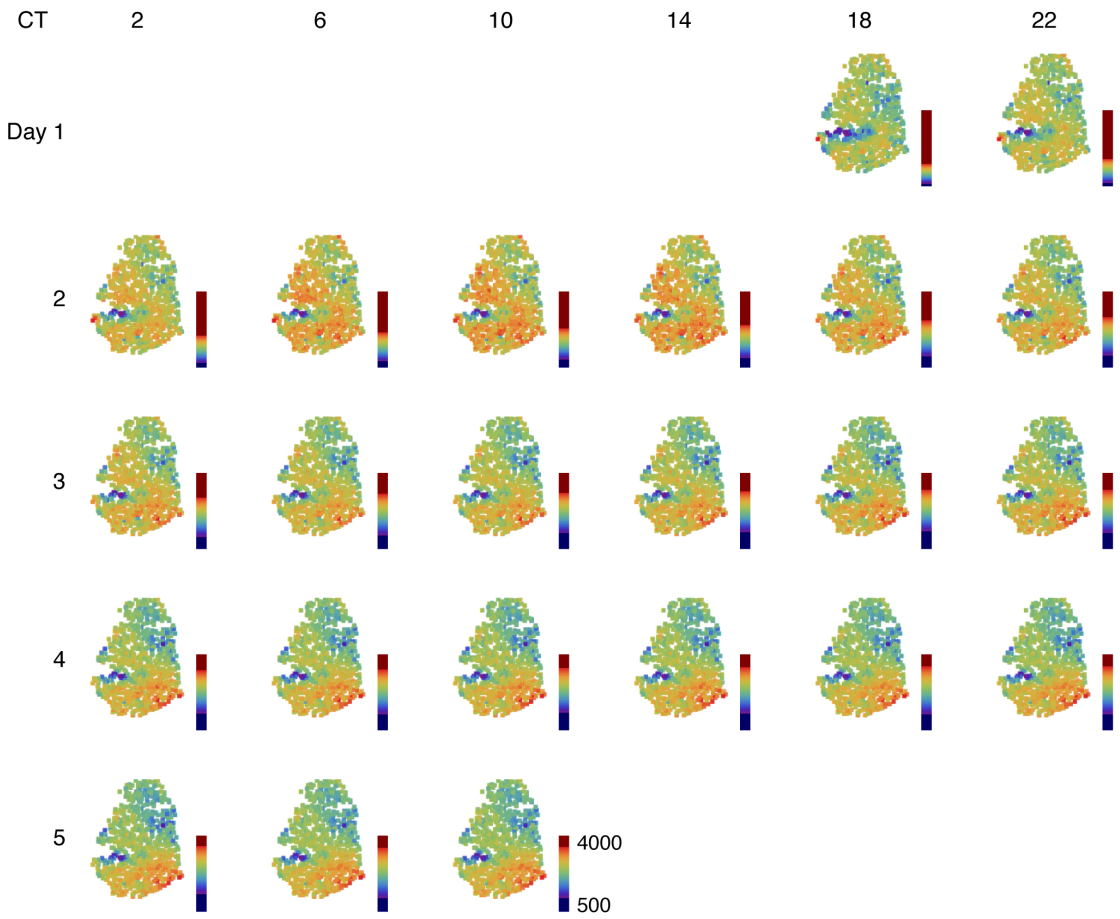

Figure 3.6: Timelapse MQAE measurement of intracellular chloride. Images are shown in 4-hour intervals for the left lobe of an SCN slice. Small differences in fluorescence amplitudes are seen over the first day, but the spatial distribution of relative fluorescence levels is consistent over the entire recording. Fluorescence is lower in the dorsal SCN, signifying the presence of more chloride relative to the ventral region.

3.5 Results

3.5.1 Effect of GABA signaling on SCN neuron electrical activity

We first use the model to predict the response of individual SCN neurons to GABA induced PSCs. Our model makes an interesting prediction that goes against the prevailing thinking about the SCN [64, 118]. While we predict that inhibitory PSCs will lengthen the interspike interval (ISI) and slow down firing when presented at later phases during the ISI, we also find that PSCs given earlier in the ISI can shorten the ISI and speed up

firing. While the magnitude of this effect depends on the time of day, the trend is consistent throughout the daytime.

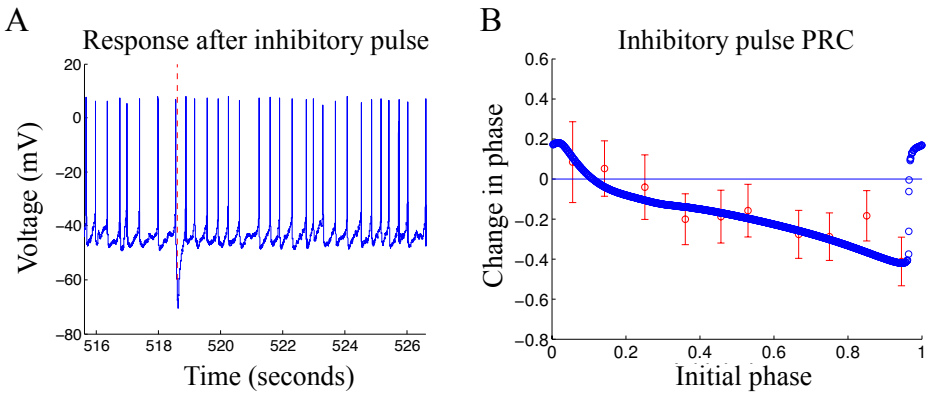

Figure 3.7: Effects of inhibitory pulses on SCN neuron firing activity. (A) Sample firing activity of an SCN neuron before and after the administration of a hyperpolarizing pulse (time of pulse denoted by red dashed line). (B) The model predicted phase response curve (dark blue line) is plotted along with the mean and standard error of responses to inhibitory pulses given experimentally to SCN neurons (red), binned by phase of pulse initiation (for the electrophysiology model, parameter R=2). Both the model-predicted and experimentally determined responses show that the response to the pulse depends on when in the ISI it is given, with pulses given shortly after the firing of an action potential shortening the ISI (as in panel A) while pulses given late in the ISI lengthening it.

To test this prediction, we apply 10pA hyperpolarizing (inhibitory) current pulses, 60ms in duration (simulating approximately 10 PSCs, a typical number seen during an ISI, presented simultaneously), to SCN neurons and measure the change in ISI caused by the pulses as described in the methods section. Data for a sample neuron is shown in Figure 3.7A. All data are grouped into 10 bins and plotted on top of the model predicted PRC in Figure 3.7B. Our simulated PRC generated before the experiment, matches the data surprisingly well. In particular, we see that inhibitory pulses given shortly after an action potential shorten the length of the ISI, while pulses given later in the cycle tend to increase the length of the ISI, validating our hypothesis.

3.5.2 Experimental measurement of the spatial distribution of excited and inhibited cells

The type of response of a cell to GABA is dependent on the chloride equilibrium potential of the cell (E_{GABA}), which is a function of the cells intracellular chloride concentration. To estimate the relative GABA equilibrium potentials of cells in the SCN, we measure relative intracellular chloride levels by applying MQAE (N-(Ethoxycarbonylmethyl)-6-Methoxyquinolinium Bromide) to acute SCN slices and measuring fluorescence with a confocal microscope (Figure 3.8A). MQAE is quenched by chloride, so the intracellular chloride concentration is assumed to be inversely proportional to the amount of fluorescence measured. A calibration of chloride quantification using MQAE can be found in Figure 3.5. Fluorescence is averaged over cell-sized regions (Figure 3.8B) and used to estimate relative E_{GABA} values across our model SCN (Figure 3.8C), which we scale to lie in a range between -32mV and -80mV, corresponding to chloride intracellular concentrations of roughly 47 mM and 7 mM, respectively, as has been previously reported [3, 132]. Our own estimation of the intracellular chloride concentration and corresponding chloride reversal potential from 286 randomly selected cells from an SCN slice (Figure 3.5) finds chloride reversal potentials consistent with this range and distribution (between -70 and -40 mV). We find that our estimated E_{GABA} values are roughly normally distributed (Figure 3.8D) across the SCN, but that there is a spatial bias with more cells with higher E_{GABA} in the dorsal SCN than in the ventral. The spatial distribution of relative chloride levels does not change over time (Figure 3.6). These findings suggest that subsets of cells are excited or inhibited throughout the entire circadian day, and the rest may change polarity as their resting membrane potential rises and falls above E_{GABA}.

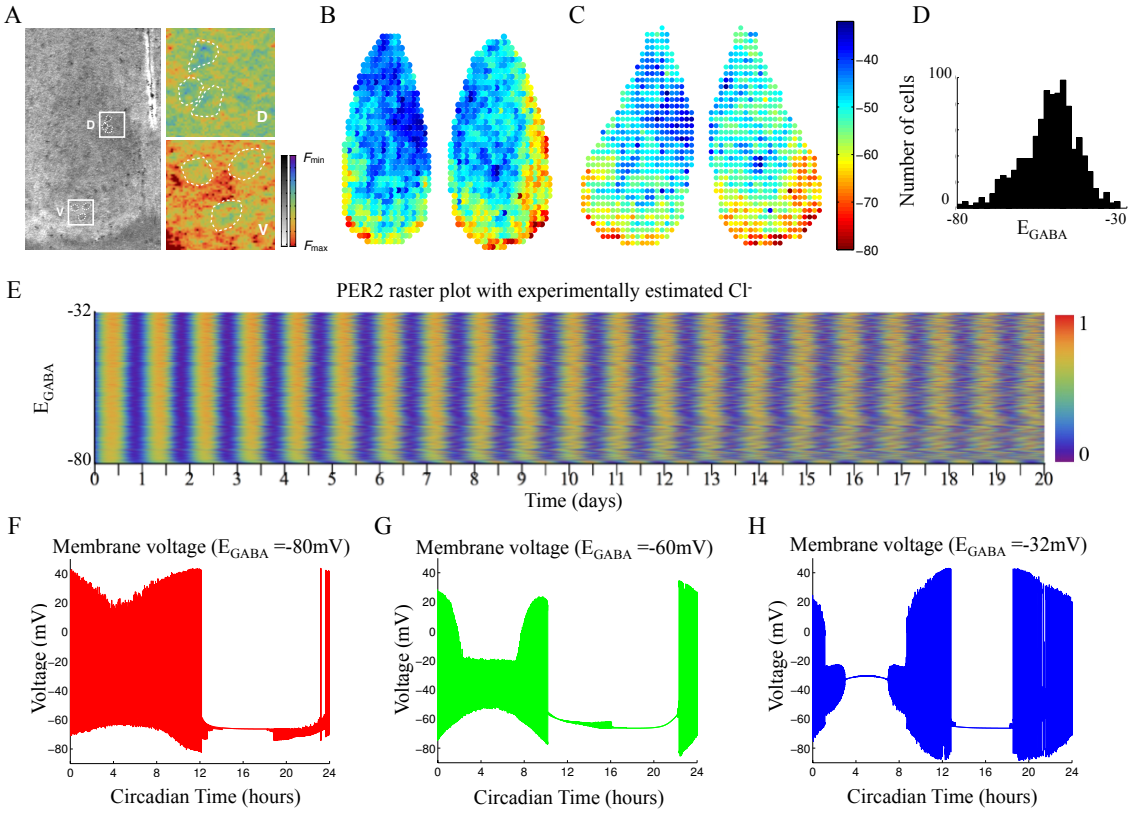

Figure 3.8: Experimentally measured intracellular chloride is used to determine EGABA for simulations, leading to predictions of strong effects of GABA signaling on cellular electrical activity rhythms. (A) Confocal microscopy of MQAE fluorescence in a unilateral SCN from an acute slice. MQAE is quenched by chloride, so areas with high fluorescence represent low intracellular chloride. Magnified images of cell bodies in dorsal, D, cells show lower fluorescence than those in ventral, V, cells. (B) Fluorescence values from the whole SCN slice are averaged over cell-sized regions, and (C) used to estimate the relative distribution of EGABA. Cells with high EGABA are excited by GABA, and with low EGABA are inhibited by it. Note that cells are plotted on a grid for visualization purposes only and that connectivity is determined independently of distance between cells, as described in the text. (D) Estimated EGABA levels across the SCN are found to be roughly normally distributed but with a clear spatial bias between the dorsal and ventral SCN. (E) A raster plot of simulated PER2 rhythms over 20 days for an SCN with the experimentally estimated EGABA values from panel C (cells are sorted by EGABA). (F-H) Circadian variation in electrical activity for sample cells with EGABA values of -80 mV (F), -60 mV (G), and -32 mV (H), plotted as the range of voltages attained by the cells throughout the day. Circadian time is determined relative to the peak in whole SCN PER2 protein levels, which is defined to be CT12.

3.5.3 Predicted consequences of spatial heterogeneity in GABA signaling

Using the distribution of E_{GABA} from Figure 3.8C, we simulate a network of 1024 SCN neurons coupled through GABA alone. All molecular clock parameters are taken

from [29] and additional electrophysiological parameters are from [31]. Heterogeneity is included in all parameters by drawing them from normal distributions with means equal to the fit values and standard deviations 2% of the means, representing unbiased heterogeneity between cells. Surprisingly, we find that GABA signaling seems to maintain some synchrony in the SCN, particularly within the GABA-excited subpopulation. Cells in the network that are strongly excited by GABA are better synchronized, and have higher amplitude rhythms (Figure 3.8E). Summaries of the circadian electrical activities over a single day for three sample cells are shown in Figures 3.8F-H, represented as the range of voltages attained by each cell continuously throughout the day. These cells have E_{GABA} values such that they are always inhibited by GABA (-80 mV), inhibited at some times of day and excited at others (-60 mV), and always excited by GABA (-32 mV) respectively. These three cells represent the continuum of electrical activities seen in the model, with the trend that excitation by GABA can drive neurons to higher resting membrane voltages and consequently hyperexcitation, including the depolarized low-amplitude membrane oscillation (DLAMO) and depolarized states that were described in [14]. The model predicts that this causes higher amplitude rhythms in intracellular calcium, as shown in Figure 3.9, which can increase transcription and cause the higher amplitude molecular rhythms previously noted. This also leads to the hypothesis that GABA signaling could affect the synchrony of molecular rhythms by driving resting membrane voltage and consequently intracellular calcium rhythms.

The model predicts that because GABA signaling changes the firing activities of individual cells, it will also impact GABA release. To explore this, we compare the profile of GABA release across one day for the three cells shown in Figure 3.8F-H (plotted in Figure 3.10A-C). Cells release large bursts of GABA after each action potential. This type of GABA release is termed phasic, and leads to the PSCs commonly described ex-

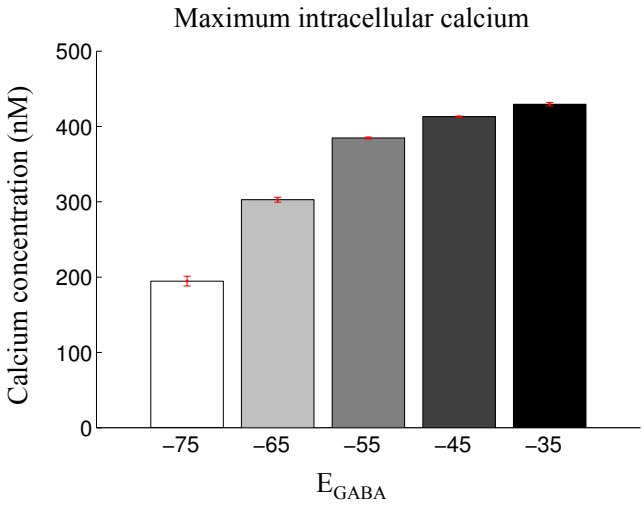

Figure 3.9: The magnitude of calcium oscillations is predicted to increase with E_{GABA}. Mean and standard error (red bars) of maximal calcium concentration attained in a circadian cycle are plotted for cells from the simulation in Figure 3.8. Cells are binned by E_{GABA} in 10 mV bins centered at the denoted E_{GABA} levels.

perimentally. During depolarization block, on the other hand, a very low level of GABA is predicted to be released at a roughly constant rate, lasting for some cells up to four or five hours (Figure 3.10C). The magnitude of this release is less than 5% of the amplitude of GABA released after an action potential, but it is sustained over time. This type of sustained GABA release is similar to the tonic GABA release that has been seen experimentally in a variety of neuronal systems [70, 40] but not fully explored in SCN neurons.

3.5.4 Tonic but not phasic GABA signaling effectively shifts molecular rhythms

To compare the effects of tonic and phasic GABA signaling on SCN neurons, we applied specific GABA time courses to simulated cells with GABA equilibrium potentials ranging between -80 and -32 mV. The first GABA stimulus used was a regular 10Hz phasic GABA signal five hours in duration, applied every 24 hours. This mimics the signal a cell could receive from multiple upstream cells collectively firing 10 total action potentials per second between them, for five hours each day. This signal caused no shift in the molecular

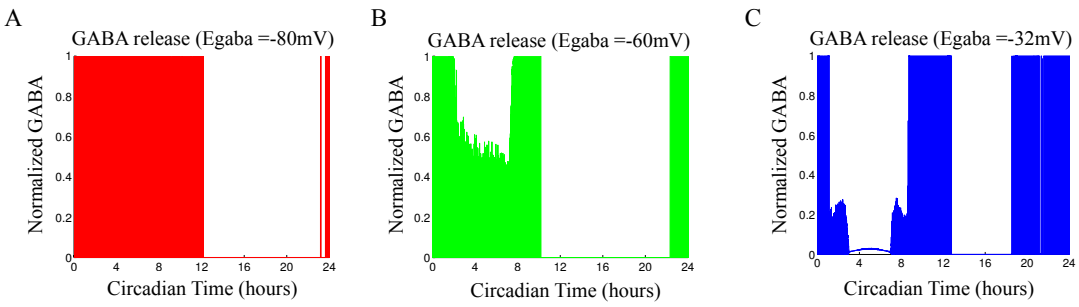

Figure 3.10: Differential patterns of GABA release by cells in different firing states. (A-C) The range of GABA released throughout one day by the sample cells in Figure 3.8 F-H with E_{GABA} values of -80, -60, and -32 mV respectively. All GABA values are normalized to the amount of GABA released after an action potential. Cells firing action potentials release short, large bursts of GABA, whereas cells in depolarization block release tonic, low levels of GABA as can be seen between CT 3 and 7 in panel C. Cells in the DLAMO state release intermediate spikes of GABA as they oscillate (as in panel B ~CT 2-7).

rhythm of the downstream cell regardless of its E_{GABA} (Figure 3.11A), and regardless of when the window fell within the circadian day. The cells did not entrain to the signal. The second GABA stimulus applied was a five-hour window of tonic, low-amplitude GABA, given every 24 hours, mimicking the GABA released by upstream cells entering depolarization block in the afternoon. Although a similar level of GABA was released with both signals, the tonic signal caused significant shifts in the molecular rhythms of the downstream cells, and the direction of the shift depended on the cells E_{GABA} (Figure 3.11B). Cells were entrained by this signal with a fixed phase relationship dependent on E_{GABA}.

To characterize this entrainment, we measure the response of individual SCN neurons in the network to this five-hour sustained GABA timecourse by calculating the PRC of sample cells with the most excitatory (E_{GABA} = -32 mV) or most inhibitory (E_{GABA} = -80 mV) responses to this signal. The PRC, shown in Figure 3.11C, shows a stable steady state for the excited cells with the pulse beginning at around CT3. This matches exactly the time (CT3-8) when the tonic GABA is predicted to be released, when the excited cells enter the depolarized states (as in Figure 3.8H), and also matches the phase of entrainment

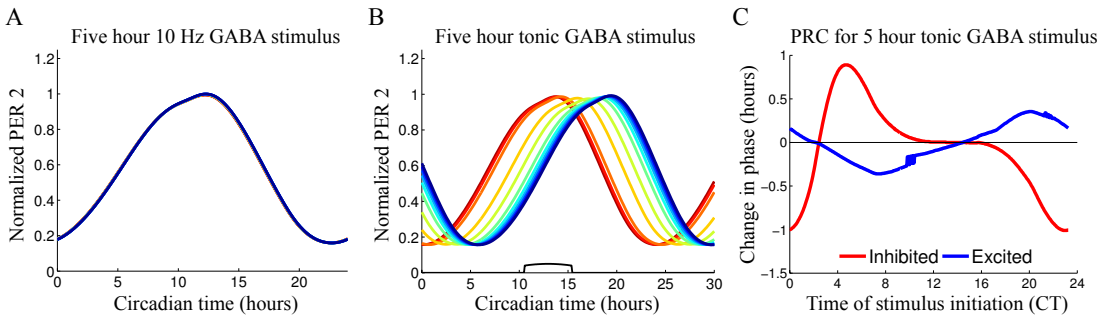

Figure 3.11: Tonic but not phasic GABA causes shifts in PER2 rhythms, with different phasing depending on the cells GABA equilibrium potential. Cells with EGABA ranging from -80 (red) to -32 (blue) are stimulated with 5 hours of phasic GABA at 10 Hz (A) or low level tonic GABA (B); GABA equilibrium potentials denoted by colors as in Figure 3.8C. PER2 rhythms for cells in panel A overlap, showing that five hours of phasic GABA does not shift the molecular rhythms of any of the cells, and they do not entrain to it regardless of when in the cycle it is given. Cells do shift to entrain to the tonic GABA stimulus with the phase relationships shown in panel B. The timing and relative amplitude of the GABA stimulus are denoted by the black curve. (C) A phase response curve of strongly inhibited (EGABA = -80) and excited (EGABA = -32) cells in response to the 5-hour tonic GABA stimulus. Initial phase is defined as the time of the beginning of the stimulus and for each cell, circadian time is determined relative to the peak in the cells PER2 protein levels, which is defined to be CT12.

shown in Figure 3.11B for the most excited cells. Conversely, cells inhibited by GABA have an unstable steady state at this time, flanked by regions of greatest advance and delay. If the sustained GABA pulse begins around this time, but not exactly at the steady state, cells will be pushed towards either big advances or delays, depending on their initial phase. The PRC predicts that the excited cells will stay synchronized, while the inhibited cells will split with some advancing and some delaying. Furthermore, it predicts that if this sustained signal persisted and was strong enough, the inhibited cells could synchronize as a secondary population antiphase to the GABA-excited cells.

3.5.5 GABA synchronizes molecular rhythms in excited cells

We find that the distribution and percentage of cells within the network with fixed GABA polarities seem to have the most significant effects on synchrony of molecular rhythms. The cells that are always excited by GABA release tonic GABA when they become depolarized, and force cells that are strongly inhibited by GABA to shift antiphase

to the tonic GABA signal. To further explore this in silico, we test idealized networks in which we consider only subpopulations of cells that are excited or inhibited at all times of day. For these populations, we fix the excited and inhibited GABA equilibrium potentials to -32mV and -80 mV respectively and vary the proportions of GABA-excited and GABA-inhibited cells in the network. To standardize the comparison, we begin all simulations with the same initial conditions and use three randomly drawn parameter sets for each network type as described previously.

In accordance with our own (Figure 3.8), as well as previous experimental data [44, 4], we begin with 40% of the cells, specifically the dorsal shell region, excited by GABA, and the remaining 60% inhibited by GABA. Starting with the cells in an initially synchronized state, we simulate the network and monitor PER2 levels over time, as is often done experimentally. Figure 3.12A shows snapshots of PER2 rhythms on the 10th day of simulated time, from which it is clear that the GABA-excited cells in the dorsal shell have maintained better synchrony in comparison to the GABA-inhibited ventral core where cells appear to be at all phases. A movie of the full simulation can be found in the supplemental data of [30]. Raster plots from this video (Figure 3.12B) clearly show that the cells excited by GABA (sorted to the top of the raster plot) have higher amplitude rhythms, and are better synchronized as one cluster, while the cells inhibited by GABA (at the bottom) begin to free run and desynchronize over time. This simulation agrees with the role for GABA signaling in synchronizing the excited cells and desynchronizing the inhibited cells proposed above.

The inhibitory GABA cells desynchronize from the synchronized excitatory GABA population, and can achieve an opposite phase if a strong enough signal is sent from the excitatory GABA population. This is shown in a random network with a 60:40 proportion of excited to inhibited cells in Figure 3.13A, and for an 80:20 excited:inhibited

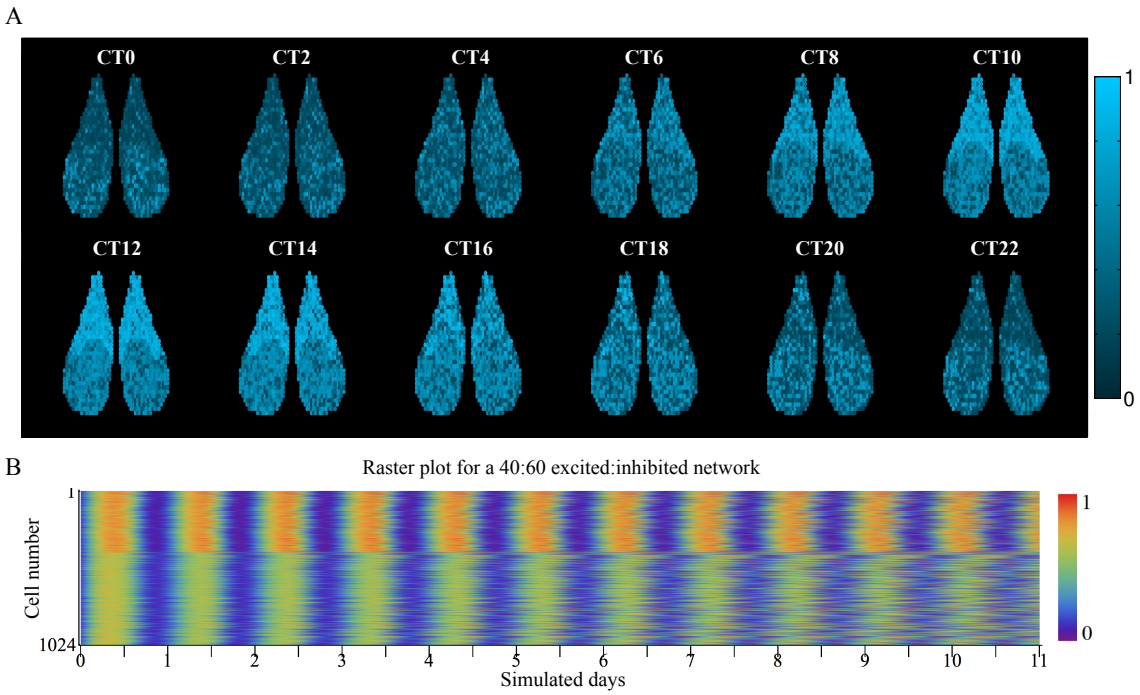

Figure 3.12: Cells excited by GABA retain synchrony over time. (A) Snapshots of PER2 rhythms in a simulated SCN every two hours over the tenth day of simulated time (CT0 to CT22 from left to right, top to bottom, all values normalized by the maximum value in the simulation). A movie of the full simulation can be found in the supplemental data of [30]. The cells excited by GABA, located in the dorsal shell region form a clear cluster. Circadian time is determined relative to the peak in whole SCN PER2 protein levels, which is defined to be CT12. (B) A raster plot of PER2 rhythms for the full 11-day simulation. Cells excited by GABA are sorted to the top, and can be seen to retain synchrony better over time whereas those inhibited by GABA desynchronize. Color bars for each scale are shown on the right.

random network in Figure 3.14A. Each of these simulations used a 10% random connectivity for GABAergic synapses in the network, but consistent results are also seen if a small-world connectivity is used. Additional raster plots (Figures 3.14B-C) with small-world connectivity show that synchrony is maintained in the GABA-excited population, but that the GABA-inhibited population does not synchronize in antiphase. Since the number of connections from the excited to the inhibited subpopulation is low in the small-world networks, the tonic signal is not strong enough to force the inhibited population to the antiphase configuration. The process of this antiphase synchronization in a 60:40 excited:inhibited random network is demonstrated in Figure 3.13B, which shows Rayleigh

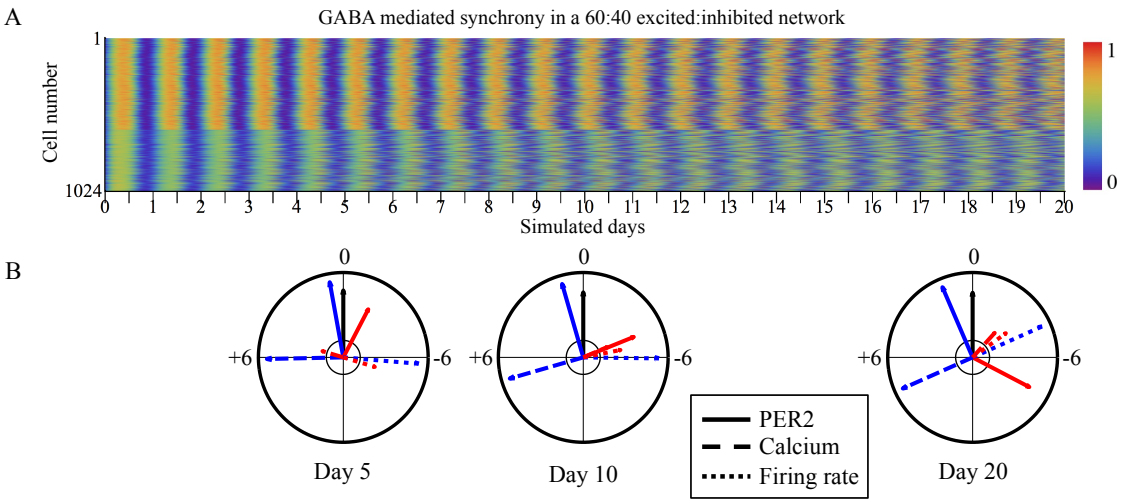

Figure 3.13: Random networks with large fractions of cells excited by GABA form excited and inhibited clusters in antiphase, driven by calcium. (A) A raster plot of normalized PER2 rhythms in a network with 60% cells excited by GABA shows the formation of two clusters, one with the excited cells and one with the inhibited. These clusters increase in coherence as the percentage of excited cells is increased (see Figure 3.14). (B) The formation of these clusters can be seen in Rayleigh plots of the mean PER2 (solid line), calcium (dashed line), and firing rate (dotted line) rhythms for the excited (blue) and inhibited (red) populations. At day 5, each of the three rhythms has the same phasing in both populations. By day 10, however, tonic GABA signaling pushes the inhibited calcium rhythm to antiphase of the excited calcium rhythm, and by day 20, the PER2 rhythm has followed as well. All phases are relative to the total SCN PER2 protein rhythm (black), and are determined as the difference in hours between the trough of the rhythm and the trough of the global PER2 rhythm (positive numbers are advanced and negative delayed).

plots depicting the phases of mean PER2, calcium and firing rate rhythms of the excited (blue) and inhibited (red) populations on days 5, 10, and 20 after the beginning of the simulation, relative to the phase of the mean PER2 level across all cells (black). At 5 days, the three rhythms are separated in phase, with roughly the same phase relationships in both the excited and inhibited populations. By day 10, the calcium rhythm in the inhibited cells has shifted to be antiphase to that of the excited cells, and by day 20, the phase of the PER2 rhythm in the inhibited cells has followed suit. Note that the firing rate rhythms of both populations are, however, still in phase. This illustrates that the molecular, calcium and electrophysiological rhythms need not show the same phase relationship.

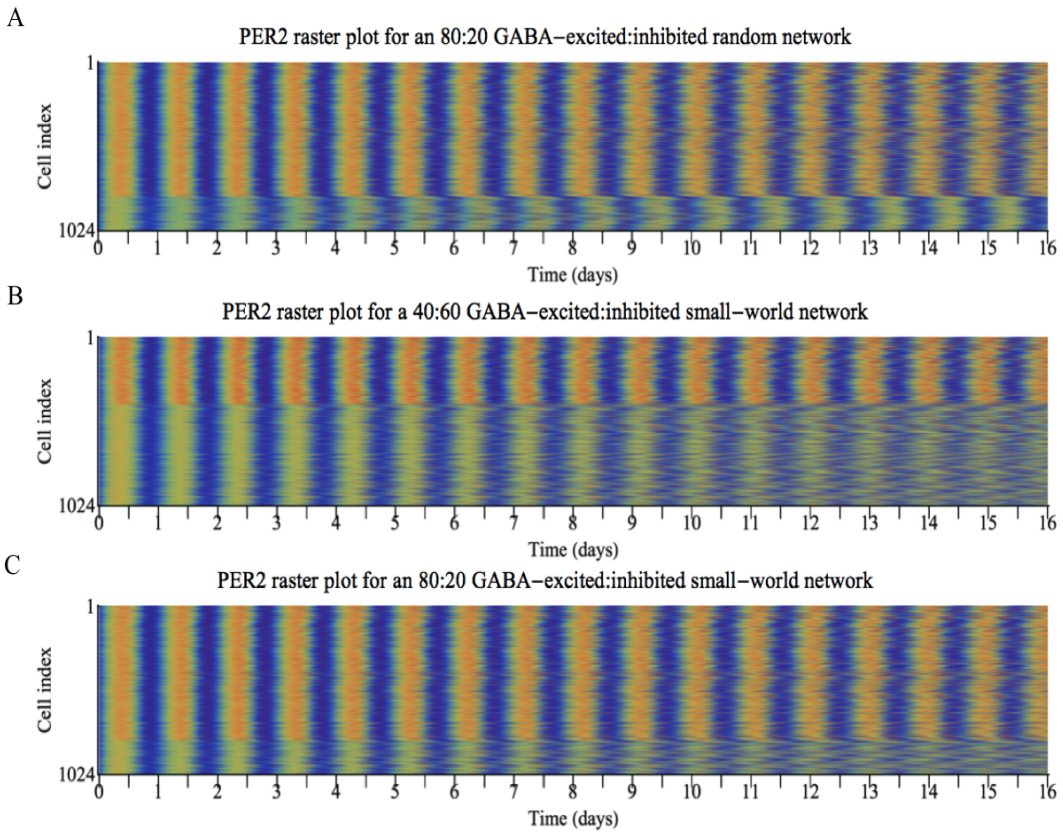

Figure 3.14: Formation of antiphase clusters depends on excitation:inhibition balance and network connectivity. (A) A raster plot of PER2 in a network with random connectivity containing 80% cells excited by GABA shows the formation of excited and inhibited clusters in antiphase (continuation of Figure 3.13). These clusters show increased coherence over the 60:40 excited:inhibited network shown in Figure 3.13. Raster plots in (B) and (C) show small-world networks with 40:60 and 80:20 ratios of GABA-excited to GABA-inhibited cells. In both simulations, the excited subpopulation forms a synchronized cluster, as with the random networks, but unlike in the 80:20 random network, the inhibited subset desynchronizes. Small-world networks used have 10% overall connectivity and a rewiring probability of 5%.

3.5.6 The combined effects of VIP and GABA

VIP is a well-known intercellular signal with an essential role in synchronizing the molecular clocks of SCN neurons, studied more in depth in chapter II. We now use our integrated model, including cellular electrophysiology and GABA signaling, to investigate the effects of having no GABA, or different balances between excitatory and inhibitory GABA within the VIP-coupled SCN network. The subset of cells that produce

and release VIP is determined by immunohistochemistry (Figure 3.2A) and denoted in the model SCN in Figure 3.2B in green. Raster plots from individual simulations are shown in Figure 3.5.6. The combined effects of VIP and GABA remove the clustering of the GABA-inhibited or GABA-excited cells. Additionally, removing GABA causes a tighter distribution of phases in agreement with [44, 91]. Most importantly, increasing the concentration of excitatory GABA cells in the network yields a larger phase distribution, in agreement with previous experimental results (Figure 3.16) [4, 39, 37]. These findings lead to the prediction that the SCN can vary the fraction of cells with different GABA polarities as a mechanism for regulating the degree of synchrony in the network. Additionally, these differences affect the ability of the SCN network to phase shift. Model predicted PRCs for the application of five hours of tonic GABA to the SCN network are shown in Figure 3.17. The PRCs match the shape and phasing of the experimentally found PRC to the GABAA receptor agonist muscimol [119], but differ in amplitude depending on the balance of GABA-excited and inhibited neurons.

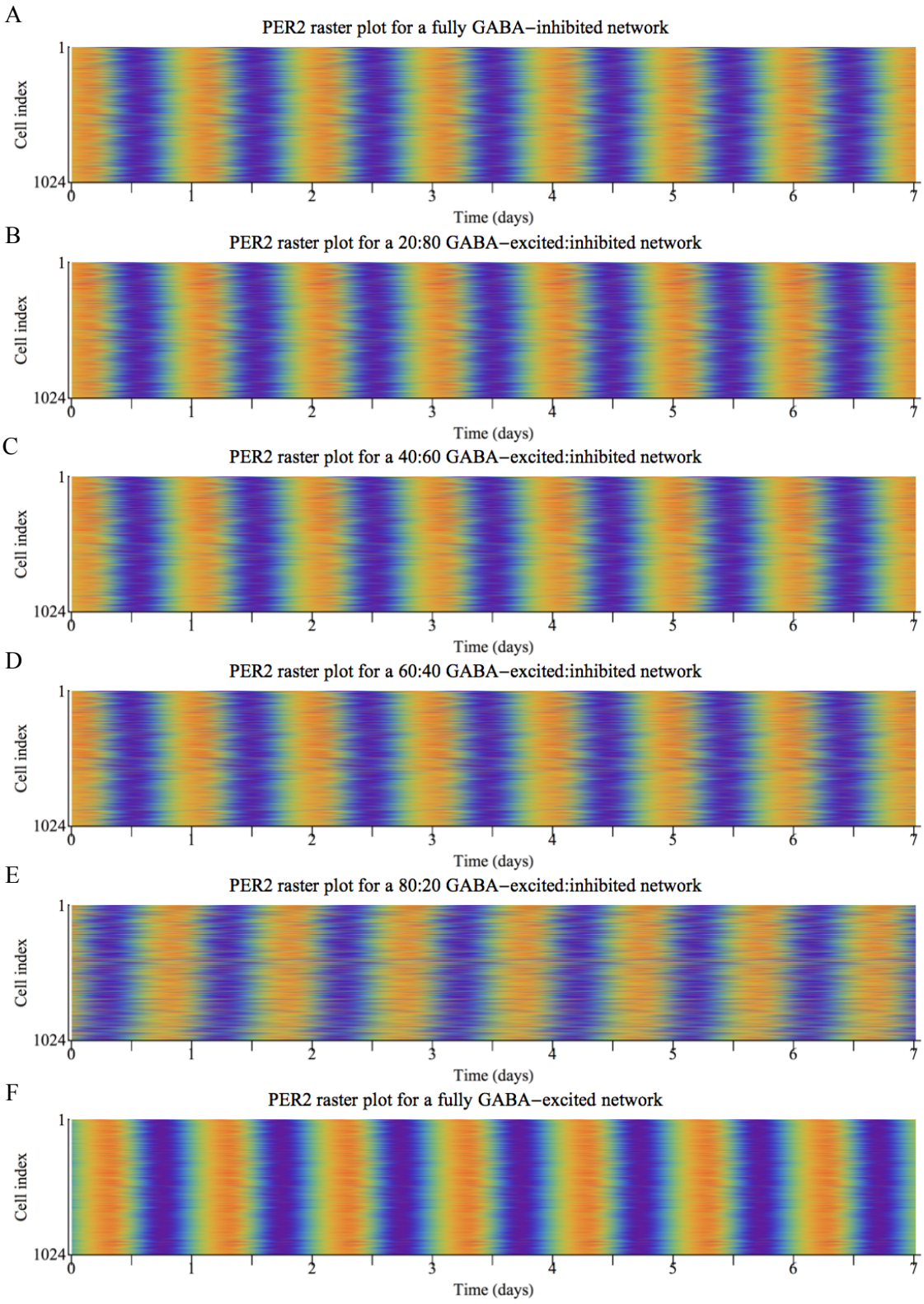
A
PER2 raster plot for a fully GABA−inhibited network
Cell index
1
1024
0
1
2
3
4
5
6
7
Time (days)
B
PER2 raster plot for a 20:80 GABA−excited:inhibited network
Cell index
1
1024
0
1
2
3
4
5
6
7
Time (days)
C
PER2 raster plot for a 40:60 GABA−excited:inhibited network
Cell index
1
1024
0
1
2
3
4
5
6
7
Time (days)
D
PER2 raster plot for a 60:40 GABA−excited:inhibited network
Cell index
1
1024
0
1
2
3
4
5
6
7
Time (days)
E
PER2 raster plot for a 80:20 GABA−excited:inhibited network
Cell index
1
1024
0
1
2
3
4
5
6
7
Time (days)
F
PER2 raster plot for a fully GABA−excited network
Cell index
1
1024
0
1
2
3
4
5
6
7
Time (days)

Figure 3.15: (Previous page.) Sample raster plots of PER2 rhythms in networks with different fractions of excited and inhibited cells. The networks are all synchronized, but have different variances in the distribution of PER2 peaktimes as is summarized in Figure 3.16. All simulations were begun from the same initial conditions, and raster plots are shown for the 23rd-30th days of the simulation. (A) The entirely GABA-inhibited network has a phase distribution with variance between the 40:60 and 60:40 networks. (B-E) Networks with E:I proportions between between 20:80 and 80:20 show the trend that increasing numbers of excited cells leads to increased variance in the distribution of phases in the network. (F) The entirely GABA-excited network has cells most in phase.

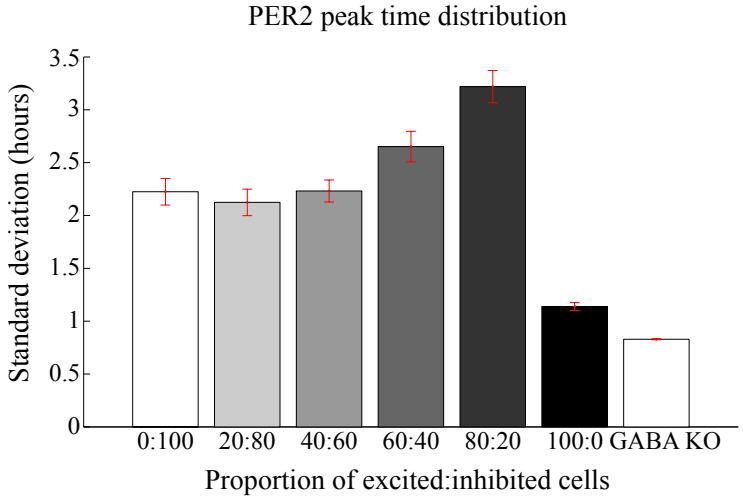

Figure 3.16: Standard deviation of the PER2 peak time distribution as a function of the proportion of GABA-excited to GABA-inhibited cells (E:I) in the network. Mean values and standard errors for three networks with different randomized parameters are shown for each network type. Cells are best synchronized and most in phase in the network where either 100% of cells are excited by GABA or when GABA is knocked out. Networks with E:I proportions between 20:80 and 80:20 are less in phase, with increasing numbers of excited cells leading to increased variance in the distribution of phases in the network. Entirely inhibitory networks (0:100) rank in between the 40:60 and 60:40 networks.

3.5.7 GABA controls tissue-level electrical activity

In addition to its effect on the synchrony of molecular rhythms, GABA has a strong effect on electrical activity. In particular, changing the proportion of excited to inhibited cells in the network changes the amplitude and timing of firing rate rhythms. An example video showing the electrical activity of a network with a 40:60 balance of GABA-excited:inhibited neurons at four circadian times is provided in the supplement of [30] (supplemental movie S2). The model predicts that networks with small fractions of excited

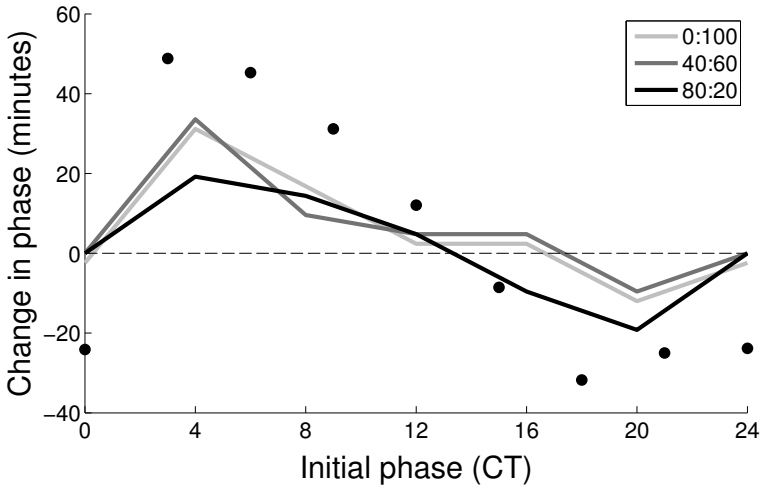

Figure 3.17: The magnitude of phase shifts caused by five hour application of tonic GABA to the SCN network depend on the balance of GABA-excited:inhibited neurons in the network. Phase response curves for networks with 0:100, 40:60, and 80:20 proportions of excited:inhibited cells show that networks with more excited cells have higher amplitude delays, and networks with more inhibited cells have higher amplitude advances. An experimentally determined PRC to the *in vivo* injection of the $GABA_A$ receptor agonist muscimol to the SCN is shown for comparison (black dots) [119]. Circadian time is defined relative to the maximum in whole SCN PER2 protein levels (CT12).

cells will have a single peak in firing rhythms around CT6, but networks with higher percentages of excited cells can actually show a crepuscular firing pattern with peaks around both dawn and dusk (Figure 3.18A). This type of pattern has been seen before experimentally in Per1::eGFP cells in mice [14]. This was also found when hamster SCN were sliced horizontally [58, 22], but not coronally. Thus our model provides a possible explanation: horizontal slices of hamster SCN could contain a higher fraction of GABA-excited neurons than coronal slices.

Separating out the contributions of the excited and inhibited neurons in Figures 3.18B and 3.18C respectively, we find that both subsets can show either unimodal or bimodal firing patterns depending on the balance of excited to inhibited neurons in the network. In most networks, each subpopulation is more likely to have unimodal firing if it is in the majority, and drive neurons with the opposite polarity to fire before or after this peak. The one exception is the entirely excitatory network (100:0), which shows crepuscular firing.

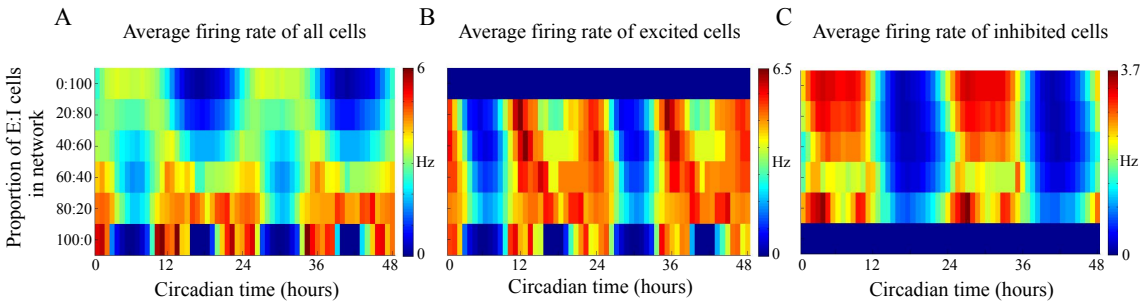

Figure 3.18: Rhythms in firing rate differ in amplitude and phasing depending on the proportion of excited to inhibited cells in the network. (A) Networks with large fractions of GABA-inhibited neurons are unimodal and those with large fractions of excited neurons can show bimodal, crepuscular firing patterns. The excited (B) and inhibited (C) subsets can each show either of these patterns depending on the balance of excited to inhibited neurons in the network. Circadian time is determined relative to the peak in whole SCN PER2 protein levels, which is defined to be CT12.

These plots show that the timing of SCN firing rhythms can be modulated by changing the excitation/inhibition balance in the network, and thus can be shifted to have different phase relationships relative to the molecular clock, without compromising synchrony of the molecular rhythms.

3.6 Discussion

The model developed and tested here provides a framework for studying the complex interactions between the molecular and electrical activities of individual SCN neurons, as well as the synchrony and phase relationships seen within the network. In particular, it is the perfect tool for investigating the conflicting hypotheses about the role of GABA signaling in the SCN. Here we propose a new mechanism, which could help to explain some of the paradoxical results.

We find that GABA signaling in the SCN has two components. Large quantities of GABA are released transiently following action potentials (phasic release). Additionally, a subset of neurons becomes depolarized, and releases a sustained low level of GABA (tonic release). The essential assumption of the model that leads to this prediction is that GABA

release is a function of a neurons membrane voltage. This implies that if cells become hyperexcited and depolarized enough, they can release low levels of GABA even without firing action potentials. Our model predicts, and experiments confirm, that pulsatile GABA can both increase and decrease the firing of a cell, depending on when during the ISI it is provided. As the tonic GABA signal occurs both during the phases that increase, and the phases that decrease the ISI, and also occurs at a low overall level, it does not significantly affect firing rate. However, it does set the overall depolarization of a neuron, which our model, as well as previous studies [31], predicts will set the intracellular calcium level, and can trigger transcription.

Remarkably, this allows the electrical firing of a neuron to become decoupled from its molecular rhythms. Tonic GABA can affect the molecular circadian clock, but this signal, we predict, comes only from a subset of neurons that have achieved a high level of depolarization. This depolarization could be due to signaling from their internal molecular clock, depolarization from long lasting neurotransmitters like glutamate, which transmit information from the retina, or GABA itself. The phasic GABA signal, on the other hand, does not affect molecular rhythms. We hypothesize that this could be important for SCN output, as neurons in the SCN could fire action potentials to transmit an output signal without shifting their own internal timekeeping. Furthermore, it allows tonic and phasic GABA to be separately regulated.

These results raise the interesting question of whether coordinated firing or many phasic GABAergic signals could act like the tonic GABA signal and shift the molecular clock. While theoretically many phasic GABA PSCs could accumulate to give an effect similar to the tonic GABA signal, we find that the number, frequency, and strength of these PSCs would have to be much greater than that previously reported [64]. Due to GABAs relatively fast clearance, it would require constant stimulation by many upstream cells

to obtain the same persistent GABA levels produced by the tonic signal, but because of sparse connectivity [44, 38] and irregular firing patterns [64], this does not happen in the model. Interestingly, a recent study found large phase shifts when many SCN neurons were optogenetically stimulated in unison with an 8 Hz signal for one hour, to mimic the firing of action potentials at 8 Hz [59]. To study this in our model, we incorporate a channelrhodopsin (ChR2)-like current into our electrophysiological model, taking parameters from a previously published model of optogenetic stimulation of ChR2 [138], and simulate this stimulus (details of the methods are given in section 3.2.1). Surprisingly we find a PRC to this stimulus that is remarkably close to that reported experimentally (Figure 3.19). We find that the important difference between optogenetic stimulation and phasic GABA signaling lies in the duration of the signal. The optogenetic stimuli each lasted 10ms and ChR2 has an estimated decay constant of 15 ms [138]. The phasic GABA pulse, on the other hand, lasted only about 5-6ms with a much shorter decay constant of 5.6 ms. Since ChR2 causes a more sustained increase in voltage, and is directly permeable to calcium [92, 23], it causes a much greater increase in intracellular calcium and is therefore effective in shifting the molecular clock, while the phasic GABA signal is not. Thus while we find certain kinds of oscillatory electrical activity can cause calcium influx and shift the molecular clock in a similar way to the tonic GABA signal, the irregular firing of average SCN neurons that causes phasic GABA release does not.

Using the tonic GABA signal, we predict that the GABA-excited cells can work together to send off a synchronizing signal to each other, and one that can push the phase of the inhibited cells away. What matters most in generating a synchronizing signal is the depolarization of the neuron, so factors besides GABA are also important. If this signal arrives before the normal calcium rise in the cell (which begins around CT 3), it will advance the rhythm in excitatory cells, and delay it in inhibitory cells. If it occurs after this

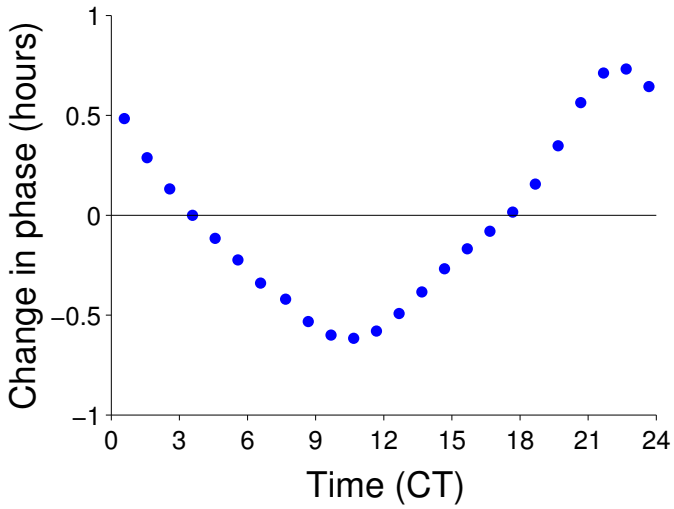

Figure 3.19: Phase response curve of a model cell to simulated optogenetic stimulation. Activation of a channelrhodopsin (ChR2)-like current in 10 ms pulses at a frequency of 8 Hz for one hour causes electrical oscillations at 8 Hz in response to the stimulus as in [59]. Due to the slow timescale of ChR2, significant amounts of calcium enter the cell leading to phase shifts in the molecular clock, unlike what is seen with the phasic GABA stimulus.

calcium rise, the opposite will be seen. As calcium is at low levels from dusk through midnight, GABA has less effect during these phases. This matches what is seen in phase response curves, and what is predicted by our model.

For these reasons, it is not surprising that another coupling agent, VIP, is strongly active in the SCN. In the presence of VIP and GABA, our model predicts the surprising result that has been seen experimentally: that GABA can synchronize or desynchronize neurons in a normally functioning SCN. We add to this the fact that this effect is strongest when a combination of excitatory and inhibitory GABA is present. Only inhibitory or only excitatory GABA yields a more phase-synchronized SCN. Surprisingly, small changes in the proportion of excited to inhibited cells can change the synchrony of the SCN, indicating this balance could be tweaked for regulation of circadian rhythms. In particular, this has interesting applications to the study of daylength encoding in the SCN. Previous studies have shown an increase in excitation in the SCN [39], and a reorganization of the phases of SCN neurons in animals entrained under long days [37, 91, 54]. These observations are

consistent with our model predictions presented here, and are further explored in chapter IV.

Our work presents a different view of synchronization in the SCN that depends not only on the specific connectivity of the network, but also depends highly on the form of the signal produced. We propose that small subsets of SCN neurons (e.g. the 10% that release VIP, or a small set of excitatory neurons) are actually responsible for producing the signals that affect synchrony. This is different than the hypothesis that all SCN neurons contribute to synchrony, and that the large number of neurons reduces noise [68, 127]. We predict that potentially most of the neurons in the SCN, and the majority of the GABA signaling (the phasic portion) do not contribute to synchrony, e.g. to reduce noise, but instead generate a large variety of firing patterns, including bimodal or crepuscular patterns, that are likely important for the SCN output. The specifics and timing of neuronal firing certainly depend on synaptic connectivity, but we find that this firing does not affect synchrony. This provides a potential answer to the question of how SCN neurons are able to show a large variety of electrical activities and generate outputs for the rest of the body without desynchronizing their own rhythms. Such mechanisms are likely found in other parts of the brain, and allow neurons to change their molecular, gene expression or biochemical state in response to some signals, while allowing neuronal processing to simultaneously occur unhindered.

CHAPTER IV

Seasonal encoding at the network level

Portions of this chapter were taken from the manuscript: Myung et al., GABA-mediated repulsive coupling between circadian clock neurons encodes seasonal time. *Under review*, 2015 [90].

4.1 Introduction

In previous chapters, we explored the role of intercellular signaling in synchronizing the cells of the suprachiasmatic nucleus (SCN) in order to generate robust daily rhythms. In-phase synchrony, however, is not the only spatiotemporal pattern that the cellular oscillators in the SCN exhibit. In fact, in addition to being the master circadian clock, the SCN is also a seasonal clock [120, 89] that encodes season-dependent daylength changes by reorganizing the phase relationship between the cells in the network [111, 110, 128, 20, 93]. Subsets of SCN cells form distinct clusters [41] that map to dorsal (shell) and ventral (core) subregions, which are groups of relatively fast and slow oscillators [91]. These clusters are preserved across a moderate range of daylengths (8-16 h) [91], but are phase locked, and separated in phase with an inter-cluster phase difference (phase gap) that changes depending on lighting history to represent the daylength in the SCN [37]. The essential network mechanism that orchestrates this phase gap is as of yet unknown.

Previous studies have focused on complete in-phase synchronization as the default net-

work state of the SCN to explain robust rhythmicity [78, 50]. This is thought to be analogous to a classical model in dynamical systems theory where weak phase-attractive coupling achieves synchrony by eliminating phase differences between individual oscillators [69]. This is insufficient, however, to explain the daylength-dependent cluster phase gap that is stably seen experimentally [91, 37]. Here, we introduce a conceptual model of the SCN network that asymmetrically connects the fast and slow oscillating clusters with phase-repulsive in addition to phase-attractive couplings, which are supported by our experimental data of oscillations in the SCNs isolated from animals entrained under various daylengths. This network structure links the phase gap to the oscillation frequency, particularly in the fast cluster (dorsal SCN), which increases proportionally to the daylength and becomes the highest under long days (LD) and provides tunability to the network.

We further find that the underlying physiological mechanism is modulation of the intracellular chloride concentration, which can adjust the strength and polarity of the ionotropic γ-aminobutyric acid receptor (GABAA)-mediated synaptic input, as proposed in previous works [4, 24, 83]. We show that increasing daylength increases the relative expression of the chloride importer Nkcc1, in line with the recent finding of increased excitation by GABA under LD [39]. Additionally, we find that blocking GABAA signaling or the chloride transporter disrupts the unique phase and period organization induced by the daylength. This strongly suggests that GABAA polarity modulation by intracellular chloride underlies the tunable repulsive coupling by daylength. We evaluate this hypothesis using the multiscale SCN model developed in chapter III. In chapter III, we showed that modulating the proportion of GABA-excited and GABA-inhibited cells in the network can tune both the period and degree of synchrony in the SCN. Here, we further use the model to show that the asymmetric distribution of GABA-excited and inhibited cells causes active phase repulsion between the two clusters, and that region-specific changes to the period

and GABA response of SCN neurons can reorganize the phase relationship among circadian oscillators to encode the daylength to which an animal has been entrained.

4.2 Materials and Methods

4.2.1 Daylength entrainment of Bmal1-ELuc transgenic mice and SCN slice culture

We used luciferase reporter mice on a C57BL/6J background (SLC Japan) carrying a heterozygote transgene generated by Nakajima [94] at an age around postnatal 60-90 days. Experimental protocols for breeding, daylength entrainment, SCN slicing and imaging were identical to a previous study [91]. Animal entrainment and SCN slice culture were performed by Jihwan Myung in the lab of Toru Takumi. The control daylength condition was defined by the equinox light-dark ratio (12:12 hr light:dark, L:D). The seasonal daylength conditions simulated summer and winter conditions. In the short day (SD) paradigm, the light phase lasted for 8 hrs and the dark phase for 16 hrs (8:16 L:D) and in the long day (LD) paradigm, the light phase lasted for 16 hrs (16:8 L:D). Daylength entrainment was performed for a minimum of 30 days before sampling [128]. All SCN slices were taken from the mid-posterior (MP) section of the SCN. The slice culture was imaged continuously with an exposure time of 15 mins. For continuous bioluminescence monitoring of the whole culture dish, we used a 24-dish-on-a-wheel photomultiplier system that counts photons for 1 min every 15 mins, per dish. For some experiments, the SCN explant from the MP section was micro-dissected into the dorsomedial (DM or D) region and the ventral region (V), which was further dissected into ventromedial (VM), and ventrolateral (VL) regions. This scheme of micro-dissection was as previously described [91] and is depicted in Figure 4.1C.

4.2.2 Measurement of intracellular free chloride concentration

We estimated the chloride concentration using quenching of MQAE (N-(Ethoxycarbonylmethyl)-6-methoxyquinolinium bromide, Molecular Probes) fluorescence by chloride as in [30], and as described in the methods in section 3.4.2. To determine the intracellular chloride concentration, we used the Stern-Volmer relation, $[Cl^{-1}] = K_{SV}^{-1}(F_0/F - 1)$, and calibrated using known chloride concentrations at 10, 20, 30, and 40 mM. The Stern-Volmer constant (K_{SV}) was estimated to be 13 M^{-1} in aqueous solution but was variable across the SCN samples in situ (10-25 M^{-1}) due to cellular exclusion and fluorescence bleaching of the MQAE dye.

4.2.3 SCN model simulations

Detailed simulations of SCN signaling were performed using the multiscale, multicellular SCN model, developed in chapter III. As before, we simulate a network of 1024 SCN neurons. Each neuron contains a biochemical model, based on mass action kinetics, of the negative feedback loops regulating clock gene expression [60] and a conductance-based model of SCN electrophysiology [31]. All parameters and coupling are as described in chapter III. The model enabled us to evaluate the overall network effect of differentially distributed chloride concentrations in single cells by varying the E_{GABA} for different cells in the network (-32 mV for GABA-excited and -80 mV for GABA-inhibited cells respectively). All other electrophysiology parameters were unchanged between the two populations. Short day SCN simulations used all original parameters. For the long day SCN simulation, all molecular clock parameters were scaled to 102% of their original values in the 40% of SCN cells in the dorsal shell; ventral SCN parameters were unchanged. This led to effective intrinsic periods of 23.7 hrs in the dorsal and 24.2 hrs in the ventral SCN.

4.3 Results

4.3.1 Representation of entrained daylength in the SCN by network interactions

To determine how daylength is internally represented, we performed time-lapse imaging of single-cell bioluminescent Bmal1 reporter activity (Bmal1-ELuc) in SCN explants from mice previously entrained under long day (16:8 h light:dark; LD) and short day (8:16 h light:dark; SD) light-dark cycles for a minimum of 30 days of entrainment. Imaging revealed that the phase distribution of the cellular Bmal1-ELuc oscillations in the SCN becomes narrower after SD and wider after LD entrainment (Figure 4.1A). The phase reorganization occurred without breaking dorso-ventral (D-V) clusters [91]. The D-V phase gap increased linearly with daylength from SD to LD (Spearman's ρ=0.045, $p<0.05$), and with significance (SD vs LD and 12:12 vs LD, $p<0.05$; Welch's t-test, SD SCN explants n=8; 12:12 n=6; LD n=6) (Figure 4.1B).

We found that the initial phase distribution is retained in each subregion. We cultured microdissected SCN subregions (dorsomedial [DM], ventromedial [VM], and ventrolateral [VL]) diagrammed in Figure 4.1C representing each of the phase clusters [91]. In the isolated SD-entrained SCN subregions, the first peak time (acrophase) of DM, VM, and VL were close together (Figure 4.1D, upper; SD: DM n=12, VM n=17, VL n=12), while in the isolated LD-entrained SCN subregions, a wider phase gap was seen between the DM and ventral subregions (VM and VL) (Figure 4.1D, lower; LD: DM n=12, VM n=13, VL n=11). Unlike the intact SCN explant which maintained the phase gap throughout culture, the phase relation across the isolated subregions changed as cycles progressed, suggesting that the phase organization is dependent on the network coupling (Figure 4.1D). The D-V phase gap in the isolated subregion culture is significantly wider in the LD entrained group than in the SD group (both DM-VM and DM-VL comparisons, LD: $p<0.01$, SD: $p<0.05$; Mann-Whitney U test) (Figure 4.1E).

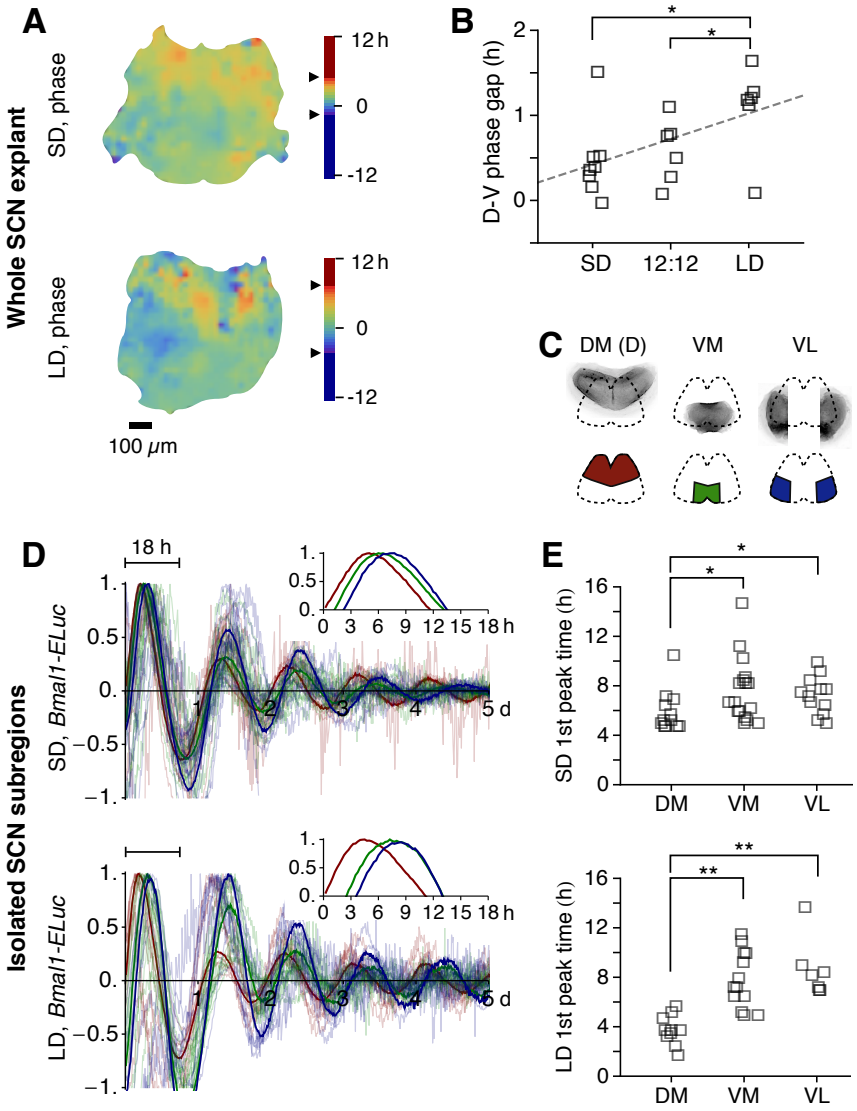

Figure 4.1: Daylength regulates synchrony of Bmal1 oscillations in the SCN. (A) Short day (SD) entrainment induces a narrow phase distribution (upper) whereas long day (LD) widens the phase gap between the dorsal and the ventral subregions of the SCN (lower). The arrows on the scale bar indicate standard deviation (1σ) of the phase distribution. (B) The dorso-ventral (D-V) pairwise phase gap in the first day in culture increases nearly linearly with daylength across SCNs (*p<0.05; Welch's t-test). (C) The isolated SCN subregions (DM, VM, and VL, upper) are diagrammatically illustrated with each subregion color-coded (in red, green, and blue, respectively, lower) for (D). (D) Ensemble averages (thick line) of detrended, normalized Bmal1-ELuc oscillations in the isolated SCN subregions are presented against plots of all samples (half transparent) from SD (upper) and LD (lower) entrainments. The relative phase distribution is retained in the isolated subregions in the first day in culture (inset: ensemble average for first 18 hrs). (E) The phase gap as a median peak time difference between DM and VM also increases with daylength (*p<0.05; **p<0.01; Mann-Whitney U test).

4.3.2 GABAergic connections mediate stable phase-gap

GABA, the most predominantly expressed neurotransmitter in the SCN, can have both inhibitory and excitatory effects [4, 24], making it difficult to interpret its role in terms of circadian synchronization [78, 9, 44]. Since the same GABAergic signal can have asymmetric effects depending on the intracellular chloride concentration in downstream cells [4], we tested GABA as a physiological source of the repulsive coupling necessary to create the phase gap, by applying the GABAA blocker gabazine (GBZ). GBZ showed clear and immediate removal of the short period aftereffect in the cultured SCN from LD entrained animals (Figure 4.2A, bottom). It also reduced the clear D-V clustering that was seen in the control (Figure 4.2A, top).The effect of GBZ was not significant in the SD entrained SCN (Figure 4.2B) but was pronounced in the LD entrained SCN (Figure 4.2C).

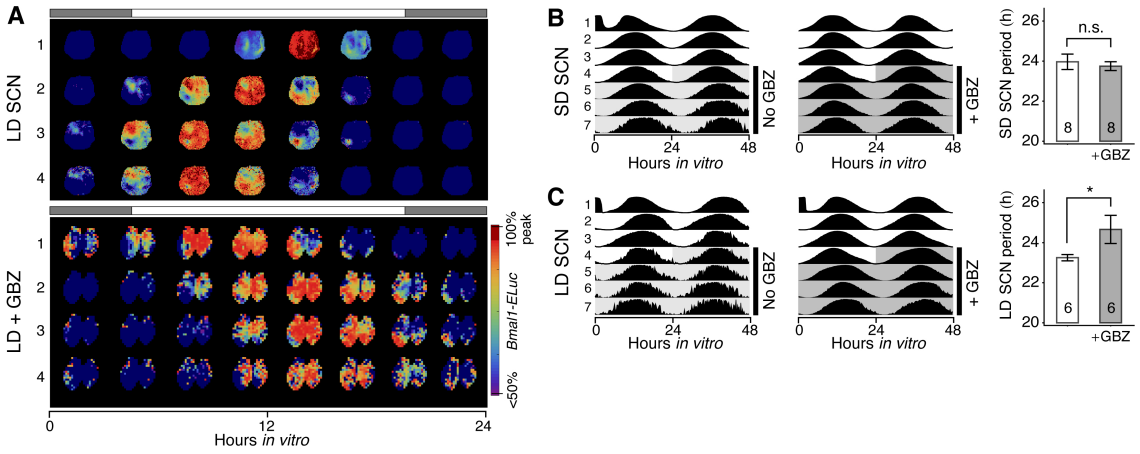

Figure 4.2: GABAA inhibition disturbs the phase and period organization caused by long or short daylength. (A) Sequences of normalized Bmal1 oscillations in the long day (LD)-entrained SCNs are shown for every 3 hours (color bar on the bottom right). The clear D-V cluster formation and the short oscillation period can be seen in the control LD SCN (top). Application of the GABAA blocker gabazine (GBZ) lengthens the free-running period in culture while making the cluster separation less clear (bottom). (B, C) The effect on the free-running period is observed in the tissue-level rhythm (measured using a photomultiplier tube). GBZ has no effect on the SD-entrained SCN culture (B) but in the LD-entrained SCN culture (C), GBZ increases the period (*p¡0.05, Students t-test; n indicated in the bar graph).

4.3.3 Model predicts GABA-response polarity and changes to intrinsic frequency are used to encode daylength

In chapter III, we showed how the balance between excitatory and inhibitory GABA signaling could be tuned to create antiphase clusters and modulate tissue level synchrony. Based on these results and previous studies [4], we hypothesized that the role of GABA in establishing the phase clusters seen experimentally was likely due to preferential excitation by GABA in the dorsal SCN [4]. By modulating the degree of GABA excitation and the intrinsic periods in the dorsal and ventral regions, we found that the realistic model could reproduce the reorganization by daylength in the SCN. Figure 4.3A reproduces the formation of dorsal and ventral phase clusters with a significant phase gap as in LD conditions, and of the synchronized clusters with no phase gap as in SD. The phase gap between mean Bmal1 levels in the dorsal and ventral SCN is shown in Figure 4.3B, and matches that seen experimentally as well (Figure 4.1D). We found that the necessary conditions for generating the LD phenotype were a decreased period in the dorsal cells, decreased by scaling all dorsal parameters to 102% of the ventral levels. The phase gap increased as the intrinsic period of the dorsal cells was decreased, with only a small difference in period ($\sim$ 0.5 hrs) necessary to create the LD phase gap. The coherence of the cluster and stability of the phase difference between clusters was also enhanced by setting all dorsal cells to be GABA-excited, and all ventral cells to be GABA-inhibited. The combination of these two changes led to the stable phase gap between clusters, and mimicked what was seen under LD entrainment.

The model enables us to explore the physiological changes in coupling needed to create the phase gap. The model predicts two distinct coupling signals: the vasoactive intestinal peptide (VIP) signal and the tonic GABA signal. The effects of these two coupling signals are shown in Figure 4.3C, with cells sorted such that the dorsal cells are numbered 1-

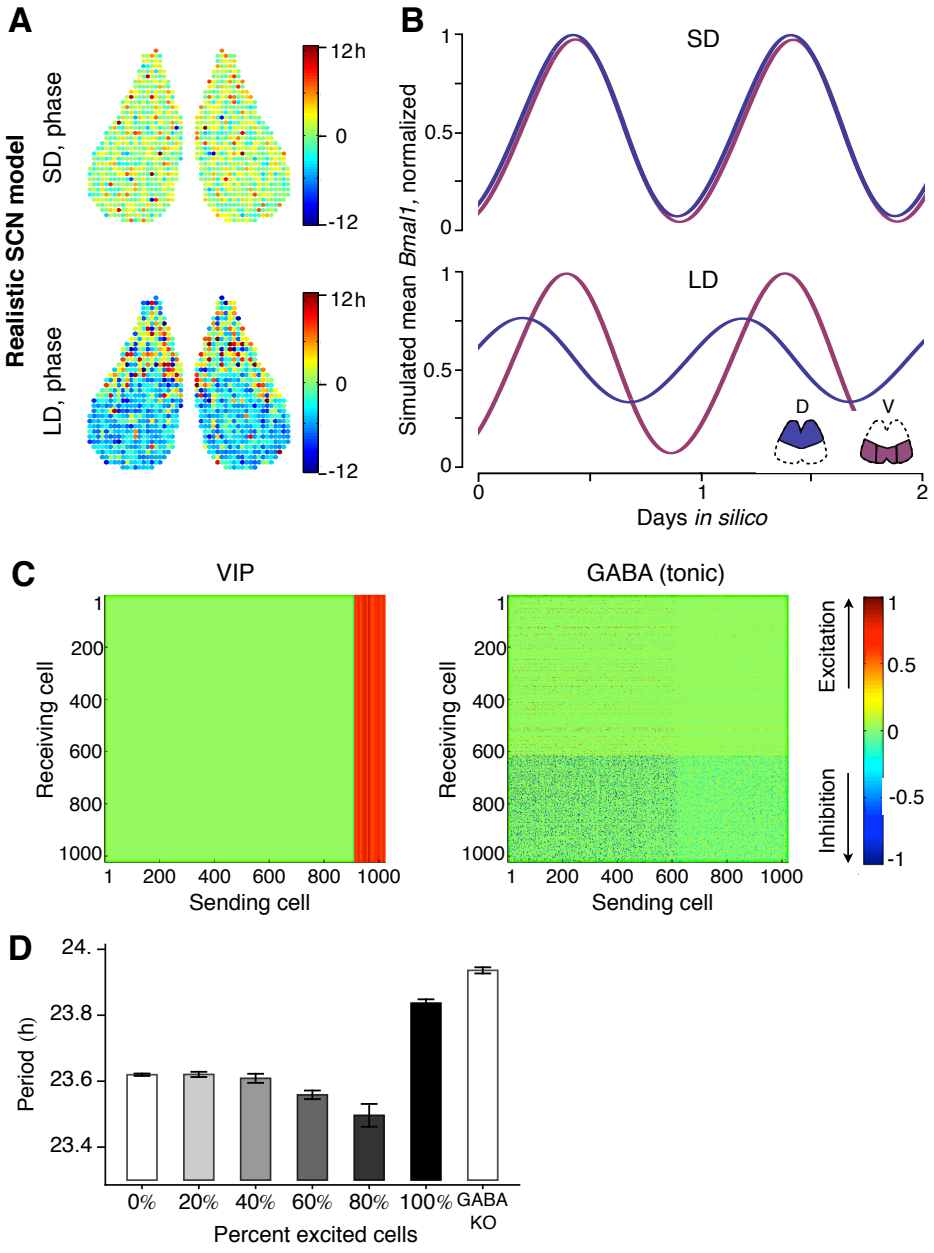

Figure 4.3: Multiscale SCN model reproduces daylength-dependent reorganization of phases. (A) The model reproduces the separation of phases between dorsal and ventral oscillators under simulated LD, which is minimal under simulated SD. (B) The phase separation is re-plotted as the averages of the Bmal1 transcript levels in dorsal and ventral regions. (C) Coupling signals in the network have two components: strong attractive coupling through VIP (red horizontal lines) and asymmetric repulsive coupling through GABA (blue vertical dotted lines). The color bar indicates the relative strength of coupling. (D) Simulations predict both the shortened dorsal period due to increased GABA excitation during LD and the lengthened period in cultured SCN during GBZ application as consequences of the change in E/I ratio.

405 and the ventral cells are numbered 406-1024. Under LD, the higher proportion of GABA-excited cells in the dorsal SCN speeds up the transcriptional oscillations in the excited cells. GABA signaling occurs between all cells in the network, but as in section 3.5.3, only the most depolarized cells release the tonic GABA signal that is able to shift the molecular clock. This signal, released by the GABA-excited cells in the dorsal SCN, inhibits the ventral cells (Figure 4.3C, right), causing phase-repulsion between the GABA-excited cells in the dorsal and GABA-inhibited cells in the ventral SCN. The ventral SCN, on the other hand, produces VIP, a known synchronizing neuropeptide, which works as a strong attractive coupling agent. This draws the phases of the two clusters closer together (Figure 4.3C, left). The combination of these two coupling signals creates a push-pull that leads to a stable phase gap. In the absence of VIP, the stable phase gap is lost, and the two clusters begin to free run with different periods (Figure 4.4). The relative phase gap between the two populations increases after LD entrainment, as the GABA-excited cells in the dorsal SCN shorten their period and repel the ventral GABA-inhibited cells. This modulation of repulsive coupling depends on the balance of excitation and inhibition (E/I) in the network [39, 30]. Consistent with the finding of increased GABA excitation under LD, higher E/I (80/20) shortens the period and the absence of GABA increases the period (Figure 4.3D), as in our experiments (Figure 4.2C). This scheme reproduces our findings from Bmal1-ELuc imaging of the SCNs entrained under SD and LD, and proposes that the stable phase gap is maintained through a balance of GABA-based repulsion and VIP-based attraction.

4.3.4 Daylength modulation of GABAA coupling by adjustment of chloride homeostasis

We hypothesized that changes in GABA-response polarity, dependent on intracellular chloride concentration, were caused by enhanced expression of the chloride importer Nkcc1 [24, 13] after long day entrainment. In the SCN culture, chronic application of the

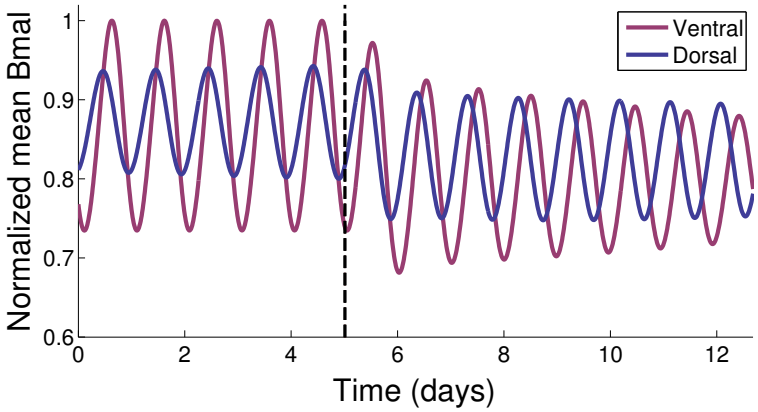

Figure 4.4: VIP knockout in LD entrained network predicts free-running of dorsal and ventral clusters. Mean Bmal levels in dorsal and ventral clusters before, and after simulated loss of VIP shows that the stable phase gap is lost after VIP knockout (indicated by black dashed vertical line). Clusters then free run with different periods. Decrease in amplitude in the ventral mean Bmal level is due both to a decrease in single cell amplitude as well as to a loss of synchrony within the cluster.

chloride transporter inhibitor furosemide (Furo) increased the period of Bmal1-ELuc oscillations in the dorsal SCN, but not in the ventral SCN, when compared to the control condition prior to drug application (Figure 4.5A). Co-application of gabazine prevented this effect, suggesting that the period lengthening is GABAA-mediated, and a consequence of the chloride concentration in the dorsal SCN (Figure 4.6). As our asymmetric repulsive coupling model predicts, this dorsal-specific lengthening of period causes the whole SCN to lengthen its period (Figure 4.5B) due to the organization of the SCN network. No such effect was seen when Furo is applied to the hippocampus (Figure 4.5C), which harbors a circadian clock but has no known role in seasonal timekeeping. Supporting these findings, the relative spatial bias of chloride concentration, estimated by MQAE fluorescence, increased across the SCN after LD entrainment (Figure 4.5D, left), which is decreased by Furo preferentially in the dorsal SCN (Figure 4.5D right). At the transcript level, the expression of the neuronal chloride importer Nkcc1 increased relative to that of the chloride exporter Kcc2 in the LD SCN (Figure 4.5E; $p<0.01$, Welch's t test). If indeed the intracellular chloride concentration modulates the SCN network to encode the daylength, the

low intracellular chloride condition caused by chloride importer blockade should switch a normal equinox (12:12 hr light:dark)-entrained SCN into an SD entrained SCN. Consistent with this prediction, we found that application of furosemide in the equinox (12:12)-entrained SCN narrowed the internal phase gap and lengthened the period of Bmal1-ELuc oscillations in the entire explant, consistent with what was seen in the SD-entrained SCN (Figure 4.5F). These results suggest that modulation of chloride homeostasis can be a modus operandi for daylength encoding in the SCN.

4.4 Discussion

We propose asymmetrical repulsive coupling and region specific period modulation as essential network mechanisms that enable daylength encoding in the SCN. Asymmetrical coupling has been proposed previously, with the fundamental idea of phase repulsion implicit in the morning-evening oscillator interpretation of behavioral splitting under constant light [104]. Similarly, internal desynchronization has been modeled as two oscillators for sleep-wake cycles that are mutually repulsive of one other [66]. Various scenarios with asymmetric coupling between two oscillators have also been considered using Pittendrigh-Pavlidis equations, which showed that a stable, but not anti-phasic, phase gap is possible when the positive (attractive) and negative (repulsive) coupling have much different strengths [98]. Here we present evidence that this asymmetric coupling structure exists at the cellular level, and demonstrate its functional role in daylength encoding. Repulsive coupling keeps SCN neurons from complete in-phase synchronization, and instead, locks them in two clusters with a stable phase gap in between. The cluster phase gap is tunable through effective modulation of repulsion strength, which is physiologically achieved by modulating intracellular chloride concentration and period.

Our experimental results point to modulation of GABA polarity as the underlying phys-

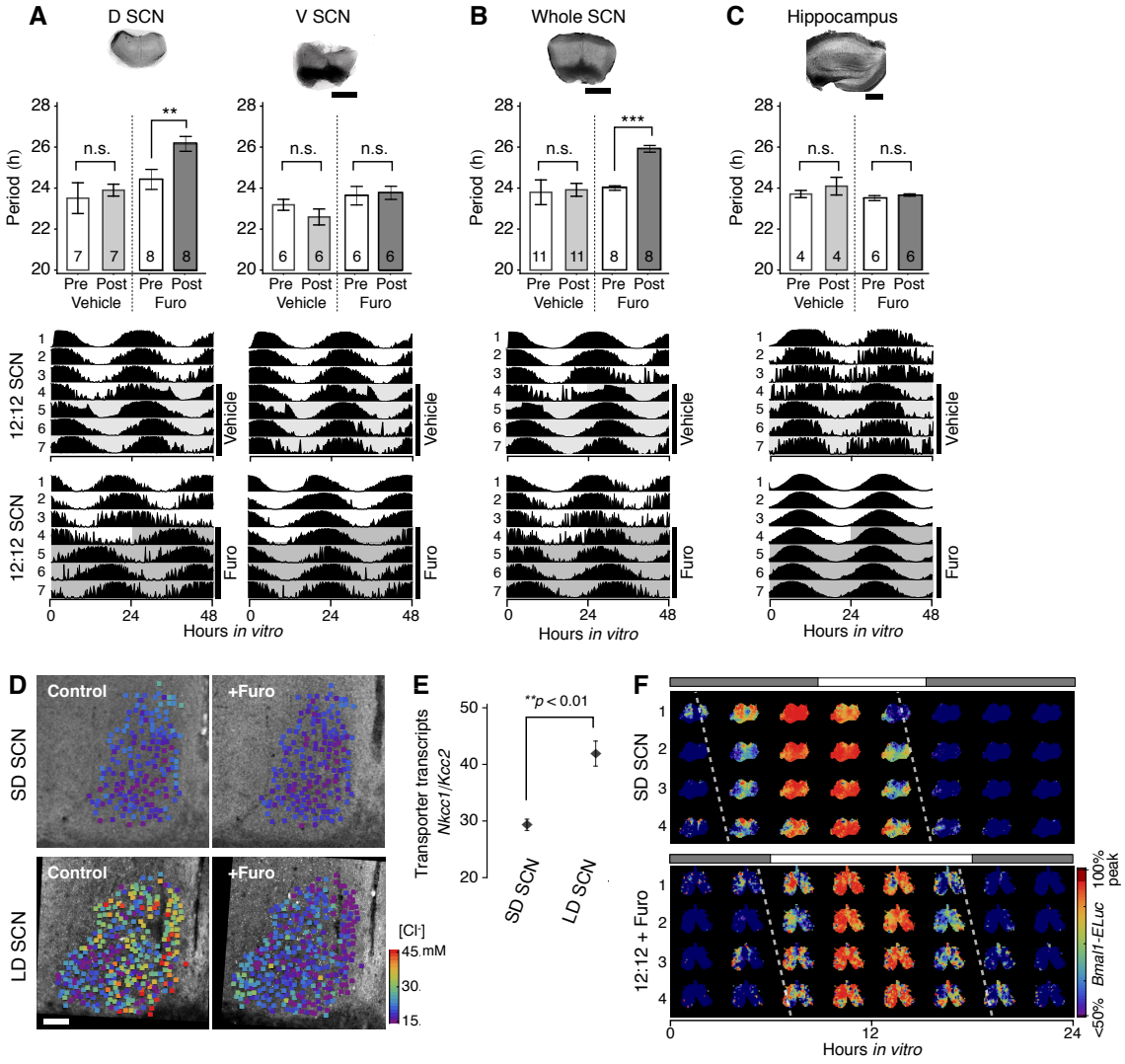

Figure 4.5: Intracellular chloride concentration manipulation disturbs the phase and period organization caused by long and short daylength entrainment. (A) The chloride transporter blocker furosemide (Furo) preferentially increases the period of Bmal1-ELuc oscillations in the isolated dorsal (D) SCN microsection only, entrained under 12:12 light-dark cycles. Representative pictures of cultured explants (top), statistics across explants (middle), and representative Bmal1-ELuc activity double-plots from the explants (bottom; light shade indicates vehicle application and dark shade indicates Furo application) are presented (**p<0.01, ***p<0.001; paired t-test; n indicated in the bar graph). (B) Slowed oscillations in the dorsal SCN induce a slow-down of the whole SCN slice under application of Furo. (C) This effect is specific to the SCN, and no period effect from Furo is seen in hippocampus (shaded region indicates drug application). (D) MQAE imaging of a unilateral SCN shows higher intracellular chloride in LD SCN (bottom left) compared to SD SCN (top left), which is decreased by application of Furo (right). (E) LD entrainment causes relative up-regulation of the chloride importer (Nkcc1) transcripts compared to the chloride exporter (Kcc2) transcripts. (F) An equinox (12:12) entrained SCN in culture can mimic the lengthened free-running period of the SD entrained SCN under application of Furo.

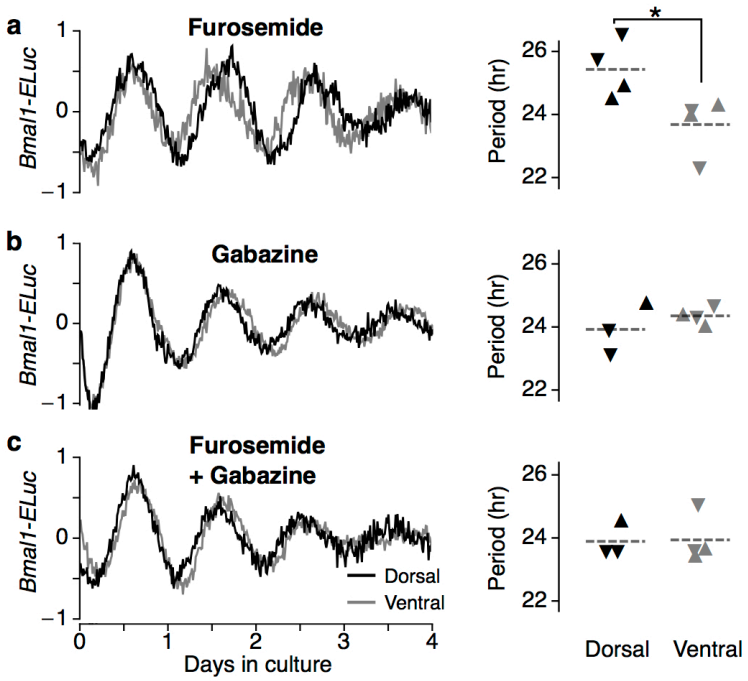

Figure 4.6: Intracellular chloride levels control dorsal SCN period through GABA signaling. (A) The chloride transporter blocker furosemide increases the period of Bmal1-ELuc oscillations in the dorsal SCN microsection but not in the ventral SCN microsection (12:12 SCN, n=4 per group; *p¡0.05, Student's t-test). (B) Application of the GABAA blocker gabazine alone had no effect on the period of Bmal1 oscillations in the microsections. (C) Application of both blockers, furosemide and gabazine, blocked the period increase in the dorsal SCN seen with furosemide alone, demonstrating that the effect of chloride homeostasis modulation acts through GABAA.

iological mechanism [83, 39] responsible for daylength encoding via phase gap between the SCN oscillators [128]. Although GABA is the most abundant and ubiquitous neurotransmitter in the SCN, reports on its role for synchronization have been mixed. In neonatal preparations, it is a synchronizer [78] or plays an unclear role [9] but in mature animals (>3 weeks old), it can be a desynchronizer [44] or can have both effects depending on the relative phase difference between SCN subregions [37]. This is in contrast with VIP, which works as a synchronizer in the SCN [8], and plays a coherent role in the phase reorganization after entrainment under varied daylengths [37]. Furthermore, GABA's polarity can switch from inhibition to excitation depending on time of the day [132] or the subregion of the SCN [4] through modulation of intracellular chloride [74]. Chloride transporters can

switch the GABA-response polarity [24], and are expressed in a region-specific manner in the SCN [13]. Because of all of these complications, GABA's role in the SCN has been difficult to assess.

Here, we predict a balance between attractive and repulsive couplings determines the quasi-stable phase gap that encodes daylength. Our realistic model finds that the anatomical bias in intracellular chloride causes GABA to excite dorsal SCN neurons and inhibit ventral ones (Figure 4.3C, right), which causes different responses to GABA [30] while creating higher synchrony in the dorsal SCN than the ventral. This is consistent with the higher synchrony in firing rate rhythms in dorsal SCN under LD [20] and dispersed phases in the ventral SCN [110]. The weaker effective repulsive coupling in SD-entrained SCN is also consistent with higher synchrony [111] and molecular rhythmicity [121]. The model predicts that VIP provides the attractive coupling force, consistent with the finding that its removal markedly compromises the balance between the two asymmetric couplings. GABA's action is difficult to define in simple terms as it depends on the intracellular chloride concentration, a fact which has caused a great deal of confusion and debate in the literature (for example, see [132, 4, 24]). Our experimental results, however, suggest that the modulation of GABA response through the reorganization of chloride homeostasis makes a potent physiological pathway for daylength encoding. This interpretation is consistent with the new finding that the GABA-mediated excitatory input increases with daylength [39], given the increase of the chloride importer over the exporter after LD entrainment.

Synchronization is a powerful mechanism for bringing order out of a number of neurons. But if all neurons are locked in the same state, they are unable to process diverse and complex information. By allowing for different phase relationships within subsets of neurons, the SCN can encode more than just circadian timing. The spatiotemporal pattern of activation in the SCN is programmable by seasonal daylength and persists on a timescale

much longer than circadian. Our study identifies an active force resisting complete synchronization as a mechanism for metastability in the SCN, which enables the encoding of daylength information. Because of these findings, we believe that the SCN potentially makes a powerful platform to study the brain's metastable states and methods for encoding diverse signals on different timescales.

CHAPTER V

Clock control of electrical activity through a kinase

Portions of this chapter were taken from the manuscript: Paul JR, DeWoskin D, Forger DB, Gamble KL, Kinase regulation encodes daily timekeeping in neuronal excitation. *In preparation*.

5.1 Introduction

One of the largest open questions in circadian biology is how SCN electrical activity is regulated. As discussed in section 1.1.3, SCN neurons show a variety of electrical activities which change throughout the course of the day. These activities are of central importance as they are thought to be an essential output signal from the SCN to other brain regions. Understanding how electrical activity is regulated is therefore necessary for understanding, and potentially controlling, the way timing information is passed on from the SCN to the rest of the brain. In section 3.5.3, we showed that our multiscale model predicted the timing of these electrical activities in individual SCN neurons could be modulated by GABA signaling within the SCN network. Additionally, we showed in section 3.5.7 that changing the balance of GABA-excitation and inhibition in the network could modulate the timing and magnitude of the tissue-wide peak firing rate. This provides a mechanism by which the network can alter its activity through the coordination of both intracellular chloride levels and intercellular signaling through GABA.

At a single cell level, the circadian control of electrical activity in our model, however, was phenomenological and based on experimental electrophysiology recordings [14] and studies of ion channel expression. While there is good evidence that the mRNAs of some ion channels do show circadian oscillations [67, 84, 105, 31], transcriptional control of ion channel expression is a metabolically inefficient means of controlling electrical activity, since it requires the daily production and destruction of ion channels. Furthermore, this is a slow process that would require minutes to hours to occur. Since the SCN needs to alter its activity more rapidly in response to external perturbations, it is likely there are other control mechanisms in place.

Here we use our detailed multiscale model to investigate a potential role of glycogen synthase kinase 3 (GSK3) in modulating neuronal activity. A previous study reported increased neuronal firing in the SCN in a mouse with increased activity of GSK3, a key kinase involved in the intracellular molecular circadian clock [100]. This could point to an alternate, non-transcriptional and more responsive, mechanism by which the molecular clock could control firing activity in the SCN. Through a combination of experiments and modeling, we show that GSK3 activates a persistent sodium current (I_{NaP}) that regulates the excitability of SCN neurons. By incorporating this persistent sodium current into our model, we propose find that the persistent sodium current is carefully balanced by a calcium activated potassium current in order to control firing activity. The balance between these currents mainly affects the after-hyperpolarization following an action potential. As I_{NaP} increases in magnitude, the after-hyperpolarization decreases, allowing the neuron to fire more rapidly. This points to a novel, efficient, way that internal molecular clock regulates the firing rate of SCN neurons and controls circadian outputs to the rest of the body.

5.2 Results

5.2.1 Inhibition of GSK3 suppresses neuronal excitability in a time-of-day dependent manner

It was reported previously that a mutant mouse model with constitutively active GSK3 showed increased spontaneous firing activity at night [100]. In order to determine whether GSK3 influences excitatory activity acutely, we conducted targeted loose-patch recordings of the spontaneous firing rate (SFR) of SCN neurons following GSK3 inhibition during the day (ZT 4-8) or night (ZT 14-18). Chronic bath application of CHIR, a GSK3 inhibitor, or vehicle control to SCN slices revealed that GSK3 inhibition suppressed SCN activity in a phase-specific manner ($p < 0.05$; Fig. 5.1A, B). During the day, cells treated with CHIR exhibited a significantly lower SFR than vehicle-treated cells ($p < 0.001$). Conversely, at night, both treatment groups were similarly suppressed, with no significant difference between the two groups ($p > 0.05$). To confirm that the observed day-time suppression was due to GSK3, we replicated our results with another GSK3 inhibitor, SB415286, and found that spike rate was reduced by 66% compared to vehicle (mean $\pm$ SEM, vehicle: 5.05 ± 0.44; SB415286, 1.71 ± 0.28; n = 34-38 cells/group). These results suggest that inhibition of GSK3 suppresses SCN neuronal excitability during the day.

To determine whether CHIR-induced suppression of excitability was due to membrane hyperpolarization, we conducted whole-cell current clamp recordings during the day. Consistent with recent reports [133, 14], day-phase SCN neurons exhibited a wide range of resting membrane potential (RMP) which was not affected by GSK3 inhibition ($p > 0.05$; Fig. 5.1C). There was also no significant difference in input resistance ($p > 0.05$), suggesting that the decreased excitability in CHIR-treated neurons was not due to an increase in the potassium leak conductance [67]. As seen in the vehicle-treated controls during the midday (Fig. 5.1C), SCN neurons are capable of exhibiting multiple phenotypes in spontaneous electrical activity [31] and can be classified as silent, spiking, having depolarized

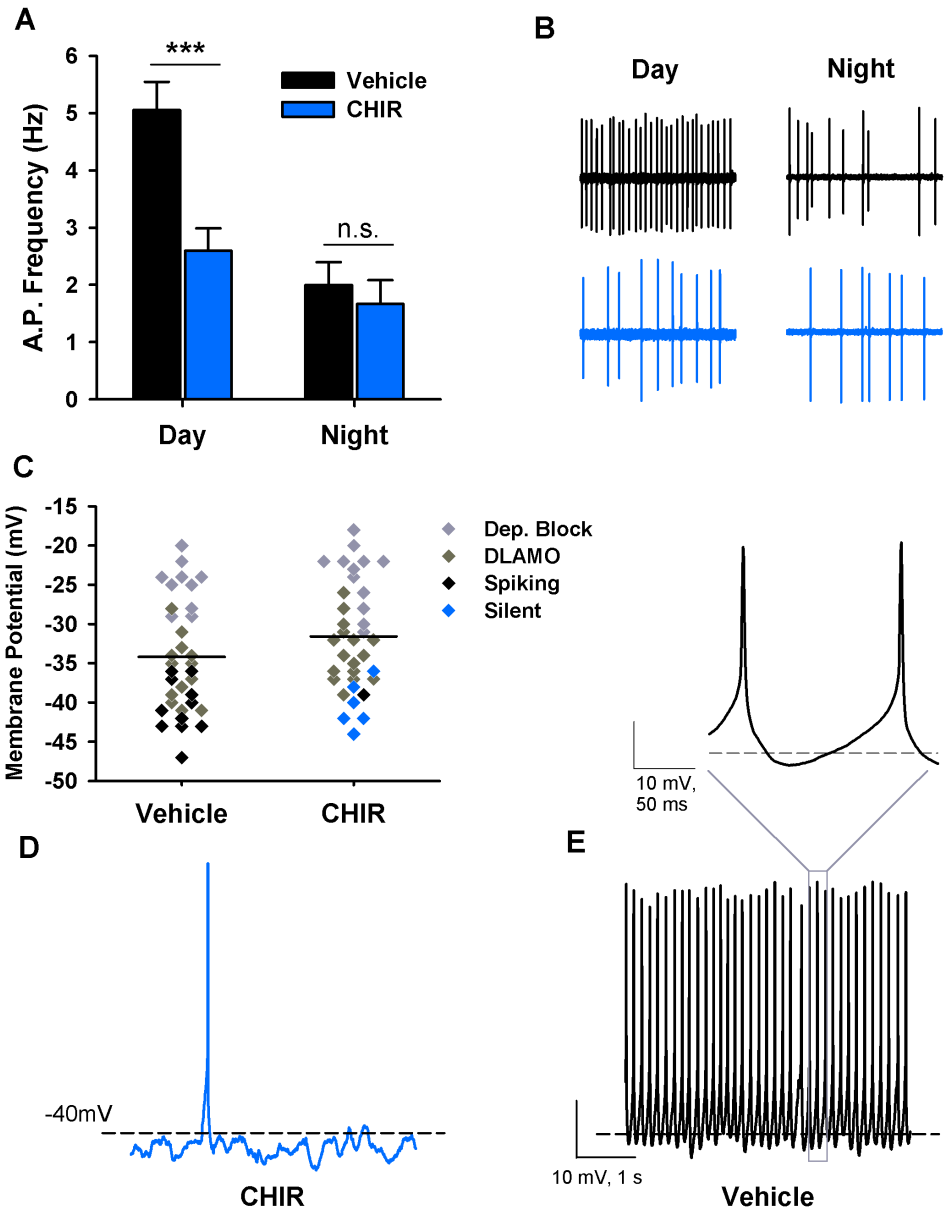

Figure 5.1: GSK3 inhibition suppresses spontaneous neuronal activity during the day. (A) Spontaneous action potential frequencies (mean ± SEM) from 2 min loose-patch recordings of neurons treated with Vehicle (0.002% DMSO) or CHIR during the day (ZT 4-8) or early-night (ZT 14-18). Two-way ANOVA; treatment × time interaction, $F_{(1,146)}$ = 5.772; n = 33-41 cells, 3-4 slices per group). CHIR significantly suppressed SCN activity during the day (*** $p < 0.001$) but not the night (n.s. $p = 0.6$). (B) Representative cell-attached loose-patch traces (10 sec) from each group. (C) Dot plot of resting membrane potential (RMP) for individual SCN neurons. Line indicates mean for each group. There was no difference in RMP between groups (independent samples t-test; $t_{(67)}$ = -1.521; $p > 0.05$; 5-6 slices per group. (D-E) Representative current clamp traces (5 sec) of SCN neurons treated with (D) CHIR or (E) vehicle during the mid-day (ZT 4-8). Inset shows zoomed in 200 ms of trace in box to show depolarizing ramp between action potentials in control cells.

low-amplitude membrane oscillations (DLAMOs), or exhibiting depolarization block. In spontaneously spiking neurons, action potentials are separated (or generated) by smooth depolarizing ramps to threshold (Fig. 5.1E). In contrast, when GSK3 was inhibited, cells within this same voltage range exhibited no spontaneous activity (Fig. 5.1D). Interestingly, a subset of cells continued to exhibit calcium-driven low amplitude membrane potential oscillations in the presence of CHIR (similar to tetrodoxin in [57, 102]), and the frequency of these oscillations was not different from vehicle treated cells, suggesting that GSK3 inhibition may modulate SCN excitability through suppression of a TTX-sensitive, voltage-gated sodium current. Because the persistent sodium current has been shown to provide at least part of the excitatory drive to action potential (AP) threshold, which appeared to be diminished in CHIR treated cells, we consider GSK3's effect on the persistent sodium current.

5.2.2 GSK3 inhibition suppresses a persistent sodium current specifically during the day

Recent work has implicated GSK3 in regulating the expression of NaV1.6 channels [123, 113], which are thought to be one of the major sources of a slowly-inactivating, or persistent, sodium current or I_{NaP} [35]. Although small in magnitude, I_{NaP} contributes to excitation of repetitively firing neurons by augmenting small depolarizations during the interspike interval [57]. In SCN cells, I_{NaP} provides the excitatory drive toward threshold [57], and silencing I_{NaP} suppresses action potential firing in SCN cells [65]. Therefore, we next examined the effect of GSK3 inhibition on I_{NaP} by measuring the current response to a slow (59 mV/s), depolarizing voltage ramp from -100 mV to 10 mV [101] before and after treatment with the selective persistent sodium channel blocker riluzole.

The voltage ramp elicited an inward current in vehicle-treated cells at the range of I_{NaP} activation, starting at -52.4 $\pm$ 1.1 mV and peaking at -26.8 $\pm$ 0.7 mV. During the day, the magnitude of peak I_{NaP} was significantly reduced in CHIR-treated cells (-10.8 $\pm$ 2.4 pA)

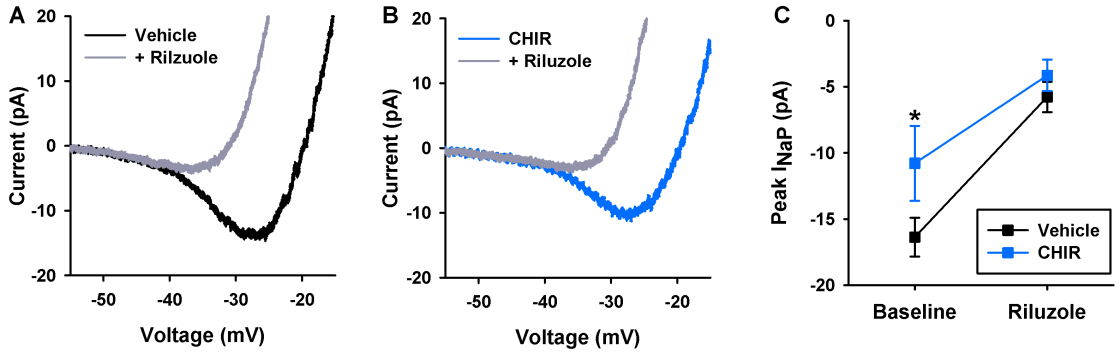

Figure 5.2: GSK3 inhibition during the day suppresses I_{NaP}. (A-B) Average normalized response to slow depolarizing voltage ramp (-100 to +10 mV; 59 mV/s) from SCN cells treated with (A) vehicle (DMSO, 0.002%) or (B) GSK3 inhibitor (CHIR, 1μM) at baseline (black/blue) and after 3-min treatment with persistent sodium current blocker, riluzole (20 μM, gray). (C) Peak inward current (mean $\pm$ SEM) from cells in A-B at baseline and after riluzole treatment. Recordings made between ZT 4-8. (two-way, repeated measures ANOVA; Treatment $\times$ Riluzole interaction, $F_{(1,31)}$ = 5.455, $p < 0.05$; n = 13-20 cells, 4 slices per group). CHIR-treated cells had significantly reduced inward current at baseline (* $p < 0.05$). This difference was lost after blockade of I_{NaP} with riluzole ($p > 0.05$).

compared to vehicle-treated controls at baseline (-16.4 $\pm$ 1.5 pA; $p < 0.05$; Fig. 5.2A, B). Application of riluzole (20 μM, 3-min) significantly suppressed the amount of inward current (CHIR, -4.1 $\pm$ 1.2 pA; vehicle, -5.8 $\pm$ 1.1 pA; $p < 0.001$) and eliminated the difference between CHIR- and vehicle-treated cells (Fig. 5.2C). At night, CHIR did not suppress baseline I_{NaP} (-11.7 $\pm$ 1.6 pA) compared to vehicle-treated controls (-11.2 $\pm$ 1.2 pA). These results suggest that GSK3 inhibition decreases I_{NaP} in day-phased SCN neurons and that this current is driven at least in part by GSK3 activation. Because circadian regulation of GSK3 inactivation increases throughout the night [16] when SCN cells are mostly quiescent, GSK3 regulation of I_{NaP} provides a previously unexplored mechanism underlying the daily rhythms in SCN excitability.

5.2.3 I_{NaP} is regulated by time-of-day and activation of GSK3

Complementary to the present results that GSK3 inhibition suppresses SCN activity during the day but not the night, we have recently reported that chronic GSK3 activation

increased neuronal firing at night, but not the day [100]. To determine if chronic GSK3 activation enhances I_{NaP} in SCN neurons, we measured I_{NaP} currents from wild-type mice and transgenic mice with constitutive GSK3 activation (i.e., GSK3-KI mice) due to serine-alanine substitutions at the two inhibitory phosphorylation sites for GSK3α and GSK3β (S21 and S9, respectively)[81]. Although previous reports have suggested that I_{NaP} does not exhibit a day/night difference in the SCN based on gene expression [99, 25], until now, no study has examined I_{NaP} isolated current at both times of the day.

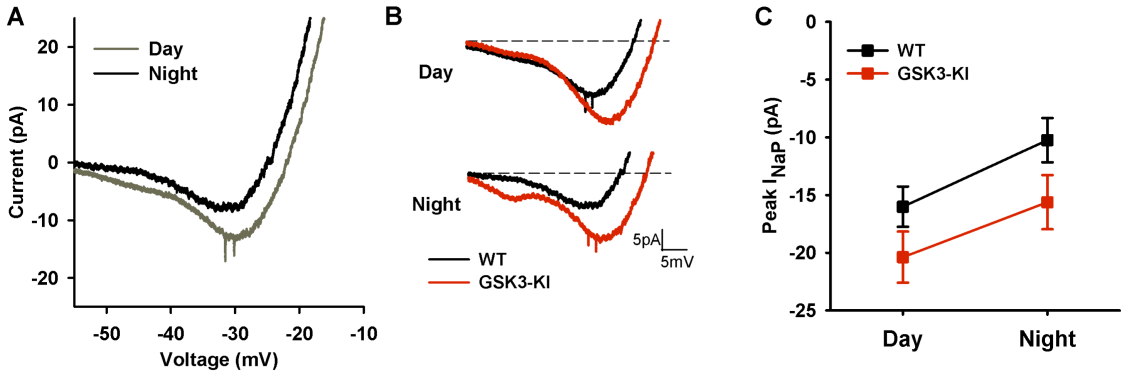

Figure 5.3: I_{NaP} is enhanced during the day and in GSK3-KI cells. (A) Average normalized response to slow depolarizing voltage ramp (-100 to +10 mV; 59 mV/s) from SCN cells from WT during the day (gray) or night (black) (n = 16-29 cells, 3-4 slices per group). (B) Average normalized responses to voltage ramp from WT (black) or GSK3-KI (red) SCN cells during the day (top) or night (bottom). (C) Peak inward current (mean $\pm$ SEM) from cells in A-B. Two-way ANOVA revealed main effects of time [$F_{(1,83)}$ = 6.473, $p < 0.05$] and genotype [$F_{(1,83)}$ = 5.551, $p < 0.05$] with no significant interaction.

We first examined whether there was a day/night difference in I_{NaP} in WT cells alone and found a significant increase in day-phase I_{NaP} (-16.01 $\pm$ 1.74 pA) compared to night (-10.25 $\pm$ 1.92 pA; $p < 0.05$, Fig. 5.3A). Further, I_{NaP} was enhanced in GSK3-KI cells compared to WT cells (main effect for genotype, $p < 0.05$; Fig. 5.3B). Surprisingly, the effect of chronic GSK3 activation was independent of time of day as both genotypes exhibited a day-night difference in I_{NaP} magnitude (main effect for Time, $p < 0.05$; Fig. 5.3C). Follow-up recordings from WT and GSK3-KI cells at night in the presence of $CdCl_2$ (0.1mM) and TEA (10mM) yielded similar results, suggesting that enhanced inward cur-

rent was not driven by calcium or potassium currents.

5.2.4 Mathematical model predicts GSK3 effect on I_{NaP} through modulation of channel conductance

To investigate how GSK3 affects neuronal excitability through the I_{NaP} current, we incorporated the current into our SCN neuron model [31, 30] developed in Chapter III. Full details of the model can be found in [30]. Here we focus on the incorporation of I_{NaP} into the electrophysiology component of the model. Briefly, we use a conductance-based model of SCN electrophysiology that simulates electrical activity with millisecond resolution based on sodium, potassium, calcium (L-type and non L-type), calcium-activated potassium, and leak (Na-leak and K-leak) currents. Here we modify the published model with the addition of the persistent sodium current, with dynamics fit using the voltage ramp data above as described in the methods section. We find that the dynamics of the persistent sodium current are consistent with a conductance-based model of the form $I_{NaP} = -g_{NaP}(V - E_{Na})$, with the activating gating variable p ranging between 0 and 1. Currents for all experimental conditions could be fit to this form by varying g_{NaP} (Fig. 5.4: g_{NaP} values are GSK3-KI day 2.27, GSK3-KI night 2.13, WT day 2.09, WT night 1.59, CHIR day 1.97, CHIR night 1.46). This suggests that the action of GSK3 on I_{NaP} is primarily through changing the maximal conductance of I_{NaP} channels, rather than affecting their dynamics.

We validated the model after the addition of the I_{NaP} current by performing voltage ramp simulations mimicking the analogous experiments presented in Fig. 5.2 and Fig. 5.3 (Fig. 5.4D-F). Simulated voltage ramps with and without I_{NaP} match the magnitudes of the inward currents seen experimentally in each condition: with simulated application of CHIR (Fig. 5.4D), wildtype (Fig. 5.4E), and with simulated constitutively active GSK3 (Fig. 5.4F), where each condition is reproduced simply by tuning the maximal conductance of the I_{NaP} current (g_{NaP}).

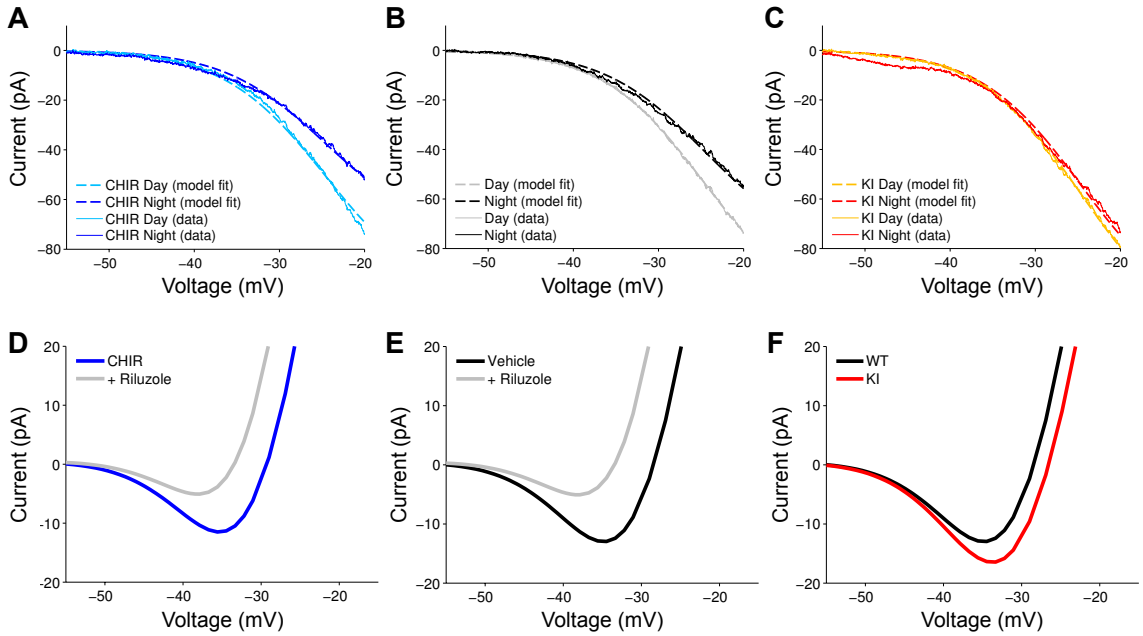

Figure 5.4: Fitting of I_{NaP} and simulation of voltage ramps in wildtype and GSK3 altered conditions at day and night. Voltage ramps in (A) GSK3 inhibited, (B) wildtype, and (C) constitutively active GSK3-KI cells at day and night are used to fit the I_{NaP} current. Data (solid lines) and model fits (dashed lines) are shown for each experimental condition. All curves are fit with the equation $g_{NaP}\frac{1}{(1+\exp(-(V+25)/7.4))^{1.5}}$, with g_{NaP} varied between experimental conditions (g_{NaP}: GSK3-KI day 2.27, GSK3-KI night 2.13, WT day 2.09, WT night 1.59, CHIR day 1.97, CHIR night 1.46). Incorporating the fit current into the model and simulating the voltage ramps reproduces experimental results. (D-E) Simulation of the experimental protocols shown in figure 5.2A-B reproduces the I_{NaP} seen experimentally. In particular, in day-time SCN cells, (D) reduction of g_{NaP} to CHIR levels reduces peak I_{NaP} relative to (E) wildtype. Simulated application of riluzole ($g_{NaP} = 0$) further decreases I_{NaP}(F) Increased g_{NaP} to GSK3-KI day-time levels increases I_{NaP}even beyond wildtype levels as in 5.3B.

5.2.5 I_{NaP} mediates GSK3-induced excitability at night

Using the model, we directly tune the strength of the I_{NaP} current, mimicking the transition from low GSK3 activity (e.g. with CHIR), to wildtype, to high GSK3 activity (e.g. GSK3-KI), and analyze how this changes neuronal excitability. We simulate 1024 GABA and VIP coupled SCN neurons and find that the wildtype cells show a variety of firing activities with circadian variation, as seen experimentally. As GSK3 activity is increased to the level of the GSK3-KI, the model predicts that many of the cells which are normally quiescent at night switch and begin spiking. Voltage for a sample quiescent wildtype neu-

ron at night sits around the resting membrane potential denoted by a dashed line (Fig. 5.5A). The identical simulated neuron with g_{NaP} increased to GSK3-KI levels on the other hand shows action potentials (Fig. 5.5B). At this circadian phase, roughly equal numbers of cells in the wildtype network are quiescent, but in the GSK3-KI, the majority of neurons spike (Fig. 5.5C). Since all parameters other than g_{NaP} are identical between the simulations, the change in activity must be due to the persistent sodium current.

To verify whether the increased excitability of GSK3-KI neurons at night seen experimentally [100] is also due to enhanced $\mathrm{I_{NaP}}$ current, we examined the spontaneous firing rate of WT and GSK3-KI SCN neurons following application of riluzole (10 μM). Consistent with the previous study [100], vehicle-treated GSK3-KI cells had a significantly increased spontaneous firing rate compared to WT neurons ($p < 0.001$; Fig. 5.5D-E). This hyper-excitability was rescued in riluzole-treated GSK3-KI cells which did not differ from either WT group ($p < 0.001$). Since the majority of SCN neurons are relatively quiescent during the night, we also quantified the number of spiking versus non-spiking cells from WT and GSK3-KI mice in riluzole- and vehicle-treated conditions and found significant differences between groups ($p < 0.001$; Fig. 5.5F). While ~one-third of WT neurons were non-spiking, almost all of the GSK3-KI neurons were silent ($p < 0.001$), as predicted by the model. Moreover, the ratio of spiking to non-spiking cells was restored to WT levels upon riluzole treatment, while riluzole had no effect on WT neurons at night ($p > 0.05$; Fig. 5.5F). Taken together, these results suggest that active GSK3 promotes neuronal excitability in an $\mathrm{I_{NaP}}$-dependent manner.

5.2.6 Model predicts GSK3 promotes excitability by suppressing the AP after-hyperpolarization

Using the model, we are able to investigate how $\mathrm{I_{NaP}}$ affects neuronal excitability. Unexpectedly, in firing neurons, the model predicts that increasing $\mathrm{I_{NaP}}$ causes an increase in firing rate with minimal change to the resting membrane potential of the cells. Often

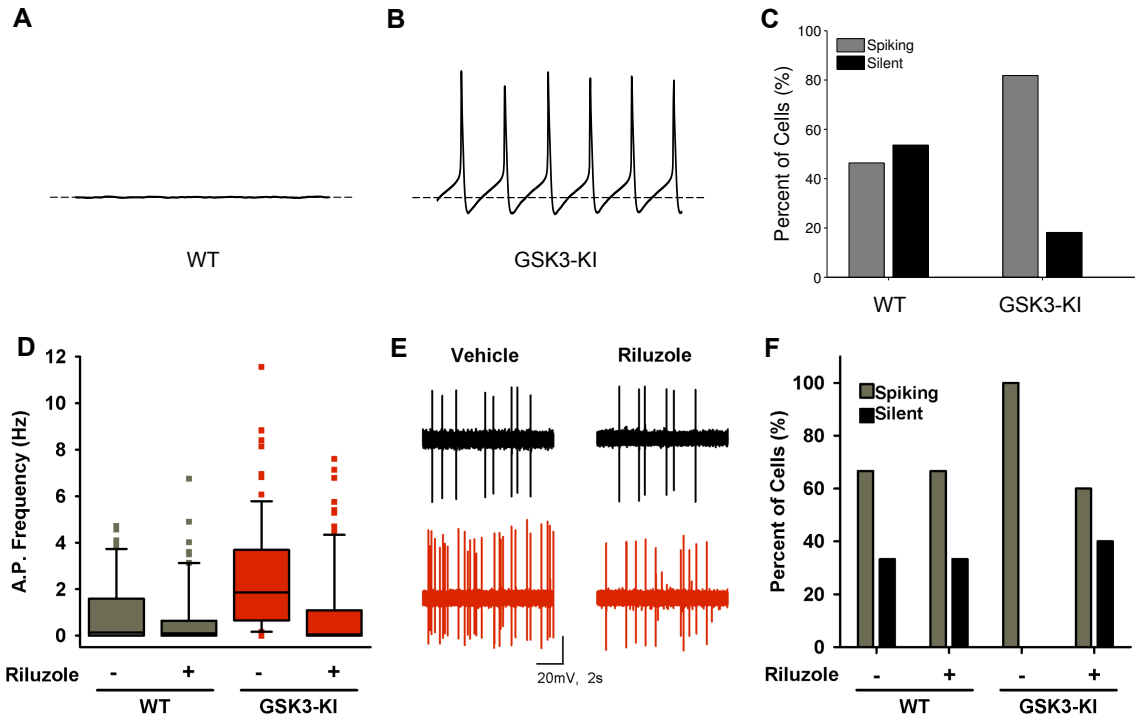

Figure 5.5: Increased I_{NaP} in constitutively active GSK3-KI increases neuronal firing. (A-B) Simulation of the SCN neuronal network model shows that with all other parameters held fixed, increasing g_{NaP} from WT to GSK3-KI levels is sufficient to switch night-time (A) quiescent neurons (B) to spiking. (C) The fraction of spiking neurons greatly increases in the model GSK3-KI network. (D) Box plot of night-time spontaneous action potential frequencies of SCN neurons from WT or GSK3-KI mice treated with vehicle or riluzole (10 μM) shows a greater firing rate in the GSK3-KI cells (Kruskal-Wallis test, $H_{(3)} = 58.202$, asymptotic significance, ***$p < 0.001$). Firing rate is reduced to equal levels in both genotypes by the application of the I_{NaP} blocker riluzole, confirming that this effect is I_{NaP} mediated. (E) Representative cell-attached loose-patch traces (10 sec) from WT (black) and GSK3-KI (red) groups. (F) Quantification of silent versus non-silent cells for each group in D-E (n = 29-35 cells, 2-3 slices per group). Three-way log-linear analysis revealed a significant three-way interaction ($\chi^2_{(1)} = 25.852$, $p < 0.001$). Follow-up chi-squared tests revealed that GSK3-KI cells were significantly more likely to be spiking than WT vehicle-treated cells ($\chi^2_{(1)} = 32.428$, $p < 0.001$), as predicted by the model. Blocking I_{NaP} with riluzole increased the proportion of silent cells in GSK3-KI slices ($\chi^2_{(1)} = 44.735$, $p < 0.001$) up to that of WT levels ($\chi^2_{(1)} = 0.430$, $p > 0.05$), confirming that the effect is I_{NaP} mediated.

increases in excitability are due to increased RMP, but I_{NaP} seems to act through a different mechanism. This model prediction is consistent with what is seen experimentally, as CHIR application causes many spiking neurons to become silent with no significant change to their RMP (Fig. 5.1C). Similarly, the majority of neurons in the GSK3-KI show no change in RMP (Fig. 5.6A). The only exception is the subset of neurons in depolarization block,

but the model predicts this effect as well since the voltage-gated I_{NaP} channels are held open at that high of a voltage, leading to an increase in RMP (Fig. 5.6B-C).

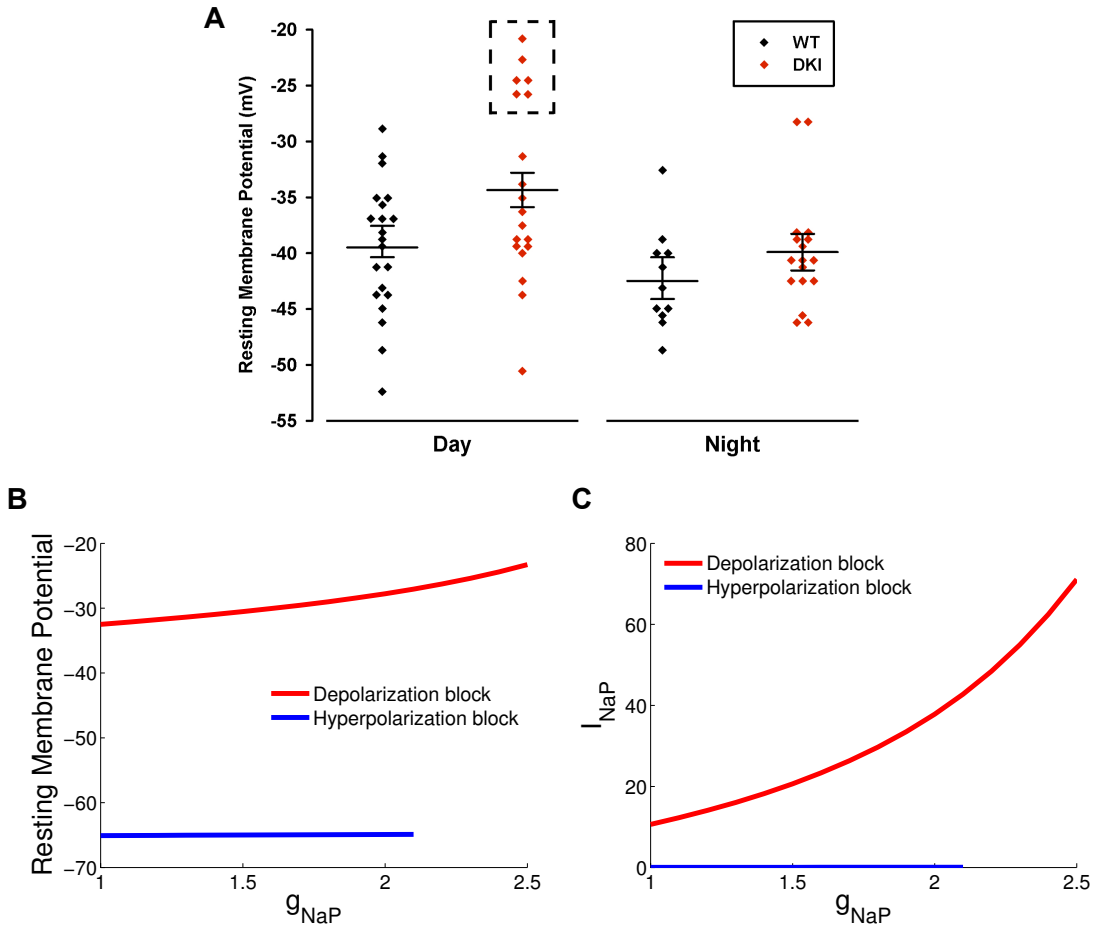

Figure 5.6: I_{NaP} raises the RMP of neurons in the depolarization block state. (A) Dot plot of RMP for individual neurons recorded from WT (black) and GSK3-KI (red) SCN slices during the day or the night. Lines represent means ± SEM. Neurons outlined by the black dashed box were in depolarization block. With the exception of these neurons, no significant increase in RMP was seen in the GSK3-KI over WT cells. (B) Model prediction of the relationship between RMP and g_{NaP} for cells in depolarization (red) and hyperpolarization (blue) block. (C) Cells with hyperpolarized RMPs do not show any change in RMP as the maximal conductance, g_{NaP}, is changed because the voltage-gated I_{NaP} channels are almost entirely closed at hyperpolarized voltages. The voltage-gated I_{NaP} channels are open at depolarized membrane voltages, however, leading to an increase in depolarization block RMP as g_{NaP} is increased.

Further analysis of our model simulations reveals that the increased excitation through I_{NaP} is instead caused by suppression of the AP after-hyperpolarization (AHP). Both at day and at night, increasing the magnitude of I_{NaP} by increasing its maximal conductance, g_{NaP},

from CHIR to WT to GSK3-KI levels causes the minimum voltage attained after an action potential to become less hyperpolarized, while the RMP is unchanged (Fig. 5.7A). Thus the magnitude of the AHP diminishes, allowing cells to fire more rapidly (Fig. 5.7B).

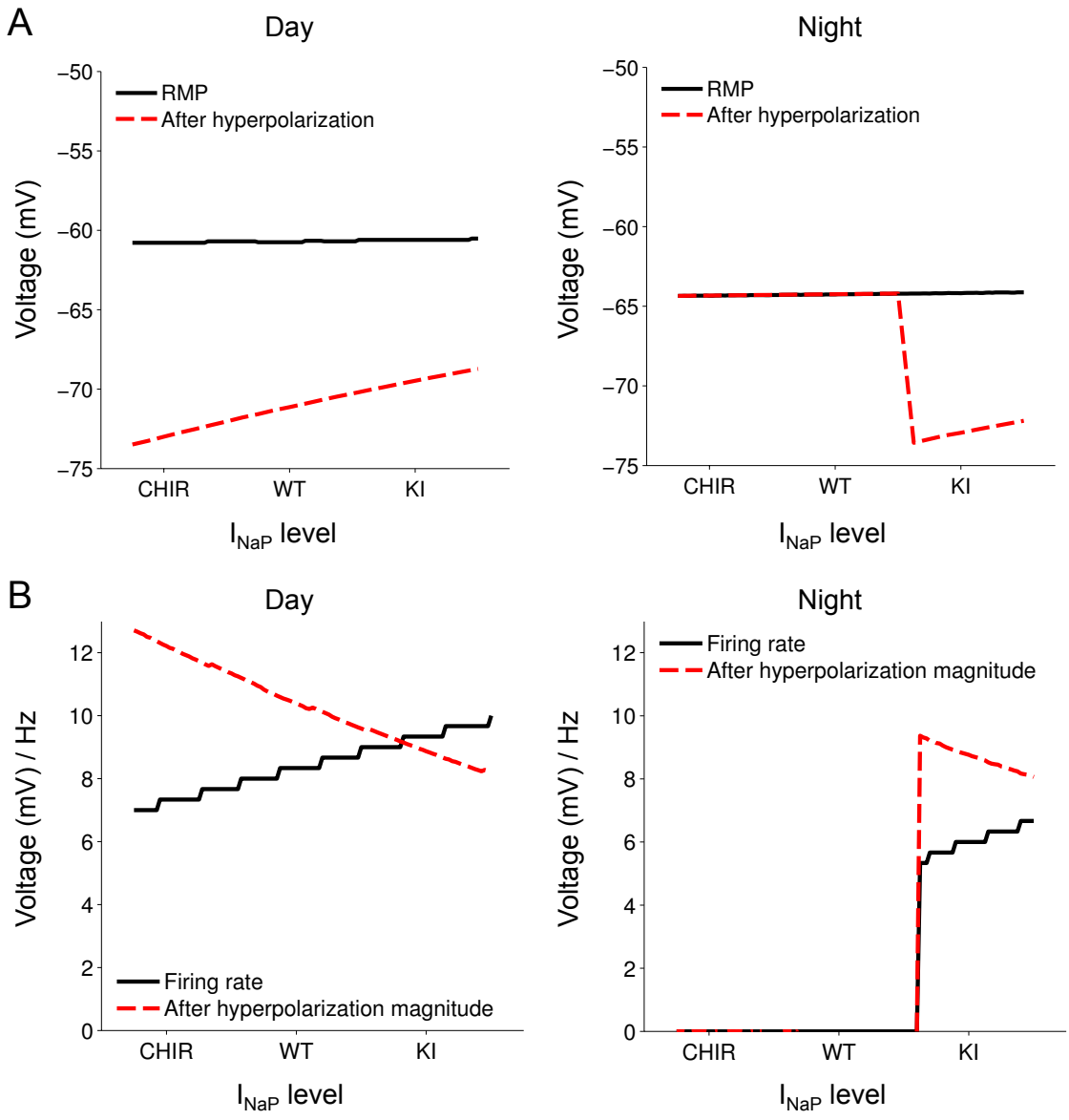

Figure 5.7: Increasing I_{NaP} decreases the magnitude of the AP after-hyperpolarization causing faster firing. (A) Both at day (left) and at night (right), increasing I_{NaP} in spiking neurons causes the neuron to reach a less hyperpolarized minimum voltage (red) following an action potential, while leaving the resting membrane potential (black) unchanged. (B) The magnitude of the AHP (RMP - post AP minimum; red) is therefore reduced, leading to a faster firing rate (black). CHIR and WT neurons at night are not predicted to fire, and therefore have a firing rate of 0 and RMP equal to their minimum value.

As predicted by the model and previously noted, current clamp traces of SCN neurons revealed significantly greater spontaneous action potential frequency in neurons from GSK3-KI mice compared to WT mice (Fig. 5.5D). Action potential waveforms of current clamp traces from both genotypes during the day and night revealed a significant decrease in the AHP, particularly during the night, such that the day-night difference in AHP is diminished in GSK3-KI neurons (Fig. 5.8). Moreover, the after-hyperpolarization of all spontaneously spiking cells were significantly negatively correlated with I_{NaP} peak current, such that the larger the I_{NaP} magnitude, the smaller the after-hyperpolarization.

The model predicts that the degree of after-hyperpolarization following an action potential depends on the balance of the I_{NaP} (positive-inward) and I_{KCa} (positive-outward) currents. By plotting each of the currents that contribute to changes in membrane voltage, it is apparent that most of the currents involved in generating the action potential shut off rapidly (Fig. 5.9A). Only I_{NaP} and I_{KCa} persist through the interspike interval, setting the AHP magnitude and the depolarizing ramp back toward threshold. Increasing I_{NaP} or decreasing I_{KCa} causes a decrease in the AHP magnitude and consequently speeds up the firing rate. Conversely, decreasing I_{NaP} or increasing I_{KCa} increases the AHP magnitude and slows firing (Fig. 5.9B).

5.3 Discussion

The varied firing activities displayed by SCN neurons in a time-of-day dependent manner are thought to be essential for sending timing information to other parts of the brain. Several studies have shown that SCN firing is controlled by the molecular clock, but the mechanism for this is largely still unknown. Past work has suggested that certain ionic channels may be transcriptionally regulated, but this is an inefficient form of regulation both in terms of metabolic cost and the slow timescales of transcription and translation.

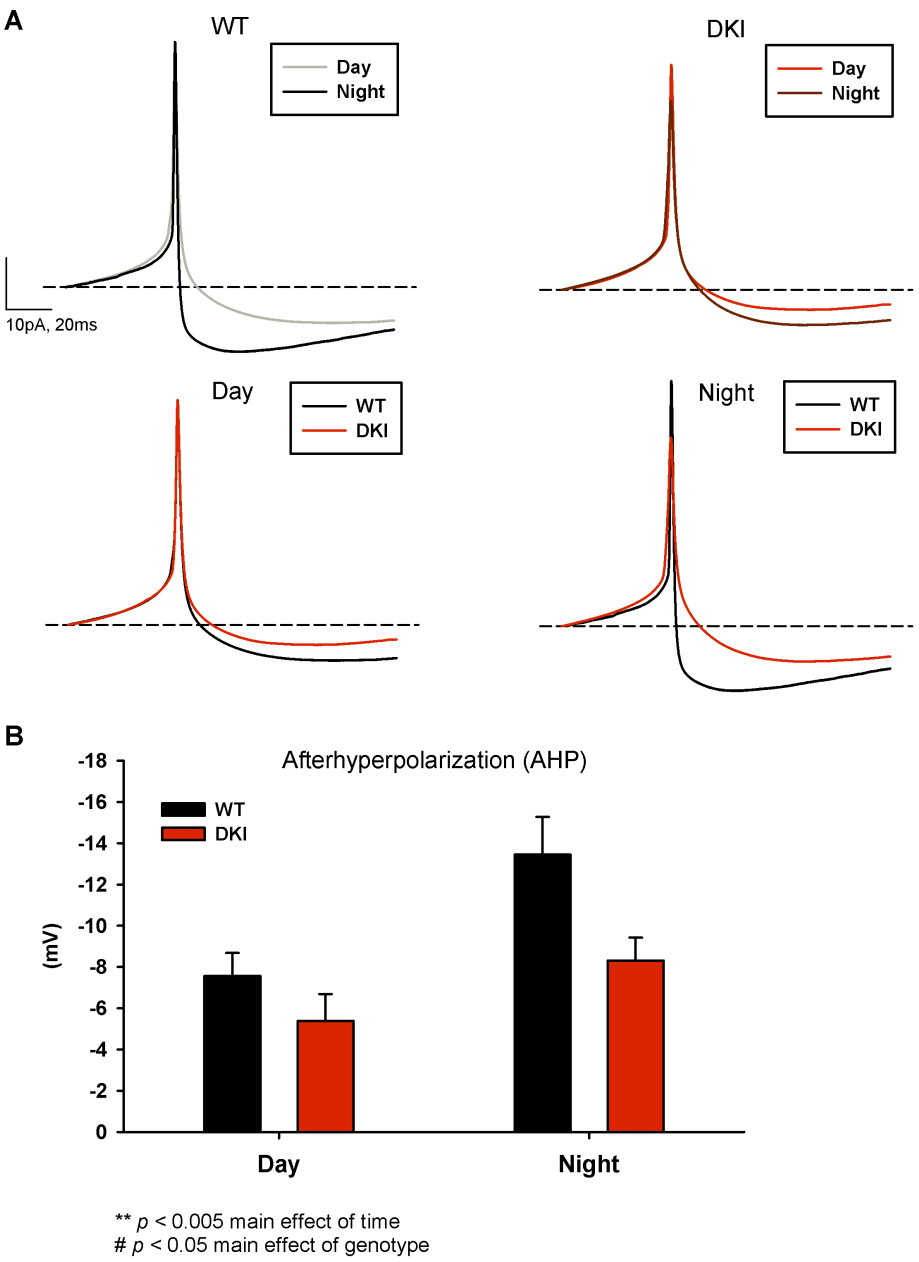

Figure 5.8: Day-time WT and all GSK3-KI neurons show reduced after-hyperpolarization. (A) Average action potential waveforms from WT and GSK3-KI SCN neurons recorded during the day and night. For visualization, baseline potential was adjusted to -40mV for all waveforms before averaging. Day-time neurons show decreased AHP relative to night-time neurons. GSK3-KI neurons show AHPs similar to the WT day-time cell at all times. (B) Quantification of the peak AHP magnitudes from panel A shows significant differences between day and night WT neurons. Little difference is seen in the GSK3-KI neurons.

Here we propose a new mechanism: control of membrane excitability through the clock-controlled kinase GSK3.

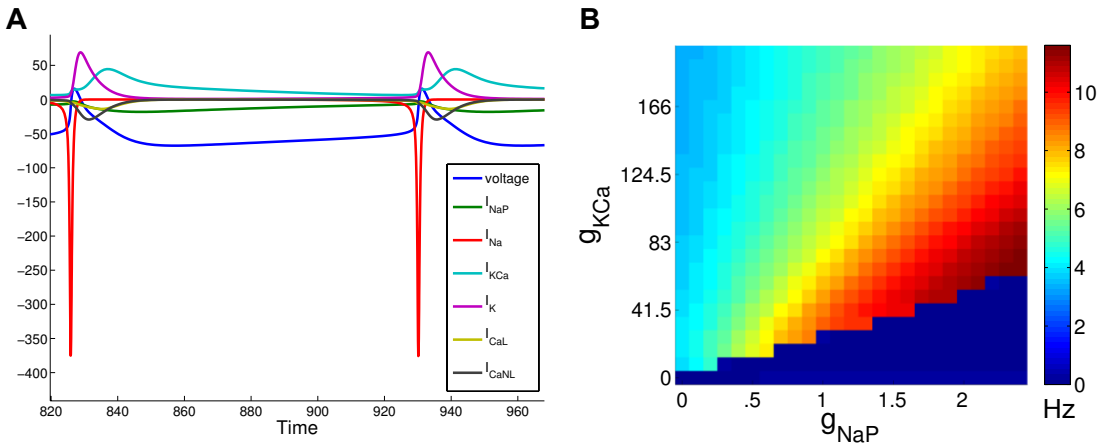

Figure 5.9: I_{NaP} and I_{KCa} balance determines AHP and firing rate. (A) Plot of the currents involved in repetitive firing. Membrane voltage (blue) peaks twice marking two action potentials. While many currents are involved in generating the action potentials, only I_{NaP} (green) and I_{KCa} (teal) evolve on a slow timescale longer than the duration of the action potential. I_{NaP} depolarizes the neuron, promoting the firing of the next action potential, and I_{KCa} hyperpolarizes the neuron, delaying the firing of the next action potential. The balance of these two currents sets the AHP and the ramp back toward threshold, thereby determining the firing rate of the cell. (B) Changing the maximal conductances g_{NaP} and g_{KCa} modulates the firing rate of the cell (colorbar on the right in Hz).

Regulation of ion channels through phosphorylation has previously been proposed, for example by the cAMP-dependent protein kinase. However, it has never been reported in the SCN. This study shows experimental evidence for a role of the kinase GSK3 in regulating a persistent sodium current, I_{NaP}, which has strong effects on neuronal electrical activity. This current promotes excitability, and can both cause silent neurons to spike as well as increase the firing rate of already spiking cells. Through a combination of modeling and experiments, we show that the balance between I_{NaP} and I_{KCa} controls the magnitude of the after-hyperpolarization following an action potential, and the depolarizing ramp toward firing. By increasing the strength of the I_{NaP} current, GSK3 increases the firing rate of the cell.

Since this change in excitation occurs without changing the cellular resting membrane potential, very little change in intracellular calcium concentration is seen. As previously

shown in Chapter III, the model predicts that without a significant change in RMP and consequent increase in intracellular calcium, modulation of firing rate can occur without affecting transcription or shifting the molecular clock. Thus GSK3 activation of I_{NaP} could be one mechanism by which a cell can tune its firing state, and rate, to reflect the phase of its molecular clock rhythm without shifting it. While more work is necessary to explore the biophysical mechanism by which GSK3 activates I_{NaP}, this work suggests a promising new motif in which a kinase can directly regulate electrical activity acutely, and without transcriptional cost. Because of its efficiency, this is a motif likely to be found in other brain regions as well.

5.4 Methods

5.4.1 Model fitting of I_{NaP}

The voltage dependence of I_{NaP} was determined using the current response to a 59 mV/s depolarizing voltage ramp, from -100 mV to 10 mV shown in figures 5.2 and 5.3. These protocols as well as all other electrophysiological recordings in this chapter were performed by Jodi Paul in the lab of Karen Gamble. Current values were fit for voltages between -65 mV and -20 mV, since cellular voltages are usually in this range. The least current was seen in night phase cells after treatment with riluzole, a selective persistent sodium channel blocker. This was taken as the baseline, and subtracted away from current response curves for day and night phase cells in three experimental conditions: wildtype, after treatment with the GSK3 blocker CHIR, and in slices from GSK3-KI animals, which have constitutively active GSK3. The dynamics of the I_{NaP} current were consistent with a conductance-based model of the form $I_{NaP} = -g_{NaP}(V - E_{Na})$, with the activating gating variable p ranging between 0 and 1. Fitting the currents, we found that p should satisfy the

standard Hodgkin-Huxley style gating variable equation

$$\frac{dp}{dt} = \frac{p_\infty(V) - p}{\tau_p} \quad \text{with} \quad p_\infty(V) = \frac{1}{(1 + \exp(-(V + 25)/7.4))^{1.5}}$$

and τ_p=100. Currents for all experimental conditions could be fit to this form by varying g_{NaP} (Fig. 5.4: g_{NaP} values are GSK3-KI day 2.27, GSK3-KI night 2.13, WT day 2.09, WT night 1.59, CHIR day 1.97, CHIR night 1.46,). This suggests that the action of GSK3 on I_{NaP} is primarily through changing the maximal conductance of I_{NaP} channels, rather than affecting their dynamics.

5.4.2 Incorporation of I_{NaP} into the SCN model

The original SCN electrophysiology model [31] included circadian variation in two conductances (g_{KCa} and $g_{\text{K-leak}}$). We additionally incorporate GSK3 control of the I_{NaP} amplitude through the function $S = 21.0(gto - 1.66)$, where gto is the molecular clock variable corresponding to GSK3 activity [60]. The maximal I_{NaP} conductance is then given by:

$$\text{WT: } g_{\text{NaP}} = 1.59 + 0.5/(1.0 + \exp(-S))$$

$$\text{CHIR: } g_{\text{NaP}} = 1.46 + 0.51/(1.0 + \exp(-S))$$

$$\text{GSK3-KI: } g_{\text{NaP}} = 2.13 + 0.14/(1.0 + exp(-S))$$

according to the values for day and night in each experimental condition, as in Fig. 5.4. This reproduces the day-night difference in I_{NaP} amplitude described above. To compensate for the addition of this current, we reduce the circadian drive of g_{KCa} and $g_{\text{K-leak}}$ to 60% of its original value (all parameters as in [30] and Chapter III except $R = 6.81 \cdot clk(G - 0.25)$). With this small modification, the model reproduces the circadian variation in electrical activity seen experimentally [14, 31].

CHAPTER VI

Conclusion

Many biological systems function based on two essential motifs: network interactions between cells and integration across timescales. Both of these are ubiquitous in the study of coupled biological oscillators. Rhythm-generating tissues such as the heart and brain require communication and coordination between cellular oscillators across timescales in order to generate tissue-level rhythms. This makes them very difficult to study experimentally, as laboratory techniques are often only good at analyzing behaviors either at single cell or tissue level resolution, but not both, and generally only on a single timescale.

Mathematical modeling can provide invaluable insight in order to explain this complexity. In particular, the development of multiscale models has the potential to integrate all of the experimental results from specific temporal and spatial scales into a coherent picture of tissue level function. Models also provide a powerful tool for studying intercellular signaling, an essential component of network activity. In this dissertation, we develop a model for the mammalian circadian clock, and show how it can be used to study the essential role of signaling on two very different timescales in order to tune the level of synchrony displayed in the network and generate a coherent tissue-level output.

First, we focus on the slow timescale and develop a multicellular model of the circadian clock from a detailed model of single-cell dynamics. With this model, we show how

intercellular signaling can create robust, tissue-level rhythms out of weak cellular oscillators. By fitting the coupling for the model to biological data measured from the SCN tissue, we find that when the coupling is removed, the model predicts that individual cells are bistable. This prediction is consistent with experimental data [135], as well as previous modeling work which showed that the proper balance of transcriptional activators and repressors is necessary for generating robust rhythms [60]. Here we extend that story by explaining how the network input can act as a transcriptional activator so that the cellular oscillators will show robust rhythms only when they are functioning as part of the network.

Next, we extend the model to include the much faster timescale of neuronal electrical activity. This requires using new computational techniques for simulating the fast dynamics efficiently. Since the fast dynamics are stiff, an implicit method is necessary for numerically solving the ODEs. Implicit methods often take longer to solve, but by using a leapfrogging technique which takes advantage of the structure of the ODEs, we are able to solve the implicit update step explicitly. This method is still second order, and as accurate as Matlab's ODE15s even with a relatively large, fixed time step. By nesting simulation of the fast timescale within each time step of the slow biochemical model, we can simulate dynamics on both scales for a large network of coupled neurons.

With this multiscale model, we show how a single neurotransmitter can signal on each of the two timescales with very different effects on network behavior. The model led to the novel prediction of a tonic GABA signal produced by a fraction of hyperexcited cells in the network, which affects molecular timekeeping on the slow timescale. The tonic signal is separate from the phasic GABA signal, which modulates the firing rate and output signal of cells in the network without affecting their internal timekeeping. Currently, it is impossible to measure GABA output precisely enough to confirm this prediction, but several experimentalists have reported that they are working on related problems and may

be able to test this prediction soon.

Finally, we use the detailed, multiscale network model to test two different attributes of the mammalian circadian clock: seasonal encoding of daylength and the regulation of electrical firing activities. Both of these functions are integral to the workings of the clock within an organism. Using the model we provide insight into the role of intra and intercellular signaling in controlling tissue-level behavior and output to the rest of the brain.

While the methods developed here have focused on a specific problem of circadian timekeeping, this framework could be applied to many other biological systems. The mathematical study and modeling of heterogeneous coupled oscillators is relevant for many other organs that also rely on the proper coordination of cellular oscillators within a tissue for proper function. One common feature of each of these biological networks is that they are highly parallel, usually with many cells working in concert to perform an activity. This structure allows for efficient simulation on parallel architecture like GPUs, as discussed here.

The circadian system is an excellent model system because much is known about the components of the genetic and electrical activities of the individual neurons that make up the master circadian clock. Furthermore, the clock has clear, well defined inputs (such as light entrainment) and outputs (such as behavioral rhythms). It is therefore an excellent system for studying how information sent in to a brain circuit is processed and encoded in a coherent output signal. Toward this end, multiscale modeling provides a powerful tool for elucidating the black box in between: the integration of heterogeneous neuronal activity in the brain across spatial and temporal scales.

APPENDIX

APPENDIX A

Supplemental information for fitting and modeling multicellular clock model

A.1 Changes to the published Kim and Forger model

The original Kim and Forger model was extended to include a model of VIP signaling [60]. Changes to the model are as below.

A.1.1 Modified parameters from the original Kim and Forger model:

```
trPo = 10.3680 (transcription rate of Per1 from E-box activation)
trPt = 17.9416 (transcription rate of Per2 from E-box actication)
```

A.1.2 Additional parameters for the extended single-cell/network models

```
uv = 10.1630 (degradation rate of VIP)
Vt = 1.8783 (VPAC2R expression level)
vbin = 0.9341 (rate constant for VIP binding to VPAC2R)
unvbin = 1.1911 (rate constant for VIP unbinding from VPAC2R)
cvbin = 0.5582 (rate constant for CRY1/CRY2 binding to VPAC2R)
uncvbin = 6.2698 (rate constant for CRY1/CRY2 unbinding from VPAC2R)
vs = 24.0730 (production rate of cAMP when VPAC2R is bound by VIP
     and not inhibited by CRY, also activation rate of CREB by cAMP)
```

```
us = 1.2555 (clearance rate of cAMP and activated CREB)
sbin = 1.6161 (rate constant for activated CREB binding to CRE
     site on DNA)
unsbin = 3.9681 (rate constant for activated CREB unbinding from
     CRE site)
CtrPo = 14.5720 (transcription rate of Per1 from CRE activation)
CtrPt = 25.9390 (transcription rate of Per2 from CRE activation)
vpr = 1.1985 (VIP release rate)
vca = 1.2811 (rate constant for circadian increase in
     intracellular calcium)
uca = 0.6273 (rate constant for circadian clearance of calcium)
```

A.1.3 Additional variables for the extended single-cell/network models

```
vip = concentration of VIP present at the cells location, able to
     bind to VPAC2R
Vij = VPAC2R state:
     i = 0 VIP is unbound, i = 1 VIP is bound
     j = 0 no CRY bound, j = 1 CRY1 is bound, j = 2 CRY2 is bound
     (only CRY1 or CRY2 may bind at once)
cAMP = intracellular cAMP concentration
CREB = activated CREB in the cell
CRE = probability that the CRE site is activated
Ca = intracellular calcium concentration
```

A.1.4 Additional equations for the extended single-cell/network models

```
vip_dot = vpr*Ca-uv*vip-vbin*(V00+V01+V02)*vip+unvbin*(V10+V11+V12);
```

```
V10_dot = vbin*V00*vip-unvbin*V10
          - cvbin*V10*(x01000+x02000)+uncvbin*(V11+V12);
V11_dot = cvbin*V10*x01000-(unvbin+uncvbin)*V11+vbin*V01*vip;
V12_dot = cvbin*V10*x02000-(unvbin+uncvbin)*V12+vbin*V02*vip;
V01_dot = cvbin*V00*x01000-uncvbin*V01-vbin*V01*vip+unvbin*V11;
V02_dot = cvbin*V00*x02000-uncvbin*V02-vbin*V02*vip+unvbin*V12;
cAMP_dot = vs*V10-us*cAMP;
CREB_dot = .1*Ca + vs*cAMP-us*CREB;
CRE_dot = sbin*CREB*(1-CRE) - unsbin*CRE;
Ca_dot = vca*G-uca*Ca;
```

A.1.5 Modified equations from the original model:

```
MnPo_dot = trPo*G+CtrPo*CRE*G-tmc*MnPo-umPo*MnPo;
MnPt_dot = trPt*G+CtrPt*CRE*G-tmc*MnPt-umPt*MnPt;
x01000_dot = tlr*McRo-uro*x01000-ar*x01000*(x20000+x20100+x40000
     +x40100+x40200+x40300+x50000+x50100+x50200+x50300+x60000
     +x60100+x60200+x60300)+dr*(x21000+x21100+x41000+x41100
     +x41200+x41300+x51000+x51100+x51200+x51300+x61000+x61100
     +x61200+x61300)+(-cvbin*(V00+V10)*x01000+uncvbin*(V01+V11));
x02000_dot = tlr*McRt-urt*x02000-ar*x02000*(x20000+x20100+x40000
     +x40100+x40200+x40300+x50000+x50100+x50200+x50300+x60000
     +x60100+x60200+x60300)+dr*(x22000+x22100+x42000+x42100
     +x42200+x42300+x52000+x52100+x52200+x52300+x62000+x62100
     +x62200+x62300)+(-cvbin*(V00+V10)*x02000+uncvbin*(V02+V12));
```

A.2 Parameter estimation using GPUs

Parameter estimation of the new model including intercellular coupling was performed using simulated annealing as in the original Kim and Forger publication [60]. The cost function used had several terms:

1. Cost for time series: The core of the cost function compares simulated variables (x,y, and z, representing proteins, mRNA, calcium, and CRE as described below) to corresponding experimentally measured time series D.

$$\sum_{i,t} w_i \left(\frac{x_i(t) - \min(x_i)}{\max(x_i) - \min(x_i)} - D(x_i, t) \right)^2 + \sum_{j,t} w_j \left(\frac{y_j(t)}{\max(y_j)} - D(y_j, t) \right)^2 + \sum_{k,t} w_k (z_k(t) - D(z_k, t))^2$$

   In this equation: $x_i(t)$ ranges over PER1, PER2, CRY1, and CRY2 proteins for 1 cycle $y_i(t)$ ranges over CRE and calcium, each for 2 cycles $z_i(t)$ ranges over per1, per2, cry1, cry2, bmal1, reverb, and npas mRNAs, each for 2 cycles For each term, the weighting w normalizes the term by the number of time points compared.

   Additionally, the following costs are added:

2. Cost for relative protein abundances
   (a) If $\left(\frac{\max(PER1)}{\max(CRY1)} - 0.1\right)^2 > 0.05^2$ then add $400\left(\left(\frac{\max(PER1)}{\max(CRY1)} - 0.1\right)^2 - 0.05^2\right)$
   (b) If $\left(\frac{\max(PER2)}{\max(CRY1)} - 0.15\right)^2 > 0.05^2$ then add $4\left(\left(\frac{\max(PER2)}{\max(CRY1)} - 0.15\right)^2 - 0.05^2\right)$
   (c) Add $\left(\frac{\max(CRY2)}{\max(CRY1)} - 0.6\right)^2$
   (d) If $\left(\frac{\max(BMAL1)}{\max(CRY1)}\right) > 1$ then add $\left(\frac{\max(BMAL1)}{\max(CRY1)} - 1\right)^2$
   (e) Add $\left(\frac{57.6104}{\max(CRY1)} - 0.78\right)^2$

3. Cost for relative minimum and maximum levels

(a) Add $0.5\left(\frac{\min(BMAL1)}{\max(BMAL1)} - 0.5\right)^2$ (BMAL protein minimum should be ~50% of max)

(b) Add $0.5\left(\frac{\min(CRE)}{\max(CRE)} - 0.2\right)^2$ (CRE minimum should be ~20% of max)

(c) Add $0.5\left(\frac{\min(per1)}{\max(per1)} - 0.3\right)^2$ (Per1 mRNA minimum should be ~30% of max)

(d) Add $0.5\left(\frac{\min(cry1)}{\max(cry1)} - 0.4\right)^2$ (Cry1 mRNA minimum should be ~40% of max)

(e) Add $0.5\left(\frac{\min(bmal1)}{\max(bmal1)} - 0.6\right)^2$ (Bmal1 mRNA minimum should be ~60% of max)

4. Cost for mRNA peak times

(a) Add $0.5\left(\frac{x(\text{desired peaktime})}{\max(x)} - 1\right)^2$

(b) Add $\left(\frac{y(\text{desired peaktime})}{\max(y)} - 1\right)^2$ for $x =$ per1, per2, and npas mRNAs, and $y =$ cry1, bmal1, reverb mRNAs.

5. Cost for protein, calcium, and CRE peak times

(a) Add $20\left(\frac{x(\text{desired peaktime})}{\max(x)} - 1\right)^2$

for $x =$ PER1, PER2, and CRY2 proteins, as well as calcium and CRE

BIBLIOGRAPHY

BIBLIOGRAPHY

[1] Ute Abraham, Adrián E Granada, Pål O Westermark, Markus Heine, Achim Kramer, and Hanspeter Herzel. Coupling governs entrainment range of circadian clocks. *Molecular systems biology*, 6(438):438, November 2010.

[2] Peter Achermann and Hanspeter Kunz. Modeling Circadian Rhythm Generation in the Suprachiasmatic Nucleus with Locally Coupled Self-Sustained Oscillators: Phase Shifts and Phase Response Curves. *Journal of Biological Rhythms*, 14(6):460–468, December 1999.

[3] Javier Alamilla, Azucena Perez-Burgos, Daniel Quinto, and Raúl Aguilar-Roblero. Circadian modulation of the cl(-) equilibrium potential in the rat suprachiasmatic nuclei. *BioMed research international*, 2014:424982, January 2014.

[4] Henk Albus, Mariska J Vansteensel, Stephan Michel, Gene D Block, and Johanna H Meijer. A GABAergic mechanism is necessary for coupling dissociable ventral and dorsal regional oscillators within the circadian clock. *Current biology : CB*, 15(10):886–93, May 2005.

[5] Sungwon An, Robert P Irwin, Charles N Allen, Connie Tsai, and Erik D Herzog. Vasoactive intestinal polypeptide requires parallel changes in adenylate cyclase and phospholipase C to entrain circadian rhythms to a predictable phase. *Journal of neurophysiology*, 105(5):2289–96, May 2011.

[6] Sungwon An, Connie Tsai, Julie Ronecker, Alison Bayly, and Erik D Herzog. Spatiotemporal distribution of vasoactive intestinal polypeptide receptor 2 in mouse suprachiasmatic nucleus. *The Journal of comparative neurology*, 520(12):2730–41, August 2012.

[7] D G Aronson, G B Ermentrout, and N Kopell. Amplitude response of coupled oscillators. *Physica D: Nonlinear Phenomena*, 41:403–449, 1990.

[8] Sara J Aton and Erik D Herzog. Come together, right... now: synchronization of rhythms in a mammalian circadian clock. *Neuron*, 48(4):531–534, 2005.

[9] Sara J Aton, James E Huettner, Martin Straume, and Erik D Herzog. GABA and Gi/o differentially control circadian rhythms and synchrony in clock neurons. *Proceedings of the National Academy of Sciences of the United States of America*, 103(50):19188–93, December 2006.

[10] Julie E Baggs, Tom S Price, Luciano DiTacchio, Satchidananda Panda, Garret a Fitzgerald, and John B Hogenesch. Network features of the mammalian circadian clock. *PLoS biology*, 7(3):e52, March 2009.

[11] Neda Bagheri, Stephanie R Taylor, Kirsten Meeker, Linda R Petzold, and Francis J Doyle. Synchrony and entrainment properties of robust circadian oscillators. *Journal of the Royal Society, Interface / the Royal Society*, 5 Suppl 1:S17–28, August 2008.

[12] Sabine Becker-Weimann, Jana Wolf, Hanspeter Herzel, and Achim Kramer. Modeling feedback loops of the Mammalian circadian oscillator. *Biophysical journal*, 87(5):3023–34, November 2004.

[13] Michael A Belenky, P J Sollars, D B Mount, S L Alper, Y Yarom, and G E Pickard. Cell-type specific distribution of chloride transporters in the rat suprachiasmatic nucleus. *Neuroscience*, 165(4):1519–37, February 2010.

[14] Mino D C Belle, Casey O Diekman, Daniel B Forger, and Hugh D Piggins. Daily electrical silencing in the mammalian circadian clock. *Science (New York, N.Y.)*, 326(5950):281–4, October 2009.

[15] Samuel Bernard, Didier Gonze, Branka Cajavec, Hanspeter Herzel, and Achim Kramer. Synchronization-induced rhythmicity of circadian oscillators in the suprachiasmatic nucleus. *PLoS computational biology*, 3(4):e68, April 2007.

[16] Rachel C Besing, Jodi R Paul, Lauren M Hablitz, Courtney O Rogers, Russell L Johnson, Martin E Young, and Karen L Gamble. Circadian Rhythmicity of Active GSK3 Isoforms Modulates Molecular Clock Gene Rhythms in the Suprachiasmatic Nucleus. *Journal of biological rhythms*, 30(2):155–60, April 2015.

[17] Y Bouskila and F E Dudek. A rapidly activating type of outward rectifier K+ current and A-current in rat suprachiasmatic nucleus neurones. *The Journal of physiology*, 488 (Pt 2:339–50, October 1995.

[18] Marco Brancaccio, Elizabeth S Maywood, Johanna E Chesham, Andrew S I Loudon, and Michael H Hastings. A Gq-Ca2+ axis controls circuit-level encoding of circadian time in the suprachiasmatic nucleus. *Neuron*, 78(4):714–28, May 2013.

[19] T M Brown, Christopher S Colwell, J A Waschek, and Hugh D Piggins. Disrupted neuronal activity rhythms in the suprachiasmatic nuclei of vasoactive intestinal polypeptide-deficient mice. *Journal of neurophysiology*, 97(3):2553–8, March 2007.

[20] T M Brown and Hugh D Piggins. Spatiotemporal Heterogeneity in the Electrical Activity of Suprachiasmatic Nuclei Neurons and their Response to Photoperiod. *Journal of Biological Rhythms*, 24(1):44–54, February 2009.

[21] Ethan D Buhr, Seung-Hee Yoo, and Joseph S Takahashi. Temperature as a universal resetting cue for mammalian circadian oscillators. *Science (New York, N.Y.)*, 330(6002):379–85, October 2010.

[22] P W Burgoon, P T Lindberg, and M U Gillette. Different patterns of circadian oscillation in the suprachiasmatic nucleus of hamster, mouse, and rat. *Journal of comparative physiology. A, Neuroethology, sensory, neural, and behavioral physiology*, 190(2):167–71, February 2004.

[23] John H Caldwell, Greta Ann Herin, Georg Nagel, Ernst Bamberg, Astrid Scheschonka, and Heinrich Betz. Increases in intracellular calcium triggered by channelrhodopsin-2 potentiate the response of metabotropic glutamate receptor mGluR7. *The Journal of biological chemistry*, 283(36):24300–7, September 2008.

[24] Hee Joo Choi, C Justin Lee, Analyne Schroeder, Yoon Sik Kim, Seung Hoon Jung, Jeong Sook Kim, Do Young Kim, Eun Ju Son, Hee Chul Han, Seung Kil Hong, Christopher S Colwell, and Yang In Kim. Excitatory actions of GABA in the suprachiasmatic nucleus. *The Journal of neuroscience : the official journal of the Society for Neuroscience*, 28(21):5450–9, May 2008.

[25] Christopher S Colwell. Linking neural activity and molecular oscillations in the SCN. *Nature reviews. Neuroscience*, 12(10):553–69, October 2011.

[26] Christopher S Colwell, Stephan Michel, Jason Itri, Williams Rodriguez, J Tam, Vincent Lelievre, Zhou Hu, X Liu, and James a Waschek. Disrupted circadian rhythms in VIP- and PHI-deficient mice. *American journal of physiology. Regulatory, integrative and comparative physiology*, 285(5):R939–49, November 2003.

[27] Hugues Dardente, Jérôme S Menet, Etienne Challet, Benjamin B Tournier, Paul Pévet, and Mireille Masson-Pévet. Daily and circadian expression of neuropeptides in the suprachiasmatic nuclei of nocturnal and diurnal rodents. *Brain research. Molecular brain research*, 124(2):143–51, May 2004.

[28] Marcel De Jeu and Cyriel Pennartz. Circadian modulation of GABA function in the rat suprachiasmatic nucleus: excitatory effects during the night phase. *Journal of neurophysiology*, 87(2):834–44, February 2002.

[29] Daniel DeWoskin, Weihua Geng, Adam R Stinchcombe, and Daniel B Forger. It is not the parts, but how they interact that determines the behaviour of circadian rhythms across scales and organisms. *Interface focus*, 4(3):20130076, June 2014.

[30] Daniel DeWoskin, Jihwan Myung, Mino D C Belle, Hugh D Piggins, Toru Takumi, and Daniel B Forger. Distinct roles for GABA across multiple timescales in mammalian circadian timekeeping. *Proceedings of the National Academy of Sciences of the United States of America*, 2015.

[31] Casey O Diekman, Mino D C Belle, Robert P Irwin, Charles N Allen, Hugh D Piggins, and Daniel B Forger. Causes and consequences of hyperexcitation in central clock neurons. *PLoS computational biology*, 9(8):e1003196, August 2013.

[32] Casey O Diekman and Daniel B Forger. Clustering predicted by an electrophysiological model of the suprachiasmatic nucleus. *Journal of biological rhythms*, 24(4):322–33, August 2009.

[33] Jay C Dunlap. Molecular bases for circadian clocks. *Cell*, 96(2):271–90, January 1999.

[34] Ryosuke Enoki, Shigeru Kuroda, Daisuke Ono, Mazahir T Hasan, Tetsuo Ueda, Sato Honma, and Ken-Ichi Honma. Topological specificity and hierarchical network of the circadian calcium rhythm in the suprachiasmatic nucleus. *Proceedings of the National Academy of Sciences of the United States of America*, December 2012.

[35] Akifumi Enomoto, Juliette M Han, Chie-fang Hsiao, and Scott H Chandler. Sodium currents in mesencephalic trigeminal neurons from Nav1.6 null mice. *Journal of neurophysiology*, 98(2):710–9, August 2007.

[36] G. Bard Ermentrout and David H. Terman. *Mathematical Foundations of Neuroscience*, volume 35 of *Interdisciplinary Applied Mathematics*. Springer New York, New York, NY, 2010.

[37] Jennifer A Evans, Tanya L Leise, Oscar Castanon-Cervantes, and Alec J Davidson. Dynamic Interactions Mediated by Nonredundant Signaling Mechanisms Couple Circadian Clock Neurons. *Neuron*, 80(4):973–983, November 2013.

[38] Junmei Fan, Hongkui Zeng, David P Olson, Kimberly M Huber, Jay R Gibson, and Joseph S Takahashi. Vasoactive Intestinal Polypeptide (VIP)-Expressing Neurons in the Suprachiasmatic Nucleus Provide Sparse GABAergic Outputs to Local Neurons with Circadian Regulation Occurring Distal to the Opening of Postsynaptic GABAA Ionotropic Receptors. *The Journal of neuroscience : the official journal of the Society for Neuroscience*, 35(5):1905–20, February 2015.

[39] Sahar Farajnia, Tirsa L E van Westering, Johanna H Meijer, and Stephan Michel. Seasonal induction of GABAergic excitation in the central mammalian clock. *Proceedings of the National Academy of Sciences of the United States of America*, 111(26):9627–32, July 2014.

[40] Mark Farrant and Zoltan Nusser. Variations on an inhibitory theme: phasic and tonic activation of GABA(A) receptors. *Nature reviews. Neuroscience*, 6(3):215–29, March 2005.

[41] Nicholas C Foley, Tina Y Tong, Duncan K Foley, Joseph LeSauter, David K Welsh, and Rae Silver. Characterization of orderly spatiotemporal patterns of clock gene activation in mammalian suprachiasmatic nucleus. *European Journal of Neuroscience*, 33(10):1851–1865, May 2011.

[42] Daniel B Forger and Charles S Peskin. A detailed predictive model of the mammalian circadian clock. *Proceedings of the National Academy of Sciences of the United States of America*, 100(25):14806–11, December 2003.

[43] Daniel B Forger and Charles S Peskin. Stochastic simulation of the mammalian circadian clock. *Proceedings of the National Academy of Sciences of the United States of America*, 102(2):321–4, January 2005.

[44] G Mark Freeman, Rebecca M Krock, Sara J Aton, Paul Thaben, and Erik D Herzog. GABA networks destabilize genetic oscillations in the circadian pacemaker. *Neuron*, 78(5):799–806, June 2013.

[45] Albert Goldbeter, G Dupont, and M J Berridge. Minimal model for signal-induced Ca2+ oscillations and for their frequency encoding through protein phosphorylation. *Proceedings of the National Academy of Sciences of the United States of America*, 87(4):1461–5, February 1990.

[46] Didier Gonze, Samuel Bernard, Christian Waltermann, Achim Kramer, and Hanspeter Herzel. Spontaneous synchronization of coupled circadian oscillators. *Biophysical journal*, 89(1):120–9, July 2005.

[47] Fabienne Guillaumond, Hugues Dardente, Vincent Giguère, and Nicolas Cermakian. Differential control of Bmal1 circadian transcription by REV-ERB and ROR nuclear receptors. *Journal of biological rhythms*, 20(5):391–403, October 2005.

[48] A J Harmar. An essential role for peptidergic signalling in the control of circadian rhythms in the suprachiasmatic nuclei. *Journal of neuroendocrinology*, 15(4):335–8, April 2003.

[49] Anthony J Harmar, Hugh M Marston, Sanbing Shen, Christopher Spratt, Katrine M West, W John Sheward, Christine F Morrison, Julia R Dorin, Hugh D Piggins, Jean Claude Reubi, John S Kelly, Elizabeth S Maywood, and Michael H Hastings. The VPAC(2) receptor is essential for circadian function in the mouse suprachiasmatic nuclei. *Cell*, 109(4):497–508, May 2002.

[50] Erik D Herzog, Sara J Aton, Rika Numano, Yoshiyuki Sakaki, and Hajime Tei. Temporal precision in the mammalian circadian system: a reliable clock from less reliable neurons. *Journal of biological rhythms*, 19(1):35–46, February 2004.

[51] Alan L Hodgkin and Andrew F Huxley. A quantitative description of membrane current and its application to conduction and excitation in nerve. *The Journal of physiology*, 117(4):500–44, August 1952.

[52] John B Hogenesch, Y Z Gu, Sanjay Jain, and Christopher A Bradfield. The basic-helix-loop-helix-PAS orphan MOP3 forms transcriptionally active complexes with circadian and hypoxia factors. *Proceedings of the National Academy of Sciences of the United States of America*, 95(10):5474–9, May 1998.

[53] M Ikeda and M Nomura. cDNA cloning and tissue-specific expression of a novel basic helix-loop-helix/PAS protein (BMAL1) and identification of alternatively spliced variants with alternative translation initiation site usage. *Biochemical and biophysical research communications*, 233(1):258–64, April 1997.

[54] Natsuko Inagaki, Sato Honma, Daisuke Ono, Yusuke Tanahashi, and Ken-ichi Honma. Separate oscillating cell groups in mouse suprachiasmatic nucleus couple photoperiodically to the onset and end of daily activity. *Proceedings of the National Academy of Sciences of the United States of America*, 104(18):7664–9, May 2007.

[55] S T Inouye. Circadian rhythms of neuropeptides in the suprachiasmatic nucleus. *Progress in brain research*, 111:75–90, January 1996.

[56] Hideo Iwasaki and Takao Kondo. Circadian timing mechanism in the prokaryotic clock system of cyanobacteria. *Journal of biological rhythms*, 19(5):436–44, October 2004.

[57] Alexander C. Jackson, Gui Lan Yao, and Bruce P Bean. Mechanism of spontaneous firing in dorsomedial suprachiasmatic nucleus neurons. *The Journal of neuroscience : the official journal of the Society for Neuroscience*, 24(37):7985–98, September 2004.

[58] Anita Jagota, Horacio O de la Iglesia, and William J Schwartz. Morning and evening circadian oscillations in the suprachiasmatic nucleus in vitro. *Nature neuroscience*, 3(4):372–6, April 2000.

[59] Jeff R Jones, Michael C Tackenberg, and Douglas G McMahon. Manipulating circadian clock neuron firing rate resets molecular circadian rhythms and behavior. *Nature neuroscience*, pages 1–5, February 2015.

[60] Jae Kyoung Kim and Daniel B Forger. A mechanism for robust circadian timekeeping via stoichiometric balance. *Molecular systems biology*, 8(630):630, December 2012.

[61] Caroline H Ko and Joseph S Takahashi. Molecular components of the mammalian circadian clock. *Human molecular genetics*, 15 Spec No(2):R271–7, October 2006.

[62] Caroline H Ko, Yujiro R Yamada, David K Welsh, Ethan D Buhr, Andrew C Liu, Eric E Zhang, Martin R Ralph, Steve A Kay, Daniel B Forger, and Joseph S Takahashi. Emergence of noise-induced oscillations in the central circadian pacemaker. *PLoS biology*, 8(10):e1000513, January 2010.

[63] Satoshi Koinuma, Takeshi Asakawa, Mamoru Nagano, Keiichi Furukawa, Mitsugu Sujino, Koh-Hei Masumoto, Yoshihiro Nakajima, Seiichi Hashimoto, Kazuhiro Yagita, and Yasufumi Shigeyoshi. Regional circadian period difference in the suprachiasmatic nucleus of the mammalian circadian center. *The European journal of neuroscience*, 38(6):2832–41, September 2013.

[64] Nikolai I Kononenko and F Edward Dudek. Mechanism of irregular firing of suprachiasmatic nucleus neurons in rat hypothalamic slices. *Journal of neurophysiology*, 91(1):267–73, January 2004.

[65] Nikolai I Kononenko, Li-rong Shao, and F Edward Dudek. Riluzole-sensitive slowly inactivating sodium current in rat suprachiasmatic nucleus neurons. *Journal of neurophysiology*, 91(2):710–8, February 2004.

[66] Richard E Kronauer. Temporal subdivision of the circadian cycle. *Lectures on Mathematics in the Life Sciences*, 19:63–120, 1987.

[67] Sandra J Kuhlman and Douglas G McMahon. Rhythmic regulation of membrane potential and potassium current persists in SCN neurons in the absence of environmental input. *The European journal of neuroscience*, 20(4):1113–7, August 2004.

[68] Hanspeter Kunz and Peter Achermann. Simulation of circadian rhythm generation in the suprachiasmatic nucleus with locally coupled self-sustained oscillators. *Journal of Theoretical Biology*, 224(1):63–78, September 2003.

[69] Yoshiki Kuramoto. *Chemical oscillations, waves, and turbulence*. Courier Corporation, 2003.

[70] Boyoung Lee, Aiqing Li, Katelin F Hansen, Ruifeng Cao, Jae Hwa Yoon, and Karl Obrietan. CREB influences timing and entrainment of the SCN circadian clock. *Journal of biological rhythms*, 25(6):410–20, December 2010.

[71] Jean-Christophe Leloup and Albert Goldbeter. A molecular explanation for the long-term suppression of circadian rhythms by a single light pulse. *American journal of physiology. Regulatory, integrative and comparative physiology*, 280(4):R1206–12, April 2001.

[72] Jean-Christophe Leloup and Albert Goldbeter. Toward a detailed computational model for the mammalian circadian clock. *Proceedings of the National Academy of Sciences of the United States of America*, 100(12):7051–6, June 2003.

[73] Jean-Christophe Leloup and Albert Goldbeter. Modeling the mammalian circadian clock: sensitivity analysis and multiplicity of oscillatory mechanisms. *Journal of theoretical biology*, 230(4):541–62, October 2004.

[74] S Y Liou and H E Albers. Single unit response of neurons within the hamster suprachiasmatic nucleus to GABA and low chloride perfusate during the day and night. *Brain research bulletin*, 25(1):93–8, July 1990.

[75] Andrew C Liu, Hien G Tran, Eric E Zhang, Aaron a Priest, David K Welsh, and Steve A Kay. Redundant function of REV-ERBalpha and beta and non-essential role for Bmal1 cycling in transcriptional regulation of intracellular circadian rhythms. *PLoS genetics*, 4(2):e1000023, February 2008.

[76] Andrew C Liu, David K Welsh, Caroline H Ko, Hien G Tran, Eric E Zhang, Aaron a Priest, Ethan D Buhr, Oded Singer, Kirsten Meeker, Inder M Verma, Francis J Doyle, Joseph S Takahashi, and Steve A Kay. Intercellular coupling confers robustness against mutations in the SCN circadian clock network. *Cell*, 129(3):605–16, May 2007.

[77] Chen Liu and Steven M Reppert. GABA synchronizes clock cells within the suprachiasmatic circadian clock. *Neuron*, 25(1):123–8, January 2000.

[78] Chen Liu, David R Weaver, Steven H Strogatz, and Steven M Reppert. Cellular construction of a circadian clock: period determination in the suprachiasmatic nuclei. *Cell*, 91(6):855–60, December 1997.

[79] Elizabeth S Maywood, Johanna E Chesham, John a O'Brien, and Michael H Hastings. A diversity of paracrine signals sustains molecular circadian cycling in suprachiasmatic nucleus circuits. *Proceedings of the National Academy of Sciences of the United States of America*, 108(34):14306–11, August 2011.

[80] Erin L McDearmon, Kush N Patel, Caroline H Ko, Jacqueline a Walisser, Andrew C Schook, Jason L Chong, Lisa D Wilsbacher, Eun J Song, Hee-Kyung Hong, Christopher a Bradfield, and Joseph S Takahashi. Dissecting the functions of the mammalian clock protein BMAL1 by tissue-specific rescue in mice. *Science (New York, N.Y.)*, 314(5803):1304–8, November 2006.

[81] Edward J McManus, Kei Sakamoto, Laura J Armit, Leah Ronaldson, Natalia Shpiro, Rodolfo Marquez, and Dario R Alessi. Role that phosphorylation of GSK3 plays in insulin and Wnt signalling defined by knockin analysis. *The EMBO journal*, 24(8):1571–83, April 2005.

[82] Kirsten Meeker, Richard Harang, Alexis B Webb, David K Welsh, Francis J Doyle, Guillaume Bonnet, Erik D Herzog, and Linda R Petzold. Wavelet measurement suggests cause of period instability in mammalian circadian neurons. *Journal of biological rhythms*, 26(4):353–62, August 2011.

[83] Johanna H Meijer, Stephan Michel, Henk T Vanderleest, and Jos H T Rohling. Daily and seasonal adaptation of the circadian clock requires plasticity of the SCN neuronal network. *The European journal of neuroscience*, 32(12):2143–51, December 2010.

[84] Andrea L Meredith, Steven W Wiler, Brooke H Miller, Joseph S Takahashi, Anthony a Fodor, Norman F Ruby, and Richard W Aldrich. BK calcium-activated potassium channels regulate circadian behavioral rhythms and pacemaker output. *Nature neuroscience*, 9(8):1041–9, August 2006.

[85] Henry P Mirsky, Andrew C Liu, David K Welsh, Steve A Kay, and Francis J Doyle. A model of the cell-autonomous mammalian circadian clock. *Proceedings of the National Academy of Sciences of the United States of America*, 106(27):11107–12, July 2009.

[86] R Y Moore and J C Speh. GABA is the principal neurotransmitter of the circadian system. *Neuroscience letters*, 150(1):112–6, February 1993.

[87] Andre J Morin, Luc Denoroy, and Michel Jouvet. Daily variations in concentration of vasoactive intestinal polypeptide immunoreactivity in discrete brain areas of the rat. *Brain research*, 538(1):136–40, January 1991.

[88] L P Morin and C N Allen. The circadian visual system, 2005. *Brain research reviews*, 51(1):1–60, June 2006.

[89] Maciej Mrugala, Piotr Zlomanczuk, Anita Jagota, and William J Schwartz. Rhythmic multiunit neural activity in slices of hamster suprachiasmatic nucleus reflect prior photoperiod. *American journal of physiology. Regulatory, integrative and comparative physiology*, 278(4):R987–94, April 2000.

[90] Jihwan Myung, Sungho Hong, Daniel DeWoskin, Erik De Schutter, Daniel B Forger, and Toru Takumi. GABA-mediated repulsive coupling between circadian clock neurons encodes seasonal time. *Under review*, 2015.

[91] Jihwan Myung, Sungho Hong, Fumiyuki Hatanaka, Yoshihiro Nakajima, Erik De Schutter, and Toru Takumi. Period Coding of Bmal1 Oscillators in the Suprachiasmatic Nucleus. *The Journal of neuroscience : the official journal of the Society for Neuroscience*, 32(26):8900–8918, June 2012.

[92] Georg Nagel, Tanjef Szellas, Wolfram Huhn, Suneel Kateriya, Nona Adeishvili, Peter Berthold, Doris Ollig, Peter Hegemann, and Ernst Bamberg. Channelrhodopsin-2, a directly light-gated cation-selective membrane channel. *Proceedings of the National Academy of Sciences of the United States of America*, 100(24):13940–5, November 2003.

[93] Emiko Naito, Tsuyoshi Watanabe, Hajime Tei, Takashi Yoshimura, and Shizufumi Ebihara. Reorganization of the suprachiasmatic nucleus coding for day length. *Journal of biological rhythms*, 23(2):140–9, April 2008.

[94] Yoshihiro Nakajima, Tomomi Yamazaki, Shigeaki Nishii, Takako Noguchi, Hideto Hoshino, Kazuki Niwa, Vadim R Viviani, and Yoshihiro Ohmiya. Enhanced beetle luciferase for high-resolution bioluminescence imaging. *PloS one*, 5(4):e10011, January 2010.

[95] Takako Noguchi and Kazuto Watanabe. Regional differences in circadian period within the suprachiasmatic nucleus. *Brain research*, 1239:119–26, November 2008.

[96] Takako Noguchi, Kazuto Watanabe, Akihiko Ogura, and Sadao Yamaoka. The clock in the dorsal suprachiasmatic nucleus runs faster than that in the ventral. *The European journal of neuroscience*, 20(11):3199–202, December 2004.

[97] K Obrietan, S Impey, D Smith, J Athos, and D R Storm. Circadian regulation of cAMP response element-mediated gene expression in the suprachiasmatic nuclei. *The Journal of biological chemistry*, 274(25):17748–56, June 1999.

[98] Gisele A Oda and W Otto Friesen. A model for "splitting" of running-wheel activity in hamsters. *Journal of biological rhythms*, 17(1):76–88, February 2002.

[99] Satchidananda Panda, Marina P Antoch, Brooke H Miller, Andrew I Su, Andrew B Schook, Marty Straume, Peter G Schultz, Steve A Kay, Joseph S Takahashi, and John B Hogenesch. Coordinated transcription of key pathways in the mouse by the circadian clock. *Cell*, 109(3):307–20, May 2002.

[100] J R Paul, R L Johnson, R S Jope, and K L Gamble. Disruption of circadian rhythmicity and suprachiasmatic action potential frequency in a mouse model with constitutive activation of glycogen synthase kinase 3. *Neuroscience*, 226:1–9, December 2012.

[101] C M Pennartz, M A Bierlaagh, and A M Geurtsen. Cellular mechanisms underlying spontaneous firing in rat suprachiasmatic nucleus: involvement of a slowly inactivating component of sodium current. *Journal of neurophysiology*, 78(4):1811–25, October 1997.

[102] Cyriel M A Pennartz, Marcel T G de Jeu, Nico P A Bos, Jeroen Schaap, and Alwin M S Geurtsen. Diurnal modulation of pacemaker potentials and calcium current in the mammalian circadian clock. *Nature*, 416(6878):286–90, March 2002.

[103] Hugh D Piggins and David J Cutler. The roles of vasoactive intestinal polypeptide in the mammalian circadian clock. *The Journal of endocrinology*, 177(1):7–15, April 2003.

[104] C S Pittendrigh and Serge Daan. A functional analysis of circadian pacemakers in nocturnal rodents. V. Pacemaker Structure: A clock for all seasons. *Journal of comparative physiology*, 106:333–355, 1976.

[105] Gilbert R Pitts, Hidenobu Ohta, and Douglas G McMahon. Daily rhythmicity of large-conductance Ca2+ -activated K+ currents in suprachiasmatic nucleus neurons. *Brain research*, 1071(1):54–62, February 2006.

[106] Martin R Ralph and Michael Menaker. Bicuculline blocks circadian phase delays but not advances. *Brain research*, 325(1-2):362–5, January 1985.

[107] Angela Relógio, Pål O Westermark, Thomas Wallach, Katja Schellenberg, Achim Kramer, and Hanspeter Herzel. Tuning the mammalian circadian clock: robust synergy of two loops. *PLoS computational biology*, 7(12):e1002309, December 2011.

[108] Steven M Reppert and David R Weaver. Molecular analysis of mammalian circadian rhythms. *Annual review of physiology*, 63:647–76, January 2001.

[109] L C Roden and I a Carré. The molecular genetics of circadian rhythms in Arabidopsis. *Seminars in cell & developmental biology*, 12(4):305–15, August 2001.

[110] J Rohling, J H Meijer, Henk Tjebbe VanderLeest, and J Admiraal. Phase differences between SCN neurons and their role in photoperiodic encoding; a simulation of ensemble patterns using recorded single unit electrical activity patterns. *Journal of physiology, Paris*, 100(5-6):261–70, 2006.

[111] Jeroen Schaap, Henk Albus, Henk Tjebbe VanderLeest, Paul H C Eilers, László Détári, and Johanna H Meijer. Heterogeneity of rhythmic suprachiasmatic nucleus neurons: Implications for circadian waveform and photoperiodic encoding. *Proceedings of the National Academy of Sciences of the United States of America*, 100(26):15994–9, December 2003.

[112] Analyne Schroeder, Dawn H Loh, Maria C Jordan, Kenneth P Roos, and Christopher S Colwell. Circadian regulation of cardiovascular function: a role for vasoactive intestinal peptide. *American journal of physiology. Heart and circulatory physiology*, 300(1):H241–50, January 2011.

[113] Alexander S Shavkunov, Norelle C Wildburger, Miroslav N Nenov, Thomas F James, Tetyana P Buzhdygan, Neli I Panova-Elektronova, Thomas a Green, Ronald L Veselenak, Nigel Bourne, and Fernanda Laezza. The fibroblast growth factor 14voltage-gated sodium channel complex is a new target of glycogen synthase kinase 3 (GSK3). *The Journal of biological chemistry*, 288(27):19370–85, July 2013.

[114] Kazuyuki Shinohara, Sato Honma, Yumiko Katsuno, Hiroshi Abe, and Ken-ichi Honma. Circadian rhythms in the release of vasoactive intestinal polypeptide and arginine-vasopressin in organotypic slice culture of rat suprachiasmatic nucleus. *Neuroscience letters*, 170(1):183–6, March 1994.

[115] Sandra M Siepka, Seung-Hee Yoo, Junghea Park, Weimin Song, Vivek Kumar, Yinin Hu, Choogon Lee, and Joseph S Takahashi. Circadian mutant Overtime reveals F-box protein FBXL3 regulation of cryptochrome and period gene expression. *Cell*, 129(5):1011–23, June 2007.

[116] Rae Silver, Joseph LeSauter, Patrick A Tresco, and Michael N Lehman. A diffusible coupling signal from the transplanted suprachiasmatic nucleus controlling circadian locomotor rhythms. *Nature*, 382(6594):810–3, August 1996.

[117] Rae Silver, Alicia I Sookhoo, Joseph LeSauter, Paula Stevens, Heiko T Jansen, and Michael N Lehman. Multiple regulatory elements result in regional specificity in circadian rhythms of neuropeptide expression in mouse SCN. *Neuroreport*, 10(15):3165–74, October 1999.

[118] Choon Kiat Sim and Daniel B Forger. Modeling the electrophysiology of suprachiasmatic nucleus neurons. *Journal of biological rhythms*, 22(5):445–53, October 2007.

[119] R D Smith, S Inouye, and F W Turek. Central administration of muscimol phase-shifts the mammalian circadian clock. *Journal of comparative physiology A, Sensory, neural, and behavioral physiology*, 164(6):805–14, February 1989.

[120] A Sumová, Z Trávnícková, R Peters, W J Schwartz, and H Illnerová. The rat suprachiasmatic nucleus is a clock for all seasons. *Proceedings of the National Academy of Sciences of the United States of America*, 92(17):7754–8, August 1995.

[121] Alena Sumová, Martin Já, Martin Sládek, Ivo Šauman, and Helena Illnerová. Clock Gene Daily Profiles and Their Phase Relationship in the Rat Suprachiasmatic Nucleus Are Affected by Photoperiod. *Journal of Biological Rhythms*, 18(2):134–144, April 2003.

[122] Joseph S Takahashi, Hee-Kyung Hong, Caroline H Ko, and Erin L McDearmon. The genetics of mammalian circadian order and disorder: implications for physiology and disease. *Nature reviews. Genetics*, 9(10):764–75, October 2008.

[123] Mónica Tapia, Ana Del Puerto, Alberto Puime, Diana Sánchez-Ponce, Laure Fronzaroli-Molinieres, Noemí Pallas-Bazarra, Edmond Carlier, Pierre Giraud, Dominique Debanne, Francisco Wandosell, and Juan José Garrido. GSK3 and β-catenin determines functional expression of sodium channels at the axon initial segment. *Cellular and molecular life sciences : CMLS*, 70(1):105–20, January 2013.

[124] Tsz-Leung To, Michael A Henson, Erik D Herzog, and Francis J Doyle. A molecular model for intercellular synchronization in the mammalian circadian clock. *Biophysical journal*, 92(11):3792–803, June 2007.

[125] Zdenka Travnickova-Bendova, Nicolas Cermakian, Steven M Reppert, and Paolo Sassone-Corsi. Bimodal regulation of mPeriod promoters by CREB-dependent signaling and CLOCK/BMAL1 activity. *Proceedings of the National Academy of Sciences of the United States of America*, 99(11):7728–33, May 2002.

[126] Gérard Triqueneaux, Sandrine Thenot, Tomoko Kakizawa, Marina P Antoch, Rachid Safi, Joseph S Takahashi, Franck Delaunay, and Vincent Laudet. The orphan receptor Rev-erbalpha gene is a target of the circadian clock pacemaker. *Journal of molecular endocrinology*, 33(3):585–608, December 2004.

[127] Hiroki R Ueda, Kenzo Hirose, and Masamitsu Iino. Intercellular coupling mechanism for synchronized and noise-resistant circadian oscillators. *Journal of theoretical biology*, 216(4):501–12, June 2002.

[128] Henk Tjebbe VanderLeest, Thijs Houben, Stephan Michel, Tom Deboer, Henk Albus, Mariska J Vansteensel, Gene D Block, and Johanna H Meijer. Seasonal encoding by the circadian pacemaker of the SCN. *Current biology : CB*, 17(5):468–73, March 2007.

[129] Christina Vasalou and Michael A Henson. A multiscale model to investigate circadian rhythmicity of pacemaker neurons in the suprachiasmatic nucleus. *PLoS computational biology*, 6(3):e1000706, March 2010.

[130] Christina Vasalou and Michael A Henson. A multicellular model for differential regulation of circadian signals in the core and shell regions of the suprachiasmatic nucleus. *Journal of theoretical biology*, 288:44–56, November 2011.

[131] Christina Vasalou, Erik D Herzog, and Michael A Henson. Multicellular model for intercellular synchronization in circadian neural networks. *Biophysical journal*, 101(1):12–20, July 2011.

[132] Shlomo Wagner, Mona Castel, Harold Gainer, and Y Yarom. GABA in the mammalian suprachiasmatic nucleus and its role in diurnal rhythmicity. *Nature*, 387(6633):598–603, June 1997.

[133] Tongfei A Wang, Yanxun V Yu, Gubbi Govindaiah, Xiaoying Ye, Liana Artinian, Todd P Coleman, Jonathan V Sweedler, Charles L Cox, and Martha U Gillette. Circadian rhythm of redox state regulates excitability in suprachiasmatic nucleus neurons. *Science (New York, N.Y.)*, 337(6096):839–42, August 2012.

[134] David R Weaver. The Suprachiasmatic Nucleus: A 25-Year Retrospective. *Journal of Biological Rhythms*, 13(2):100–112, April 1998.

[135] Alexis B Webb, Nikhil Angelo, James E Huettner, and Erik D Herzog. Intrinsic, nondeterministic circadian rhythm generation in identified mammalian neurons. *Proceedings of the National Academy of Sciences of the United States of America*, 106(38):16493–8, September 2009.

[136] David K Welsh, D E Logothetis, M Meister, and Steven M Reppert. Individual neurons dissociated from rat suprachiasmatic nucleus express independently phased circadian firing rhythms. *Neuron*, 14(4):697–706, April 1995.

[137] David K Welsh, Joseph S Takahashi, and Steve A Kay. Suprachiasmatic nucleus: cell autonomy and network properties. *Annual review of physiology*, 72:551–77, March 2010.

[138] John C Williams, Jianjin Xu, Zhongju Lu, Aleksandra Klimas, Xuxin Chen, Christina M Ambrosi, Ira S Cohen, and Emilia Entcheva. Computational optogenetics: empirically-derived voltage- and light-sensitive channelrhodopsin-2 model. *PLoS computational biology*, 9(9):e1003220, January 2013.

[139] A T Winfree. *The Geometry of Biological Time*. Springer, New York, 2001.

[140] Yujiro R Yamada, Caroline H Ko, Joseph S Takahashi, and Daniel B Forger. Exploring Network Properties of a Detailed Mathematical Model of the Supra-Chiasmatic Nuclei.

[141] Shun Yamaguchi, Hiromi Isejima, Takuya Matsuo, Ryusuke Okura, Kazuhiro Yagita, Masaki Kobayashi, and Hitoshi Okamura. Synchronization of cellular clocks in the suprachiasmatic nucleus. *Science (New York, N.Y.)*, 302(5649):1408–12, November 2003.

[142] Yoshiaki Yamaguchi, Toru Suzuki, Yasutaka Mizoro, Hiroshi Kori, Kazuki Okada, Yulin Chen, Jean-Michel Fustin, Fumiyoshi Yamazaki, Naoki Mizuguchi, Jing Zhang, Xin Dong, Gozoh Tsujimoto, Yasushi Okuno, Masao Doi, and Hitoshi Okamura. Mice genetically deficient in vasopressin V1a and V1b receptors are resistant to jet lag. *Science (New York, N.Y.)*, 342(6154):85–90, October 2013.

[143] Jing Yang, Felino R A Cagampang, Yasuhisa Nakayama, and Shin-Ichi T Inouye. Vasoactive intestinal polypeptide precursor mRNA exhibits diurnal variation in the rat suprachiasmatic nuclei. *Brain research. Molecular brain research*, 20(3):259–62, November 1993.

[144] Eric E Zhang, Yi Liu, Renaud Dentin, Pagkapol Y Pongsawakul, Andrew C Liu, Tsuyoshi Hirota, Dmitri a Nusinow, Xiujie Sun, Severine Landais, Yuzo Kodama, David a Brenner, Marc Montminy, and Steve a Kay. Cryptochrome mediates circadian regulation of cAMP signaling and hepatic gluconeogenesis. *Nature medicine*, 16(10):1152–6, October 2010.